THE LARGE SCALE MOTIONS OF GALAXIES

Han Ying Loke

Presented for the degree of Doctor of Philosophy

University of Edinburgh

1997

Declaration

The contents of this thesis are all of my own work except where references are cited.

Han Ying Loke

September 1997

Publication

The paper "The correlation between bulk and shell velocities in cosmology", which forms the content of chapter 2, was published in Loke & Heavens, 1996, MNRAS, 279, 1303.

Acknowledgements

First and foremost as far as academic and technical assistance are concerned, I wish to thank my supervisors Dr. Alan Heavens, Prof. John Peacock and assistant supervisor Dr. Andy Taylor. Alan Heavens has been my principal supervisor throughout my entire PhD course and he has been tremendously helpful in numerous occasion to say the least. Without his guidance, advice, and the effort of reading through the whole contents of this work, my thesis would probably never exist. And when additional help was needed, John Peacock and Andy Taylor have proved to be more than just another two useful supervisors that I had. The input from other academic staff like Prof. Andy Lawrence and Prof. Peter Brand on subjects that are not necessarily related to the thesis was also an inspiration for me and they will always be remembered.

It was my good fortune to have worked in an environment like the Royal Observatory. Apart from the excellent facilities provided by the STARLINK, I was constantly surrounded by experts in various fields of astronomy from whom I could always seek technical assistance. It was also a pleasure to have worked along with other PhD students some of whom like Stephen Dodds, Steve McNally, Andrew Thackrach, Andrew Harrison and Jonathan Tedds who have all left; and others like William Ballinger (thanks for reading part of this thesis), Alison Stirling, Michael McCartney, Henry Buckley, Simon Dye, Paulina Lira, Ian Waddington, Richard Knox, Richard Brookie, Elese Archibald, Mathew Horrobin, and many other relatively new students who I am sure I will also enjoy their company if I was given enough time to know them better. On the financial side, I wish to thank the Lee's Foundation in Malaysia for the funding of the university fees during the second and third year of my PhD course.

Last and certainly not least, I wish to express my gratitude to all my family members, particularly my parents. Throughout my academic study, they have provided not just the financial support that I needed, but also the mental encouragement that I cherished. However such gratitude extends way beyond my PhD study; It goes all the way back to the first day I was born. While in our hearts we appreciate the love and care of each other in the family, we often do so without telling each other. Perhaps sometime it is hard to express one's feeling verbally, or may be such gratitude just cannot be expressed in words, certainly not in one short paragraph that one customary adheres to in the acknowledgements. With the completion of this thesis, this is perhaps the best chance yet for me to express my gratitude to my parents for bringing me up and looking after me for twenty odd years. I will always be in debt to you all.

Abstract

This thesis concerns with the study of the large scale motions of the universe. In particular the peculiar velocities of galaxies are used in a variety of ways to estimate some of the most important cosmological parameters.

Many galaxies are observed to be moving with a velocity that is not quite consistent with the picture of a homogeneous and isotropic universe. Such peculiar velocity must thus be caused by the small inhomogeneities that are still present today. By studying this velocity distortion, one should in principle be able to probe the underlying mass which light alone does not reveal.

In chapter 1, a brief introduction of cosmology is presented. Here I outline some of the most fundamental principles of cosmology and their evidence, namely the expansion of the universe and its homogeneity and isotropy. Using the theory of general relativity, these features lead us to the invention of the Robertson-Walker metric. I then show how the dynamics of the universe depend on its dominant constituents and density. The different morphology of galaxies is also presented where the general features of spirals and ellipticals are outlined. On the section of structure formation, the standard Newtonian treatment to the density perturbations is discussed in the linear regime. Here we see how structures such as galaxies can be formed from the growth of some initial density fluctuations. At the end of the chapter, the importance of the peculiar velocity to the work of this thesis is discussed.

Chapter 2 gives an account of how the correlation of bulk and shell velocities can be used together with their measurements to constrain $\beta \equiv \Omega^{0.6}/b$. The observational evidence of a relatively stationary shell in a large bulk flow environment prompted us

to investigate the likelihood of such an unlikely occurrence. Our analysis shows that the shell velocity measurements can be heavily contaminated with noise. In the absence of noise, the correlation between these two velocities depends only on the parameter β and the power spectrum used. We carried out the analysis with different models of power spectrum and for the theoretical predictions from these models to match up with observations, we conclude that the value of β should be in the order of unity. The two principal models of power spectrum that we tested are that of Peacock & Dodds (1994) and the CDM-like model. The content of this chapter is identical to the paper published by Loke & Heavens (1996).

In chapter 3, we applied a statistical likelihood method on the redshift distortion to give a joint probabilistic value of β and σ_8. The existence of peculiar velocity distorts the true spatial galaxy distribution and this hinders us from obtaining the real-space power spectrum. However, if we resolve the density perturbations in the formalism of a continuous spherical transform, it is possible to formulate statistically the likelihood distribution of the density perturbations under the redshift distortion, given a value of β and an appropriate model of the power spectrum. By matching up the likelihood predictions of the density perturbations in redshift space to that of a real galaxy catalogue, it is then possible to constrain the value of β and the power spectrum, which in this case is assumed to depend on σ_8 only. The analysis in this chapter is based on the work of Heavens & Taylor (1995) with the crucial difference that the analysis was carried out by setting the boundary at infinity and as such we do not have to worry about the boundary conditions.

In chapters 4 and 5, a theoretical model of the velocity field is developed under the linear regime and the assumption of a irrotational flow ($\nabla \times \mathbf{v} = 0$). The analysis predicts that the density potential derived from a galaxy catalogue is linearly related to the velocity potential via the parameter β, if galaxies are linear tracers of mass. In chapter 4, I compare the predicted velocity potential derived from the IRAS galaxy catalogue with that of POTENT (where potential was constructed from the actual measurement of velocity). In theory the comparison of these two potentials should yield a value of β. However, the analysis in chapter 4 is flawed by the fact that the redshift distortion was not properly taken into account. Nevertheless, the results do suggest that there

might be a correlation between these two potentials. In chapter 5 the redshift distortion was properly treated by expanding the potential into its spherical harmonic components. Much of the analysis in this chapter is based on the previous work of Nusser & Davis (1994). Here I attempted constructing the dipole ($l \leq 1$) velocity potential from the IRAS galaxy catalogue using different values of β. This is then compared to the same dipole component of POTENT. My results suggest that the predicted dipole potential does not match that of POTENT for a reasonable value of β. This contradicts with the results of $\beta \simeq 0.6$ found by Nusser & Davis (1994) where the dipole velocity was analysed. For $l > 1$ multipoles, the construction depends on the boundary conditions at infinity, which the current survey does not probe. Therefore comparison of the two potentials here does not yield any useful result.

Finally in chapter 6, I give a short conclusion of my work and an overview of the current state of cosmology, in particular the measurements that will be of immense importance to my work in future. Some of the most important unresolved issues (such as the values of Hubble constant, density of the universe, mass/light bias, etc) in cosmology are also discussed.

Contents

Chapter 1

Introduction to Cosmology

1.1 Outline of the Thesis

In the first chapter, the basic features and principles of cosmology are presented. Here I outline how the observational evidences of the universe have propelled us into developing the standard model in cosmology. With the notion of a homogeneous, isotropic and expanding universe, the Robertson-Walker Metric can be derived from the theory of general relativity. I also show how different constituents (e.g. matter, radiation) and their density can affect the expansion and ultimately the fate of the universe. In the latter part of this chapter, the standard theories of structure formation using the Newtonian analysis are presented. We see how structures such as galaxies can be formed from the linear growth of density perturbations. Finally I outline how the expansion of the universe produces a velocity potential that is curl-free, which is of great importance to the whole of this thesis as all the subsequent chapters utilise this curl-free potential assumption to carry out their analysis.

This thesis deals mainly with the study of peculiar velocity. The aim here is to extract some of the cosmological parameters, in particular β by various direct and indirect methods. Chapter 2 shows how measurements of the bulk streaming and shell streaming can be combined, taking proper account of shot noise and correlation between these two measurements, to put constraints on β. Our analysis suggests that in order to have a

stationary shell in a huge bulk flow environment, β should be in the order of unity for a reasonable power spectrum. The work of this chapter is also published in Loke & Heavens (1996).

In chapter 3 we investigate how the indirect effects of peculiar velocities can be used to constrain β. This chapter develops the theory for a continuous spherical transform of redshift surveys. In common with the discrete transform (Heavens & Taylor 1995) upon which it is based, the spherical nature of the redshift distortion and specification of a typical redshift survey (radial selection function, angular masking near galactic plane etc) can be incorporated naturally into this spherical coordinate system. The continuous transform has the theoretical advantage that no finite outer boundary is needed for specification. We apply the method to the IRAS 1.2 Jy survey (Fisher et al. 1995a) and found that small-scale velocity dispersion does affect the value of β deduced. Although its value varies according to the modes analysed, it is still consistent with the results of e.g. Heavens & Taylor (1995), Hamilton (1993a).

Chapter 4 shows how the peculiar velocity potential derived by POTENT can be used directly to estimate β, by comparison with a potential constructed from a 3D redshift galaxy survey. Under the simple mass/light bias hypothesis made by equation (1.85) and the assumption of a linear growth of density perturbations, the potential constructed from the galaxy survey is simply related to the velocity potential via the parameter β. Thus comparing these two potentials should yield the value of β. This has similarities with comparison of the predicted and observed peculiar velocities, but with two potential advantages. Firstly, there is the practical advantage that the potential is a scalar quantity, whereas the peculiar velocity in its entirety is a vector, and secondly, the potential is influenced more by long-wavelength perturbations than the velocity field, so a linear analysis of the potential should be more accurate.

In chapter 5, we take into account of the fact that the predicted velocity potential is calculated from a redshift survey, not a real-space survey, and carry out a multipole expansion of the velocity potential in redshift space. This method was originally used by Nusser & Davis (1994) to estimate β by matching the dipole velocity derived from POTENT. We extend the analysis to higher velocity multipoles to estimate β. This

exercise was only partially successful as technical problems prevented multipoles beyond dipole being effectively used. This may be a profitable future area of study.

Finally, some brief conclusions and final remarks are presented in chapter 6.

1.2 Our Universe

There are countless heavenly objects in our universe. On the small scale we have dust and particles; further up the scale there are meteors and comets; then there are planets, moons and stars like our Sun. On an even bigger scale, we have millions of galaxies and clusters of galaxies. Beside all these, there are also many exotic objects such as quasars, black holes, pulsars, etc which were discovered only within the last few decades. The universe is truly amazing and varied in its contents and to study them all would be a near impossible task. What cosmology concerns is the study of the large-scale structure and behaviour of the universe. It does not attempt to yield information and make predictions on scales that are smaller than the extragalactic one. At first the purpose of cosmology may appear to be over ambitious given that our tools for observation and our knowledge of the laws of nature still leave considerable room for improvement. However the advancement in the understanding of the physical laws and the rapid improvements in our observational technique in the last few decades have put us in a position to make some sense out of what we observe about the universe. We are still a long way from understanding fully our universe but perhaps one day we may answer the ultimate questions posed by cosmology: How did the universe come about? What are the contents of the universe? And what is the fate of our universe?

The purpose of this chapter is to give a brief background knowledge and the current state of cosmology. It shows how observations made on galaxies, nucleosysthesis, and microwave background radiation (sections 1.3, 1.4, and 1.5) in recent decades have led to the idea of the big bang cosmology; and how in sections 1.6 and 1.7 the notion of homogeneity and isotropy allows us to construct the Robertson-Walker space-time metric. The dynamics of the universe are then described in section 1.8 where the consequences of the Friedmann equations are also discussed. In section 1.9 the different morphology

and surface brightness profile of galaxies are outlined. In sections 1.10 and 1.11 the theory of structure formation from the Newtonian treatment of perturbations is presented. The problems of using galaxies as the tracer of mass are discussed in section 1.12. The material discussed in section 1.13 about the peculiar velocity of galaxies lays the basic theoretical foundations which will be useful in all later chapters. A brief description of the data extracted from the galaxy survey is presented in section 1.14. Finally the outline of the whole thesis is given in section 1.1.

1.3 Expanding Universe

To begin the study of cosmology, there must be a common starting point. The most fundamental feature of the so-called standard cosmology is the expansion of the universe. The expansion was discovered by Hubble in the 1920s when galaxies were observed to be moving away from us by virtue of the fact that the spectral lines are redshifted (apart from some nearby galaxies such as Andromeda which is moving towards us). Not only are galaxies moving away from us, their recession velocity u is directly proportional to the distance l from us:

$$u = H_0 l. \tag{1.1}$$

This is called the Hubble's law and H_0 is the Hubble constant. Since nothing dictates that H_0 has been a constant during all time rather than a function of time $H(t)$, the subscript 0 denotes the value at present time. The value initially found by Hubble was H_0=550 km s^{-1} Mpc^{-1}. This value was too high because it was not known at the time that there are two types of Cepheid variable stars (used as calibrators). Observations in recent decades have put the value ranging from 50 to 85 in the same units. It is now customary to put the uncertainty in H_0 via the parameter h:

$$H_0 = 100\,h \text{ km s}^{-1}\text{Mpc}^{-1}. \tag{1.2}$$

If one projects the expansion of the universe backward in time, it is then clear that at some earlier epoch our universe began with the so-called "Big Bang", where everything

started off with a gigantic explosion at $t = 0$ and expanded and evolved into the universe that we observe today.

The Hubble constant is one of the most important parameters in cosmology, its value determining the size and age of our universe. If H_0 is large, the universe was expanding rapidly and therefore took less time to reach the present size. So a high value of H_0 means a young universe while a low value of H_0 would imply that the universe is older. In fact the age of the universe is inversely proportional to the Hubble constant. Current measurements of H_0 give an age of 15-20 billion years for the universe.

1.4 Nucleosynthesis in the Early Universe

From the moment of explosion up to the Planck time of 10^{-43}s, the physical conditions (e.g. temperature, density) of the universe were so extreme that we do not know the physical processes that were going on with our present understanding of physics. From the Planck time onwards, fundamental particles like quarks, antiquarks, leptons, antileptons, and some vector bosons (e.g. photon, $W^{\pm}$, Z) emerged until about 10^{-10}s when the temperature became too low for the quarks to exist as a single particle. Instead confinement of three quarks produced baryons such as protons and neutrons, and the quark-antiquark pairs became mesons. About a few seconds after the big bang, nucleosynthesis started to occur between proton (p) and neutron (n) to produce deuteron $^2H^+$ (d) with the release of radiation:

$$n + p \rightarrow d + \gamma. \tag{1.3}$$

A small amount of neutral deuterium atoms ^2H was then formed when a deuteron bound with an electron. The remaining deuterons then took part in the fusion reactions to form $^3He^{++}$ and triton $^3H^+$:

$$\begin{aligned} d + d &\rightarrow {}^3He^{++} + n \\ p + d &\rightarrow {}^3He^{++} + \gamma \\ n + d &\rightarrow {}^3H^{+} + \gamma \end{aligned}$$

$$\begin{aligned} d + d &\rightarrow {}^3\mathrm{H}^+ + p \\ n + {}^3\mathrm{He}^{++} &\rightarrow {}^3\mathrm{H}^+ + p \end{aligned} \tag{1.4}$$

The ${}^3\mathrm{He}^{++}$ and ${}^3\mathrm{H}^+$ formed then took part in further fusion reactions to produce helium nuclei ${}^4\mathrm{He}^{++}$ which is very stable:

$$\begin{aligned} n + {}^3\mathrm{He}^{++} &\rightarrow {}^4\mathrm{He}^{++} + \gamma \\ d + {}^3\mathrm{He}^{++} &\rightarrow {}^4\mathrm{He}^{++} + p \\ p + {}^3\mathrm{H}^+ &\rightarrow {}^4\mathrm{He}^{++} + \gamma \\ d + {}^3\mathrm{H}^+ &\rightarrow {}^4\mathrm{He}^{++} + n. \end{aligned} \tag{1.5}$$

Detailed calculation of the beta decays of neutron to proton shows that at the point of nucleosynthesis the ratio of neutron to proton number is

$$\frac{N_n}{N_p} \simeq \frac{1}{7}. \tag{1.6}$$

The remaining neutrons had no time to decay before they fused with deuterons and subsequently into ${}^4\mathrm{He}^{++}$. There they stay until today because bound neutrons do not decay. The same number of protons and neutrons go into ${}^4\mathrm{He}^{++}$, and the remaining protons became hydrogen atoms when they bound with electrons later. Thus the end result of the nucleosynthesis is a universe filled with hydrogen and helium ions.

From the ratio (1.6) and the fact that the number of ${}^4\mathrm{He}$ nuclei is half the number of neutrons, the ratio of ${}^4\mathrm{He}$ to ${}^1\mathrm{H}$ is

$$X_4 \equiv \frac{N({}^4\mathrm{He})}{N({}^1\mathrm{H})} = \frac{N_n/2}{N_p - N_n} \simeq \frac{1}{12}. \tag{1.7}$$

The ratio of mass in ${}^4\mathrm{He}$ to total mass in ${}^1\mathrm{H}$ and ${}^4\mathrm{He}$ is thus

$$Y_4 \equiv \frac{4X_4}{1 + 4X_4} \simeq 0.25\,, \tag{1.8}$$

which is consistent with the observed value of 0.22-0.25 (e.g. 0.249 ± 0.001 in Tytler et al. 1996)

The prediction of helium and deuterium abundances rely on the ratio of baryon to photon number (e.g. Islam 1992). Helium will be more abundant for a greater number of baryons, while deuterium abundance is correspondingly lower. The comparison of the predicted and the observed abundances is a powerful test of the standard cosmology. At present the observation agrees with the prediction if the baryon to photon ratio η lies in the range (4-7)$\times 10^{-10}$, corresponding to $0.015 \leq \Omega_B h^2 \leq 0.026$ (e.g. chapter 1, Kolb & Turner 1990 hereafter KT; chapter 5, Roos 1994) where Ω_B is the baryonic density parameter defined as the ratio of baryonic density ρ_B to the critical density $\rho_c \equiv 3H_0^2/8\pi G$ (G is the gravitational constant). Recent measurement of the deuterium abundances in the high redshift quasar by Tytler et al. (1996) gives a value of $\Omega_B h^2 = 0.024^{+0.006}_{-0.005}$. Taking $0.5 \leq h \leq 0.85$, we get $0.02 \leq \Omega_B \leq 0.1$ which is in concordance with the observation and provides a strong support for the standard big bang cosmology.

1.5 Cosmic Microwave Background Radiation

If big bang did indeed occur about 15-20 billion years ago, then detail calculation shows that the relics of the explosion would have cooled down to a temperature of a few Kelvin above absolute zero today and the radiation should exhibit a blackbody spectrum in the microwave region. In 1964 while calibrating an antenna for satellite communication at a wavelength of $\lambda = 7.35$ cm, Arno Penzias and Robert Wilson detected a constant low level of background noise in every direction. After ruling out the technical problems with the antenna and electronics, it was concluded that the universe was emitting an excess radiation corresponding to a blackbody temperature of 3.5 K, and that this microwave radiation was coming from every direction and was unpolarised.

The instrument used at that time was crude by today's standard but since then all measurements at different wavelengths have confirmed that the spectrum is indeed blackbody. Recently, such confirmation was reinforced by a dedicated instrument, the Far Infrared Absolute Spectrophotometer (FIRAS) aboard the Cosmic Background Explorer (COBE) satellite launched in 1989. The temperature deduced from the COBE

measurements (Mather et al. 1994) is

$$T_0 = 2.726 \pm 0.01\ K. \tag{1.9}$$

1.6 Large-Scale Isotropy and Homogeneity

The expansion of the universe, helium abundance and the cosmic microwave background radiation (CMBR) all strongly endorse the standard big bang model. To understand the dynamics of the universe, one needs to be able to describe the galactic motions which follow the geodesics. Such description requires a coordinate system that is most appropriate and preferably simplest for us to follow. For that we need to know the distribution of matter (e.g. homogeneity, isotropy) so that a suitable coordinate system may be chosen.

The first assumption about the matter distribution is that of isotropy, where the universe on a large scale looks the same whichever direction an observer happens to make his/her observations. The best evidence for the isotropy of the universe is the uniformity of the temperature of the CMBR: apart from the observed dipole anisotropy which is due to the Earth's motion relative to the cosmic rest frame, the temperature difference between any two directions in the sky is less than one part in 10^4.

The second assumption is that the universe is homogeneous. Homogeneity essentially means that the large-scale distribution of matter is the same everywhere in the universe and it implies that observation made in any part of the universe is the same. So for example, an observer at another galaxy would see the same CMBR isotropy as we do in the Milky Way.

Direct evidence for the homogeneity is more tenuous. Galaxy surveys up to a distance of a few hundred Mpc do provide supporting evidence but their interpretation is not so straightforward. For a start, the redshift distances determined from equation (1.1) of Hubble's law do not give the *true* distances from us as an "excess" velocity will be induced by any small-scale inhomogeneities and this excess velocity will manifest itself in the redshift data. There are methods in which true distances can be determined from

the galaxy luminosity function discussed in section 1.9 but they all have significant errors associated with them. A more serious problem of using galaxy surveys as evidence of homogeneity is that light does not necessarily trace mass. In particular, if the mass/light ratio varies according to the environment (e.g. local density), galaxy distribution will not reflect the true distribution of mass.

There is however evidence from the peculiar velocity of the galaxies to support homogeneity. The afore-mentioned excess velocity with respect to the cosmic rest frame defined by the CMBR, or the peculiar velocity can be thought of as a galaxy's velocity after its 'Hubble expansion velocity' has been subtracted and is due primarily to any inhomogeneity. This gravitationally-induced peculiar velocity δu is in the order of (section 1.3, KT)

$$(\delta u)_\lambda \simeq \Omega_0^{0.6} \lambda H_0 \left(\frac{\delta\rho}{\rho}\right)_\lambda \tag{1.10}$$

on the scale λ, where $(\delta\rho/\rho)_\lambda$ is the fractional mass density fluctuation on the scale λ, and $\Omega_0 \equiv \rho_0/\rho_c$ is the ratio of the present mass to critical density of the universe. Peculiar velocities have been measured up to a distance of around 70 h^{-1} Mpc (e.g. Mathewson et al. 1992) and their typical values are in the order of a few hundred km/s, indicating that $(\delta\rho/\rho)_\lambda$ is in the order of 10^{-1}. Study of galaxy clustering also shows that the density fluctuation decreases towards zero with increasing scale.

Another strong argument for homogeneity comes from the debate of whether our position is unique in the universe. It is fairly well established that the universe as viewed by us is isotropic; but if the universe is not homogeneous, isotropy will disappear for an observer on galaxy other than our own. This would imply that we are living in a very special position in the whole of the universe and there is no strong theoretical argument to favour such a rare chance occupancy.

The two postulates made above are in fact the pillars of the cosmological principle, which simply states that the universe on a large scale is homogeneous and isotropic everywhere. It is important to note that isotropy does not necessarily imply homogeneity, and vice versa. However isotropy is a necessary (though not sufficient) condition for homogeneity to hold true. It is also necessary to state that homogeneity and isotropy

only hold true for any *fundamental* observer. A fundamental or comoving observer is one which moves passively with the Hubble's expansion without any peculiar velocity.

1.7 The Robertson-Walker Metric

To follow the motion of a galaxy, one can resort to the square of its space-time interval ds^2 which describes the path taken under external influence. According to the principle of least action for example, a particle will choose a path that optimise the action S and such a path is called the geodesic line. Measurement of the line element ds^2 requires both a time and space coordinate system. In Newtonian mechanics, the time is both global and unambiguous for all observers. In general relativity however, there is no global inertial frame and to construct a time coordinate which is valid globally, a set of special circumstances are necessary. Fortunately, these circumstances are satisfied by a homogeneous and isotropic universe.

To construct a global time coordinate in general relativity, first introduce a series of space-like hypersurfaces which are non-intersecting. On any one of these surfaces, the separation between any two points is space-like and galaxies lying on this surface are indeed occupying a surface of simultaneity. This series of hypersurfaces can be labelled by the proper time $x^0 = t$ of any galaxy, that is time measured by a stationary clock (defined as the clock in a frame in which the CMBR is observed to be isotropic) in the galaxy. This time turns out to be universal so that at any particular time, the positions of the galaxies lie in one of these hypersurfaces.

For the spatial movement of the galaxy, we introduce the spatial coordinates (x^1, x^2, x^3) which are constant along a geodesic. A galaxy which follows such geodesic varies only its time coordinate and is indeed classed as a fundamental observer mentioned before. The metric under such construction can be written as

$$ds^2 = c^2dt^2 - h_{ij}dx^i dx^j, \qquad (i, j = 1, 2, 3), \tag{1.11}$$

where c is the speed of light; and h_{ij} are functions of (t, x^1, x^2, x^3). A vector along a world-line of $(cdt, 0, 0, 0)$ and another which lies on the space-like hypersurface t=constant with

vector $(0, \mathrm{d}x^1, \mathrm{d}x^2, \mathrm{d}x^3)$ are clearly orthogonal by the construction of the coordinates. The geodesic equation derived from the theory of general relativity is (e.g. Islam 1992)

$$\frac{\mathrm{d}^2 x^\mu}{\mathrm{d}s^2} + \Gamma^\mu_{\lambda\nu} \frac{\mathrm{d}x^\lambda}{\mathrm{d}s} \frac{\mathrm{d}x^\nu}{\mathrm{d}s} = 0, \tag{1.12}$$

where $\Gamma^\mu_{\lambda\nu}$ is the Christoffel symbol defined by

$$\Gamma^\mu_{\lambda\nu} = \frac{1}{2} g^{\mu\sigma} (g_{\sigma\lambda,\nu} + g_{\sigma\nu,\lambda} - g_{\lambda\nu,\sigma}), \tag{1.13}$$

with $\mathrm{d}s^2 = g_{\mu\nu} \mathrm{d}x^\mu \mathrm{d}x^\nu$ $(\mu, \nu = 0, 1, 2, 3)$, and a comma denotes partial differentiation: $g_{\sigma\lambda,\nu} \equiv \partial g_{\sigma\lambda} / \partial x^\nu$.

On the hypersurface of t =constant, two galaxies with coordinates (x^1, x^2, x^3) and $(x^1 + \Delta x^1, x^2 + \Delta x^2, x^3 + \Delta x^3)$ have spatial separation of

$$\mathrm{d}l^2 = h_{ij} \Delta x^i \Delta x^j. \tag{1.14}$$

By the postulate of homogeneity and isotropy where all points and directions on a hypersurface are equivalent, a triangle formed by three nearby galaxies must, at later time, be similar to the original one on another hypersurface and that the magnification factor is independent of the three-space position of the triangle. Thus h_{ij} must have a common factor that is a function of t alone so that the ratios of small distances are the same all the times. This gives rise to the metric in the form

$$\mathrm{d}s^2 = c^2 \mathrm{d}t^2 - a^2(t) \gamma_{ij} \mathrm{d}x^i \mathrm{d}x^j, \tag{1.15}$$

where γ_{ij} are functions of (x^1, x^2, x^3) only. According to the theorem of differential geometry, homogeneity and isotropy imply a three-space that has a constant curvature which is manifested in γ_{ij}. In fact, if we choose to describe the three-space position using the spherical polar coordinates with $x^1 = r$, where r is the angular diameter distance, $x^2 = \theta$ and $x^3 = \phi$, equation (1.15) becomes the Robertson-Walker metric:

$$\mathrm{d}s^2 = c^2 \mathrm{d}t^2 - a^2(t) \left[\frac{\mathrm{d}r^2}{1 - kr^2} + r^2 (\mathrm{d}\theta^2 + \sin^2 \theta \mathrm{d}\phi^2) \right], \tag{1.16}$$

where the curvature constant k can take the values of -1,0, or +1, and $a(t)$ is called the scale factor for the reason that its value gives an indication of the size of the universe.

The proper distance l from our galaxy, chosen as the origin, to another galaxy at comoving coordinates $(r, 0, 0)$ is, by integrating the spatial part of the Robertson-Walker metric:

$$l = a(t) \int_0^r \frac{\mathrm{d}r}{\sqrt{1 - kr^2}}. \tag{1.17}$$

The recession velocity u of the galaxy is obtained by differentiating l with respect to time (denoted by a single dot above l):

$$\begin{aligned} u = \dot{l} &= \dot{a} \int_0^r \frac{\mathrm{d}r}{\sqrt{1 - kr^2}} \\ &= \frac{\dot{a}}{a} l. \end{aligned} \tag{1.18}$$

Thus as expected from the Hubble's law, the recession velocity is proportional to the distance and from equation (1.1), the Hubble constant is related to the scale factor via

$$H(t) = \frac{\dot{a}}{a}. \tag{1.19}$$

1.7.1 Light Propagation in the Robertson-Walker Metric

Astronomical data rely almost exclusively on the observations of electromagnetic radiation emitted by the source of interest and so it is important to examine the effect of light propagation in an expanding universe. Let a source at comoving coordinate $r = r_1$ emit radiation at time t_1 which is then received by another observer (say us) located at comoving coordinate $r = 0$ at time t_0; the radiation will follow a null geodesic $\mathrm{d}s^2 = 0$ along the path from (r_1, t_1) to $(0, t_0)$. The propagation of the radiation is along θ =constant and ϕ =constant, so the path r satisfies

$$\mathrm{d}t^2 - a^2(t) \frac{\mathrm{d}r^2}{1 - kr^2} = 0. \tag{1.20}$$

By integrating this equation, we have

$$\int_{t_1}^{t_0} \frac{\mathrm{d}t}{a(t)} = \int_0^{r_1} \frac{\mathrm{d}r}{(1-kr^2)^{1/2}}. \tag{1.21}$$

Suppose that the first wavecrest of the radiation was emitted at time t_1 by the source and received by us at time t_0, and the second wavecrest was emitted at time $t_1 + \delta t_1$ and reaches us at time $t_0 + \delta t_0$. Since the right hand side of equation (1.21) is the same for both wavecrests, we have

$$\int_{t_1}^{t_0} \frac{\mathrm{d}t}{a(t)} = \int_{t_1+\delta t_1}^{t_0+\delta t_0} \frac{\mathrm{d}t}{a(t)}, \tag{1.22}$$

or equivalently

$$\int_{t_1}^{t_1+\delta t_1} \frac{\mathrm{d}t}{a(t)} = \int_{t_0}^{t_0+\delta t_0} \frac{\mathrm{d}t}{a(t)}. \tag{1.23}$$

It is fair to approximate $a(t)$ to be unchanged during the interval t_1 to $t_1 + \delta t_1$ and from t_0 to $t_0 + \delta t_0$. Since the wavelength emitted by the source λ_1 is equal to $c\delta t_1$ and similarly the wavelength observed by us is $\lambda_0 = c\delta t_0$, we arrive at the following result:

$$\frac{\lambda_0}{\lambda_1} \equiv 1 + z = \frac{a(t_0)}{a(t_1)}, \tag{1.24}$$

where z quantifies the amount of redshift in wavelength being detected compared to that when the radiation was emitted. This result implies that as the universe expands, the wavelength of a photon will be redshifted due to the fact that the universe was smaller when the photon was emitted.

In the absence of the expansion, the actual distance between us and a source with intrinsic luminosity L is simply equal to the luminosity distance d_L, defined in terms of the measured flux F:

$$d_L^2 \equiv \frac{L}{4\pi F}. \tag{1.25}$$

With the expansion, the energy emitted during the time interval δt_1 will be received by the observer in a time interval $\delta t_0 = \delta t_1[a(t_0)/a(t_1)]$. Apart from that the energy of

the photon will also decrease by a factor of $a(t_1)/a(t_0)$. At the time of detection, the radiation will be distributed over a sphere of radius $4\pi a^2(t_0)r_1^2$. Therefore the observed flux is

$$\begin{aligned} F &= \frac{L}{4\pi a^2(t_0)r_1^2}\left[\frac{a(t_1)}{a(t_0)}\right]^2 \\ &= \frac{L}{4\pi a^2(t_0)r_1^2(1+z)^2}, \end{aligned} \tag{1.26}$$

and so the luminosity distance in the expanding universe is

$$d_L^2 = a^2(t_0)r_1^2(1+z)^2. \tag{1.27}$$

Suppose that the same object at coordinate $r = r_1$ has a physical size of l, then by the metric of (1.16), observer at $r = 0$ will measure an angular diameter δ of

$$\delta = \frac{l}{a(t_1)r_1}. \tag{1.28}$$

The angular diameter distance d_A defined as

$$d_A \equiv \frac{l}{\delta} = a(t_1)r_1 \tag{1.29}$$

is then related to d_L by $d_A = d_L(1+z)^2$.

1.8 Dynamics of the Universe

The Robertson-Walker metric of (1.16) tells us the geometric properties of a homogeneous and isotropic space-time. However the metric by itself does not show the dynamic evolution of the universe. For that, we need to use general relativity to relate the geometry of the space time to the source of gravitational field. These are the Einstein equations given by

$$R_{\mu\nu} - \frac{1}{2}g_{\mu\nu}R = \frac{8\pi G}{c^4}T_{\mu\nu}, \tag{1.30}$$

where $T_{\mu\nu}$ is the energy-momentum tensor of the source producing the gravitational field which for a perfect fluid with pressure p and matter four-velocity of $u^\mu \equiv \mathrm{d}x^\mu/\mathrm{d}s$ is

$$T^{\mu\nu} = (\rho c^2 + p)u^\mu u^\nu - pg^{\mu\nu}, \tag{1.31}$$

where ρc^2 is the mass-energy density. The Ricci scalar $R_{\mu\nu}$ in equation (1.30) is given as follows:

$$R_{\mu\nu} = \Gamma^\lambda_{\mu\nu,\lambda} - \Gamma^\lambda_{\mu\lambda,\nu} + \Gamma^\lambda_{\mu\nu}\Gamma^\sigma_{\lambda\sigma} - \Gamma^\sigma_{\nu\lambda}\Gamma^\lambda_{\nu\sigma}, \tag{1.32}$$

and the Ricci scalar R is defined by

$$R = g^{\mu\nu}R_{\mu\nu}. \tag{1.33}$$

With the Robertson-Walker metric of (1.16), the 00- and 11-components of equation (1.30) becomes (e.g. Roos 1994; Islam 1992)

$$\begin{aligned} \frac{\dot{a}^2 + kc^2}{a^2} &= \frac{8\pi}{3}G\rho, \\ \frac{2\ddot{a}}{a} + \frac{\dot{a}^2 + kc^2}{a^2} &= -\frac{8\pi}{c^2}Gp, \end{aligned} \tag{1.34}$$

where $\ddot{a}$ denotes the second derivative of the scale factor with respect to time. These equations are known as the Friedmann equations which were first derived in 1922 by Alexandr Friedmann. The first equation of (1.34) can be rewritten as

$$kc^2 = H_0^2 a_0^2(\Omega_0 - 1), \tag{1.35}$$

where a new parameter Ω_0 has been defined as the ratio of the present day density ρ_0 to the critical density ρ_c:

$$\Omega_0 \equiv \frac{\rho_0}{\rho_c} = \frac{8\pi G\rho_0}{3H_0^2}. \tag{1.36}$$

Since $H_0^2 a_0^2$ is positive, equation (1.35) implies that the value of k depends only on the density parameter Ω_0 and the universe is described as either closed, flat, or open as

follow:

$$\begin{aligned} \Omega_0 > 1 \quad &\Longrightarrow \quad k = +1 \quad \text{CLOSED} \\ \Omega_0 = 1 \quad &\Longrightarrow \quad k = 0 \quad \text{FLAT} \\ \Omega_0 < 1 \quad &\Longrightarrow \quad k = -1 \quad \text{OPEN.} \end{aligned} \tag{1.37}$$

Subtracting the first from the second equation of (1.34) we obtain

$$\frac{2\ddot{a}}{a} = -\frac{8\pi G}{3c^2}(\rho c^2 + 3p). \tag{1.38}$$

Today $\dot{a} \geq 0$; if in the past $(\rho c^2 + 3p)$ remained positive as it does today, then $\ddot{a}$ was always negative and at some time in the past a must have been equal to zero. This event occurred by definition at $t = 0$ and is referred to as the big bang.

From equation (1.38) it is clear that if we want a static universe in which $\dot{a} = \ddot{a} = 0$, then $\rho c^2 + 3p$ must be zero, which is somewhat odd and cannot be realised physically. Before the expansion of the universe was discovered, Einstein formulated the equations of general relativity in order to achieve a static solution by introducing the so-called 'cosmological constant' Λ in the form of $\Lambda g_{\mu\nu}$ into equation (1.30). With the discovery of the Hubble's expansion, the introduction of the cosmological constant seems somewhat unnecessary. While there is no overwhelming reason for having the cosmological constant, there is no compelling reason to exclude it either. However observations on the perihelion shift of Mercury put a constraint on the cosmological constant of $|\Lambda| < 10^{-42}\text{cm}^{-2}$ (Islam 1983) and throughout this thesis, I shall assume a value of zero for Λ.

For different values of k, the first equation of (1.34) becomes

$$\begin{aligned} \dot{a}^2 &= c^2 + \frac{8\pi G\rho a^2}{3} \qquad (k = -1) \\ \dot{a}^2 &= \frac{8\pi G\rho a^2}{3} \qquad (k = 0) \\ \dot{a}^2 &= -c^2 + \frac{8\pi G\rho a^2}{3} \qquad (k = +1). \end{aligned} \tag{1.39}$$

To see qualitatively how $a(t)$ evolves with time for different k, we begin by using the first equation of (1.34) to get $\rho a^3 = 3a(\dot{a}^2 + kc^2)/8\pi G$; differentiating this expression

and using the second equation of (1.34) we get

$$\frac{\mathrm{d}}{\mathrm{d}t}(\rho a^3) = -\frac{3a^2\dot{a}p}{c^2} = -\frac{p}{c^2}\frac{\mathrm{d}a^3}{\mathrm{d}t}. \tag{1.40}$$

Or, equivalently,

$$\frac{\mathrm{d}}{\mathrm{d}a}(\rho a^3) = -\frac{3pa^2}{c^2}. \tag{1.41}$$

From this expression we see that as long as the pressure p remains positive, the density ρ will decrease with increasing a at least as fast as a^{-3}. Thus as a tends to infinity, ρa^2 decays as least as fast as a^{-1}. In the cases of $k = -1$ and $k = 0$, equation (1.39) implies that $\dot{a}^2$ remains positive and $a(t)$ will keep on increasing. In fact for $k = -1$,

$$a(t) \to ct \quad \text{as} \quad t \to \infty. \tag{1.42}$$

In the case of $k = 0$, the decay of the ρa^2 term means that $a(t)$ will increase more slowly than t. For $k = +1$ however, the initial expansion from the big bang halts when ρa^2 reaches the value $3c^2/8\pi G$. Since $\ddot{a}$ is always negative, $a(t)$ must begin to decrease until it reaches zero sometime in the future and such event is known as the big crunch.

The dependence of the fate of the universe on the density parameter can be understood by invoking Newtonian gravity in the following manner: Consider a spherical region of size l with a total mass of M inside it. A particle at the edge of this region will be moving outward with velocity $u = H_0 l$ according to the Hubble's law. This Hubble velocity is greater than the escape velocity $u_{\mathrm{esc}} = (2GM/l)^{1/2} = (8\pi G\bar{\rho}l^2/3)^{1/2}$ if the average density inside this sphere, $\bar{\rho}$ is less than $3H_0^2/8\pi G$, the critical density ρ_c derived in equation (1.36). So for $\bar{\rho} < \rho_c$, the Hubble velocity is greater than the escape velocity and the expansion will go on indefinitely. But for $\bar{\rho} > \rho_c$, the expansion will be halted and the universe will start to contract.

Observations on luminous matter give Ω_0 (strictly speaking Ω_B) a value in the region of 0.01. However, other methods of analysis using gravitational effects of matter suggest that the total Ω could be much higher, in the region of unity. The theory of inflation also favours an $\Omega_0 = 1$ universe. Therefore it is widely believed that there is the so-called

'dark matter' that accounts for the missing mass of the universe. There are also other evidences for the existence of the dark matter from e.g. the gravitational lensing events and the flat rotation curve of our galaxy (see section 1.9).

1.8.1 Energy Conservation in the Expanding Universe

If one applies the law of mass-energy conservation in general relativity, $T^{\mu\nu}{}_{;\nu} = 0$, one will in fact arrive at the same equation (1.41), which can be rewritten in a slightly unfamiliar form:

$$\mathrm{d}\left[a^3(\rho c^2 + p)\right] = a^3 \mathrm{d}p. \tag{1.43}$$

For the simple equation of state $p = w\rho c^2$, where w is a constant, the energy density evolves in such a way that $\rho \propto a^{-3(1+w)}$. The value of w depends on the dominant constituent of the universe during the expansion. Three examples which are of cosmological interest include:

$$\begin{aligned} \text{RADIATION} \quad & (p = \frac{1}{3}\rho c^2) \implies \rho \propto a^{-4} \\ \text{MATTER} \quad & (p = 0) \implies \rho \propto a^{-3} \\ \text{VACUUM ENERGY} \quad & (p = -\rho c^2) \implies \rho \propto \text{const.} \end{aligned} \tag{1.44}$$

Radiation is the dominant component during the hot early universe. As the scale factor $a(t)$ grew with time, radiation energy density decayed more rapidly and lost its dominance over to matter and continued to do so until the present day. If the universe underwent a process called inflation, then there was a very brief interval during the very early epoch when the stress energy was dominated by vacuum energy.

To see how the scale factor evolves with time, we first notice that for $w > -1/3$ (which is satisfied by the radiation or matter-dominated universe), the curvature term in the first equation of (1.34) can be neglected in the limit of small a as

$$\frac{kc^2}{a^2} \ll \frac{8\pi}{3} G\rho. \tag{1.45}$$

Thus the first Friedmann equation simplifies to

$$\frac{\dot{a}}{a} = \left(\frac{8\pi}{3}G\rho\right)^{1/2} \propto a^{-3(1+w)/2}. \tag{1.46}$$

Supposing that this differential equation can be integrated from $t = 0$ onwards, we then have

$$a \propto t^{2/3(1+w)} \tag{1.47}$$

which leads to the following results: $a \propto t^{1/2}$ for a radiation and $a \propto t^{2/3}$ for a matter-dominated universe.

1.8.2 The Hubble Radius

During the expansion, the time scale over which the physical quantities will vary is $(\dot{a}/a)^{-1}$. The distance travelled by light during this time is defined as the Hubble radius:

$$l_H \equiv c\left(\frac{\dot{a}}{a}\right)^{-1} = cH^{-1}(t). \tag{1.48}$$

Within this length scale physical processes operate coherently and relativistic effects become important. For length scale that is much smaller than l_H, Newtonian analysis usually suffices. At present the structures that we are capable of observing are indeed much smaller than the Hubble radius today: $l_H(t_0) \simeq 3000h^{-1}$ Mpc.

However at earlier time, the structures that we see today might have evolved from regions that were super-horizon sized. The proof goes as follow: if the scale factor grows as t^n (where $n = 1/2$ for radiation and $2/3$ for matter-dominated universe), then the Hubble radius which grows faster than the scale factor ($l_H \propto t$) must have been smaller than certain length scale of interest at an earlier time. From the time when all scale of interest is bigger than l_H, smaller scale regions will become sub-horizon first before the larger one eventually does the same. This event is known as the horizon crossing and is important in analysing the structure formation theory where the distinction between relativistic and Newtonian analysis is made.

1.8.3 Evolution of Density Parameter

Here we examine how the density parameter $\Omega(t) \equiv 3H^2\rho/8\pi G$ evolves with time. As we shall see, the result has serious implication (and problems) on the standard cosmology model. The first Friedmann equation of (1.34) can be rewritten as

$$\Omega(t) = \frac{1}{1 - X(t)} \tag{1.49}$$

$$X(t) = \frac{k}{a^2}\frac{8\pi G\rho}{3} \propto \begin{cases} a^2(t) & \text{(RD)} \\ a(t) & \text{(MD)}, \end{cases} \tag{1.50}$$

where RD and MD denote radiation and matter dominated era respectively. A similar analysis of the evolution of Ω with $a(t)$ is given by Madsen & Ellis (1988). For the density parameter to evolve to the present day value of around unity, then its value in the early universe must be in the order of (KT)

$$\begin{aligned} |\Omega(10^{-43}\text{sec}) - 1| &\lesssim 10^{-60} \\ |\Omega(1\text{sec}) - 1| &\lesssim 10^{-16}. \end{aligned} \tag{1.51}$$

What the evolution of Ω tells us is that to get to the present observed value of the density parameter, then its value must be extremely close to one in the beginning of the big bang. The standard cosmological theory cannot explain why Ω should start off with such a special value. This is the so-called "flatness problem". It is this problem (along with others) that prompted the recent surge in the development of the inflation theory first proposed by Alan Guth in 1981.

1.9 Galaxies

How do large-scale structures like galaxies and clusters of galaxies form? This is the major unsolved problem every cosmologist is faced with. When considering the large-scale structure of the universe, the basic constituents can be taken to be galaxies. Galaxies range widely in their sizes, shapes, masses and luminosities. Nevertheless, a typical

galaxy can be thought of as a congregation of about 10^{11} stars bound together by their mutual gravitational attraction and has a size of 10-30 kpc. There are several exceptions at both extremes. For example, 'dwarf galaxies' have luminous masses in the range of 10^5-10^7 $M_\odot$ ($M_\odot$ is the solar mass) and radii of around 1-3 kpc while there are some giant galaxies with masses as high as 10^{13} $M_\odot$.

Galaxies are classified according to their shapes or morphology. Broadly speaking, they are divided into 'ellipticals' and 'discs'. Ellipticals are smooth, featureless, distributions of stars and contain no dust. They are found mainly in high density regions of the universe such as dense clusters of galaxies. Unlike spiral galaxies which have stars rotating about the centre, ellipticals support themselves from gravitational collapse by having stars with large random velocities. The surface brightness profiles of a typical elliptical can be adequately described by the de Vaucouleurs (1948) law:

$$I(r) = I(0)\exp(-kr^{0.25}) \equiv I_e\exp\{-7.67[(r/r_e)^{0.25} - 1]\}, \tag{1.52}$$

where r is the radial distance from the centre, the effective radius r_e is the radius containing half the total luminosity, and I_e is the surface brightness at r_e. r_e is typically $3h^{-1}$ kpc for a bright elliptical and is smaller for fainter galaxies (Kormendy 1977). The alternative formula which also fits the ellipticals well is the Hubble-Reynolds law (Reynolds 1913; Hubble 1930),

$$I(r) = \frac{I_0 r_H^2}{(r + r_H)^2}, \tag{1.53}$$

where r_H is typically $0.1r_e$. Ellipticals are classified into $E_1....E_n$ where $n = 10(a-b)/a$ with a and b being the length of the major and minor axis.

The range of luminosities L of elliptical galaxies can also be quantified by the luminosity function $\phi(L)$ which describes the relative number of galaxies at different L. The quantity $\phi(L)\mathrm{d}L$ gives the number of galaxies in the luminosity interval L to $L+\mathrm{d}L$. For ellipticals, Schechter's law (Binney & Tremaine 1987) gives the analytic approximation of:

$$\phi(L)\mathrm{d}L = n_\star \left(\frac{L}{L_\star}\right)^\alpha \exp(-L/L_\star)\frac{\mathrm{d}L}{L_\star}, \tag{1.54}$$

where n_*=1.2×10$^{-2}h^3$Mpc^{-3}; α=-1.25; and L_*=1.0×10$^{10}h^{-2}L_\odot$ (where $L_\odot$ is the solar luminosity) in the visual band (Kirshner et al. 1983). The random velocities of the stars are also useful in determining the luminosity of an elliptical via the Faber-Jackson law in which the root mean square velocity dispersion σ_v in the inner few kiloparsecs is correlated to L by

$$\sigma_v \simeq 220(L/L_*)^{0.25} \text{ kms}^{-1} \tag{1.55}$$

This relation is important in determining the *real* distance of an elliptical as opposed to the redshift distance measured from the Doppler shift of the spectrum.

The second major type of galaxy is the 'disc' (or 'spiral' as it is often called) to which our own galaxy, the Milky Way, belongs. A typical spiral has most of its visible stars contained in a flat, disc-like structure which has spiral arms extending from the centre of the disc. In addition to the disc, most spirals also contain a spheroidal distribution of stars which are distinctly different from the stars seen in the disc. These stars in the spheroidal part are, by and large, older population II stars in contrast with the population I stars found in the disc. Generally, the spheroid is comparatively small and contributes only a fraction of the total luminosity of the galaxy. In low density regions of the universe, spirals make up about 80% of the bright galaxies, but this number drops to around 10% in dense regions such as clusters.

Stars in the spirals are not distributed uniformly. Many of them are bound together in clusters. By and large, the clusters can be divided into open clusters which contain about 10^2-10^3 young population I stars, and globular clusters which have 10^4-10^6 old population II stars and are usually distributed in a spherically symmetric manner around the centre of a galaxy.

The surface brightness profile of a spiral galaxy disk also obeys an exponential function (de Vaucouleurs & Pence 1978):

$$I(r) = I_0 \exp(-r/r_d), \tag{1.56}$$

where the typical disk scale length is $r_d \simeq 3h^{-1}$ kpc, and the central brightness is $I_0 \simeq 140 L_\odot \text{pc}^{-2}$. Hubble also classified the spiral galaxies into four types, called Sa,

Sb, Sc, Sd. Along the sequence Sa→Sd, the luminosity of the spheroidal component decreases, the relative mass of the gas increases, and the spiral arms become more loosely wound.

Unlike elliptical galaxies, stars in most spiral galaxies have a circular motion about the centre and the circular speed curves are nearly flat (i.e. v_c is independent on r) at 200-300 km/s except at the centre. If the luminous matter found mainly in the centre of the galaxy contains most of the mass of the galaxy, then one would expect a decaying velocity profile with increasing r. For this reason, it has been postulated that there must be a presence of invisible or dark matter in the outer parts of the galaxy.

Another class of galaxies which are neither distinctly ellipticals nor spirals are the lenticulars. These galaxies are smooth and featureless and have disc that contain no gas, dust, bright young stars, or spiral arms, but yet obey the exponential surface brightness law of a spiral galaxy. Lenticulars are labelled by the symbol S0 in Hubble's scheme.

1.10 Structure Formation

Although the cosmological principle states that the distribution of matter in the universe is homogeneous and isotropic, clearly on a scale smaller than a few hundred Mpc, we do see non-homogeneous structures like galaxies, clusters of galaxies, superclusters of galaxy clusters, and so on. The current standard model of structure formation goes as follows: the universe was almost uniform at early times, then a small amplitude of inhomogeneity was generated by some process. The origin of this inhomogeneity is still not very well understood. The two current competing theories attribute the density fluctuations to be generated either by inflation or by the emergence of topological defects such as cosmic strings from the symmetry breaking of the Lagrangian field. Once the initial perturbations are formed, dense regions grow denser by gravitationally attracting more mass and the perturbations evolve into the structure that we see today. This hypothesis is supported by the COBE observations of the microwave background radiation where the temperature perturbations on the last scattering surface were found to be very small, implying a very smooth universe, but a small temperature perturbation

was also detected, supporting the existence of some small density fluctuations in the early universe.

To test the structure formation hypothesis, one might naturally do so by evolving some initial spatial density distribution $\rho(\mathbf{x})$ under the mathematical equations of the hypothesis in a simulation until the present day. One then compares the simulated density profile with that observed today. Unfortunately, the initial conditions required for such simulation need to be very finely tuned in order that such point to point comparison can be made. To carry out such a simulation, the initial density distributions at every point in space have to be known or assumed which is practically impossible. Instead of comparing the theoretical and the observed density profiles, a statistical approach will be more appropriate and practical in this case.

1.10.1 Correlation Function and Power Spectrum

It is more convenient to describe the density field of the universe in terms of its contrast at comoving position $\mathbf{x}$ defined by

$$\delta(\mathbf{x}) \equiv \frac{\rho(\mathbf{x}) - \bar{\rho}}{\bar{\rho}}, \tag{1.57}$$

where $\bar{\rho}$ is the mean density of the universe. The quantity $\delta(\mathbf{x})$, though easily understood is not very convenient to work with in practice. This is because the gravitational attraction at one position will influence the density field of another, and so on. Instead of working in $\mathbf{x}$ space, the statistics of the density field are easier to be dealt with in the comoving wavenumber $\mathbf{k}$ space where the magnitude $k = |\mathbf{k}|$ corresponds to $2\pi/d$ for fluctuations on the scale of d. The density perturbations in $\mathbf{k}$ space are in fact the Fourier transform of $\delta(\mathbf{x})$:

$$\delta_{\mathbf{k}} \equiv \frac{1}{(2\pi)^3} \int \delta(\mathbf{x}) \mathrm{e}^{-i\mathbf{k}\cdot\mathbf{x}} \mathrm{d}^3\mathbf{x} \tag{1.58}$$

with its inverse being

$$\delta(\mathbf{x}) \equiv \int \delta_{\mathbf{k}} \mathrm{e}^{i\mathbf{k}\cdot\mathbf{x}} \mathrm{d}^3\mathbf{k}. \tag{1.59}$$

To quantify how the density field in one place is correlated with that in another place separated by a distance of $x' = |\mathbf{x}'|$, the correlation function is defined by

$$\xi(x') \equiv \langle \delta(\mathbf{x})\delta(\mathbf{x}+\mathbf{x}')\rangle = \int \langle \delta_{\mathbf{k}}\delta_{\mathbf{k}'}\rangle e^{i\mathbf{k}\cdot\mathbf{x}} e^{i\mathbf{k}'\cdot(\mathbf{x}+\mathbf{x}')} d^3\mathbf{k} d^3\mathbf{k}', \tag{1.60}$$

where $\langle ... \rangle$ denotes averaging over an ensemble of different universes at fixed $\mathbf{x}$ and $\mathbf{x}'$. Because of homogeneity and isotropy, ξ does not depend on where $\mathbf{x}$ is, nor does it depend on the direction of $\mathbf{x}'$. Therefore $\langle \delta_{\mathbf{k}}\delta_{\mathbf{k}'}\rangle$ must involve the Dirac delta function in $\mathbf{k}$:

$$\langle \delta_{\mathbf{k}}\delta_{\mathbf{k}'}\rangle \equiv P(k)\delta^{\mathrm{D}}(\mathbf{k}+\mathbf{k}'). \tag{1.61}$$

Since $\delta(\mathbf{x})$ is real, $\delta_{\mathbf{k}}$ is complex but satisfies the relation $\delta_{-\mathbf{k}} = \delta^*_{\mathbf{k}}$ (where $\delta^*_{\mathbf{k}}$ is the complex conjugate of $\delta_{\mathbf{k}}$) and so equation (1.61) now becomes

$$\langle \delta_{\mathbf{k}}\delta^*_{\mathbf{k}'}\rangle \equiv P(k)\delta^{\mathrm{D}}(\mathbf{k}-\mathbf{k}'). \tag{1.62}$$

The quantity $P(k)$ is known as the power spectrum of the density field which by isotropy and homogeneity depends only on the magnitude of $\mathbf{k}$, and its value is $\langle |\delta_{\mathbf{k}}|^2\rangle$.

With these statistical preliminaries, the correlation function is then

$$\xi(x') = \int P(k) e^{i\mathbf{k}\cdot\mathbf{x}'} d^3\mathbf{k} \tag{1.63}$$

with complementary Fourier inverse being the power spectrum itself:

$$P(k) = \frac{1}{(2\pi)^3}\int \xi(x') e^{-i\mathbf{k}\cdot\mathbf{x}'} d^3\mathbf{r}. \tag{1.64}$$

Another important quantity of interest is the *rms* mass fluctuation or variance of the density field as it is sometime known:

$$\begin{aligned}\langle \delta^2(\mathbf{x})\rangle &= \xi(0) = \int P(k) d^3\mathbf{k} \\ &= \int 4\pi k^3 P(k)\frac{dk}{k} \\ &\equiv \int \Delta^2(k) d\ln k,\end{aligned} \tag{1.65}$$

where $\Delta^2(k) \equiv 4\pi k^3 P(k)$ represents the contribution to the variance per $\ln k$ interval.

1.11 Newtonian Treatment of Perturbations

To see how the density perturbations grow with time, we need a set of equations governing the evolution of the perturbations under the influence of external force. Whereas on the small scale such as an atom, one needs to invoke electromagnetic force to describe the particles, on the scale that is small compared to the Hubble radius $l_H \equiv cH^{-1}$ and large compared to the Schwarzschild radius, gravity will be the dominant force and classical Newtonian calculation will be more than adequate as long as the particles concerned do not move at a speed close to that of light (see section 1.8.2). For more details, readers are referred to e.g. Peebles (1980); KT; and Padmanabhan (1993).

1.11.1 Fluid Equations in Cosmology

The equations that adequately describe the density evolution in cosmology are the fluid equations in the presence of gravitational force. The fluid particles in this case are the galaxies. The standard equations for a fluid with density ρ and pressure p are

$$\begin{aligned} \left(\frac{\partial \rho}{\partial t}\right)_{\mathbf{r}} + \nabla_{\mathbf{r}} \cdot \rho \mathbf{u} &= 0, \\ \rho\left[\left(\frac{\partial \mathbf{u}}{\partial t}\right)_{\mathbf{r}} + (\mathbf{u} \cdot \nabla_{\mathbf{r}})\,\mathbf{u}\right] &= -\nabla_{\mathbf{r}} p - \rho \nabla_{\mathbf{r}} \Phi_{\mathrm{grav}}. \end{aligned} \tag{1.66}$$

The subscript $\mathbf{r}$ indicates that the spatial variable is the proper distance $\mathbf{r}$ from some chosen origin, while $\mathbf{u}$ is the proper velocity relative to the origin, and Φ_{grav} is the gravitational field. $\mathbf{r}$ is related to the comoving coordinates $\mathbf{x}$ and the scale factor $a(t)$ by $\mathbf{r} = a(t)\mathbf{x}$ and $\mathbf{u}$ is related to the peculiar velocity $\mathbf{v}$ by

$$\mathbf{u} = \dot{\mathbf{r}} = \dot{a}\mathbf{x} + \mathbf{v}\,(\mathbf{x}, t)\,. \tag{1.67}$$

The first equation of (1.66) is essentially the mass conservation equation while the second one is the Euler equation of fluid motion. On changing variables from $\mathbf{r}$ to $\mathbf{x} = \mathbf{r}/a$, one sees that the first term of the mass conservation equation becomes

$$\left(\frac{\partial}{\partial t}\right)_{\mathbf{r}} \rho(\mathbf{r}/a(t), t) = \frac{\partial \rho}{\partial t} - \frac{\dot{a}}{a}\mathbf{x} \cdot \nabla \rho, \tag{1.68}$$

where $\nabla \equiv \nabla_{\mathbf{x}}$ indicates that the spatial variable is the comoving coordinates. Equation (1.67) in the second term of mass conservation equation gives

$$\nabla_{\mathrm{r}} \cdot \rho \mathbf{u} = \frac{1}{a} \nabla \cdot \rho \mathbf{v} + \frac{3\dot{a}}{a} \rho + \frac{\dot{a}}{a} \mathbf{x} \cdot \nabla \rho. \tag{1.69}$$

The sum of equations (1.68) and (1.69) then gives the mass conservation equation in the expanding coordinates:

$$\frac{\partial \rho}{\partial t} + \frac{3\dot{a}}{a} \rho + \frac{1}{a} \nabla \cdot \rho \mathbf{v} = 0. \tag{1.70}$$

Similarly, on changing the proper to comoving coordinates and using equation (1.67), the Euler equation of motion can be expressed in the expanding coordinates. Together with equation (1.70), the fluid equations in this coordinate system read

$$\begin{aligned} \frac{\partial \delta}{\partial t} + \frac{1}{a} \nabla \cdot (1+\delta) \mathbf{v} &= 0, \\ \frac{\partial \mathbf{v}}{\partial t} + \frac{1}{a} (\mathbf{v}.\nabla) \mathbf{v} + \frac{\dot{a}}{a} \mathbf{v} &= -\frac{1}{\rho a} \nabla p - \frac{1}{a} \nabla \phi_{\mathrm{grav}}, \end{aligned} \tag{1.71}$$

where δ is the dimensionless density contrast defined in equation (1.57) and the potential Φ_{grav} has been replaced with ϕ_{grav}:

$$\Phi_{\mathrm{grav}} \equiv \phi_{\mathrm{grav}} - \frac{1}{2} a \ddot{a} x^2. \tag{1.72}$$

In the proper coordinates, the zero-zero component of the Einstein field equations for velocity $v \equiv |\mathbf{v}| \ll c$ and $\Lambda = 0$ is

$$\nabla_{\mathrm{r}}^2 \Phi_{\mathrm{grav}} = 4\pi G(\rho + 3p/c^2). \tag{1.73}$$

For zero pressure fluid, equation (1.73) implies that the potential measured by an observer in the background model is

$$\Phi_{\mathrm{b}} = \frac{2\pi G \bar{\rho}(t) r^2}{3}. \tag{1.74}$$

Using the Newtonian equation of motion $\ddot{\mathbf{r}} = -\nabla_{\mathbf{r}}\Phi_{\rm grav}$, together with equation (1.74), the cosmological equation becomes

$$\frac{\mathrm{d}^2 a}{\mathrm{d}t^2} = -\frac{4}{3}\pi G\bar{\rho}(t)a. \tag{1.75}$$

Putting equation (1.75) into (1.72) and using equation (1.73) gives

$$\nabla^2\phi_{\rm grav} = 4\pi G a^2\bar{\rho}\delta. \tag{1.76}$$

So by transforming the potential $\Phi_{\rm grav}$ to $\phi_{\rm grav}$ by virtue of equation (1.72), we have obtained a Poisson equation for this new potential. One can treat $\phi_{\rm grav}$ as the peculiar gravitational potential as the only source for $\phi_{\rm grav}$ is the perturbation in matter distribution.

1.11.2 Growth of Linear Perturbation

To proceed any further, one can assume here that the matter is only slightly perturbed from the mean background density. This is likely to be true on large scales even though nonlinear clustering is happening on small scales (Peebles 1980, §28). This assumption may also be true in some early epoch of the universe. In the linear perturbation approximation ($\delta \ll 1$), the perturbation equations become (by multiplying the first equation of (1.71) with $\mathbf{v}$ and the second by ρ and taking the divergence of the sum of both, see Peebles 1980)

$$\frac{\partial^2\delta}{\partial t^2} + 2\frac{\dot{a}}{a}\frac{\partial\delta}{\partial t} - 4\pi G\bar{\rho}\delta - \frac{v_s^2\nabla^2}{a^2}\delta = 0. \tag{1.77}$$

where $v_s^2 \equiv (\partial p/\partial\rho) = \delta p/\delta\rho$ is the square of the adiabatic sound speed with δp and $\delta\rho$ as the perturbation in pressure and density respectively. For perturbation on the scale of l such that $(v_s t/l)^2 \ll 1$ where $t \sim (G\bar{\rho})^{-1/2}$ is the free fall time, equation (1.77) reduces to

$$\frac{\partial^2\delta}{\partial t^2} + 2\frac{\dot{a}}{a}\frac{\partial\delta}{\partial t} = 4\pi G\bar{\rho}\delta. \tag{1.78}$$

The condition $(v_s t/l)^2 \ll 1$ is in fact equivalent to selecting perturbation scale such that l is much greater than the Jeans length $\lambda_J \sim v_s/(G\bar{\rho})^{1/2}$ and so one expects the structure to grow with time. For a flat ($\Omega = 1$), matter-dominated universe where $a \propto t^{2/3}$ and $6\pi G\bar{\rho}t^2 = 1$, equation (1.78) becomes

$$\frac{\partial^2\delta}{\partial t^2} + \frac{4}{3t}\frac{\partial\delta}{\partial t} = \frac{2}{3t^2}\delta \tag{1.79}$$

which has a solution of

$$\delta = A(\mathbf{x})t^{2/3} + B(\mathbf{x})t^{-1}. \tag{1.80}$$

Here the perturbation follows a power law as opposed to an exponential growth from the normal Jeans analysis in a static regime. This is because the expansion of the universe slows the exponential growth of the instability.

For an open ($\Omega < 1$) or closed ($\Omega > 1$) universe, the rate at which perturbations grow depends on the exact value of Ω (Peebles 1980). For $\Omega = 0$,

$$\delta = A(\mathbf{x}) + B(\mathbf{x})t^{-1}. \tag{1.81}$$

This implies that no structure will grow for such a low value of Ω. The growth of the perturbations for a moderate value of Ω is however only strongly suppressed if it falls below 0.1. All these analyses on the growth of structure were done on the scale that is much larger than the Jeans length and much smaller than the Hubble length. For a small-scale fluctuation where the pressure term $v_s^2\nabla^2\delta/a^2$ in equation (1.77) becomes dominant, the perturbations decay as $\delta \propto t^{-1/6}$ (Padmanabhan 1993).

So far the Newtonian growth of the linear perturbations has been discussed in the matter-dominated universe with $l \ll l_H$. In the radiation-dominated universe, relativistic analysis shows that structure that is smaller than the Hubble length l_H merely oscillates as plane waves and does not grow. The physical reason is that while the matter perturbations might have overcome the pressure support, it is the rapid expansion of the universe driven by the dominant radiation that prevents the structure that is smaller than l_H from gravitationally collapsing. For perturbations with $l > l_H$, the fluctuation grows

as $\delta \propto a^2 \propto t$. Finally, for structures that are bigger than l_H in the matter-dominated universe, perturbations evolve as $\delta \propto a \propto t^{2/3}$.

1.11.3 Hot and Cold Dark Matter

So far the ideal fluid analysis shows that perturbations on all scales larger than λ_J after matter-radiation equality will grow together in the same manner (e.g. $\delta \propto t^{2/3}$ for an $\Omega = 1$ universe) and so while the *amplitude* of the power spectrum might change with time, it should retain its *shape* throughout the matter-dominated period. The question of what the power spectrum should look like then lies crucially on what happened during and prior to the matter-radiation equality period. For perturbations on a scale that is smaller than some particular value, its growth is wiped out by certain dissipative processes which are discussed below.

The nature of the dissipation is different for baryons and dark matter. In the case of the collisionless dark matter, weakly interacting particles can freely propagate from an overdense region to an underdense one and in so doing the perturbation is erased. This process is known as 'free streaming' and it affects scales that are smaller than the free-streaming scale λ_{FS}. For the period prior to the decoupling time t_{dec} baryons are tightly coupled to the photons due to Thomson scattering. So while the photons diffuse from an overdense to an underdense region, they drag along with them the baryons, wiping out the baryon fluctuations on the scale that is smaller than the mean free path of the photon. This process is called the 'Silk damping' and the relevant mass on such scale is the Silk mass below which no structure can form.

During the period between the matter domination and decoupling, perturbations in the dark matter can grow but perturbations in baryons cannot because of their coupling with photons. After decoupling, the baryon pertubations are free to grow and they quickly fall into the potential wells created by the dark matter perturbations. Shortly afterwards, the baryon perturbations catch up with that of the dark matter and from then on they grow together.

To obtain the power spectrum once all structures start growing, it is important to

know the value of perturbations on all scales at horizon crossing time $t_{\rm enter}$. Perturbations on the scale of λ at horizon crossing, denoted $\delta_\lambda(t_{\rm enter})$, is a fundamental and important parameter in cosmology as the amplitude of the perturbations at later time is fixed by it. Without a proper model of the primeval perturbations, the fluctuation is often assumed to follow a power law:

$$\delta_\lambda(t_{\rm enter}) \propto M_\lambda^{-\alpha}, \tag{1.82}$$

where M_λ corresponds to the mass on the scale of λ.

One of the crucial unknowns in specifying the power spectrum is the dark matter constituent(s). For dark matter that is light, the free-streaming scale is large and the threshold mass corresponds to that of a supercluster. This limiting case is known as the hot dark matter (HDM) and it has a spectrum of the form (KT and references therein):

$$P(k) = Ak^{1+6\alpha} \exp[-4.61(k/k_{\rm FS})^{1.5}], \tag{1.83}$$

where $k_{\rm FS} = 0.16(m_\nu/30{\rm eV})$ Mpc^{-1} is the free streaming scale which depends on the mass of the neutrino particle m_ν (if neutrinos are the main constituent of the dark matter), and A is the unknown normalisation constant.

On the other extreme where the dark matter is heavy, the free-streaming scale is much smaller and so structure on the galactic scale can grow. This is the so-called cold dark matter (CDM) model and it has a spectrum given by

$$P(k) = \frac{Ak^{1+6\alpha}}{(1 + Bk + Ck^{1.5} + Dk^2)^2}, \tag{1.84}$$

where $B = 1.7(\Omega_0 h^2)^{-1}$ Mpc, $C = 9(\Omega_0 h^2)^{-1.5}$ Mpc$^{1.5}$, and $D = 1(\Omega_0 h^2)^{-2}$ Mpc^2.

The hot dark matter model predicts that no structure that is smaller than the free streaming scale $2\pi/k_{\rm FS} \simeq 40(m_\nu/30{\rm eV})^{-1}$ Mpc should form from the primeval spectrum; this clearly conflicts with the observation. So if hot dark matter is to be adopted as a valid model, further evolution involving some sort of fragmentation from large to small structure must be invoked.

1.12 Biasing in Galaxy Distribution

While it is possible to postulate how the mass density should evolve with various models, all the theories have to be supported by observations on the distribution of galaxies. One important question then inevitably arises: Do galaxies actually trace the underlying mass? If the distribution of mass is different from that of galaxies, it would be pointless to construct any theory based on observations of galaxies alone when possibly over 90% of the mass in the universe is in the form of dark matter.

Given that all structures on the galactic scale are most likely to be formed by gravitationally collapsing into the core of a dense region, intuitively there may be some justifications to assume that galaxies do trace mass to a certain extent. To quantify the relationship between the two, it is often proposed that

$$\frac{\delta n}{n} = b\frac{\delta \rho}{\rho}, \tag{1.85}$$

where $\delta n/n$ and $\delta\rho/\rho$ are the perturbation in galaxy and mass distribution respectively; and b is the bias parameter. The lack of complete knowledge of this bias parameter means that one usually sets it to be a scale-invariant constant. The appeal of this scale-invariant property is that it makes the calculation involving bias much easier.

Appealing as it might be, it is important to be aware that equation (1.85) is only an assumption. In fact simulation using a CDM code with this simple bias model has failed to reconcile the galaxy distribution on all scale as discussed in Coles (1993). Environmental effects such as local mass densities may influence the value of b. Other local effects that may affect the formation of galaxies are also discussed in e.g. Rees (1985) and Dekel (1986).

1.13 Peculiar Velocity

While the big bang theory predicts that the recession velocity in a homogeneous and isotropic universe should be proportional to the distance from the observer, the presence of density inhomogeneities causes the galaxies to deviate from the uniform Hubble flow

through the gravitational attraction of different regions: galaxies are attracted more strongly towards the denser regions than those that are less dense. Quantitatively, the density fluctuation generates the peculiar velocity by virtue of equations (1.71).

To see how the peculiar velocity will evolve in an expanding universe, we first take the Fourier transforms of equations (1.71) with the linear assumptions of $\delta \ll 1$ and $v \ll c$, which now simplify as

$$\begin{aligned} \dot{\delta}_{\mathbf{k}} - \frac{i\mathbf{k}}{a} \cdot \mathbf{v}_{\mathbf{k}} &= 0, \\ \frac{\mathrm{d}}{\mathrm{d}t}(a\mathbf{v}_{\mathbf{k}}) - i\mathbf{k}v_s^2\delta_{\mathbf{k}} - i\mathbf{k}\phi_{\mathbf{k}} &= 0, \end{aligned} \tag{1.86}$$

where $\mathbf{v}_{\mathbf{k}}$, $\delta_{\mathbf{k}}$ and $\phi_{\mathbf{k}}$ are the Fourier transforms of $\mathbf{v}(\mathbf{x})$, $\delta(\mathbf{x})$ and ϕ_{grav} respectively.

The peculiar velocity can be decomposed into its rotational ($\mathbf{v}_\perp$) and irrotational ($\mathbf{v}_{||}$) components:

$$\mathbf{v} = \mathbf{v}_{||} + \mathbf{v}_\perp, \quad \mathbf{v}_{\mathbf{k}} = \mathbf{v}_{||}(\mathbf{k}) + \mathbf{v}_\perp(\mathbf{k}), \tag{1.87}$$

where

$$\begin{aligned} \nabla \cdot \mathbf{v}_\perp = 0, \qquad & \nabla \times \mathbf{v}_{||} = 0, \\ \mathbf{k} \cdot \mathbf{v}_\perp(\mathbf{k}) = 0, \qquad & \mathbf{k} \cdot \mathbf{v}_{||}(\mathbf{k}) = |\mathbf{k}||\mathbf{v}_{||}(\mathbf{k})|. \end{aligned} \tag{1.88}$$

By substituting the rotational and irrotational vectors into equation (1.86), the perturbation equations become

$$\begin{aligned} &\frac{\mathrm{d}}{\mathrm{d}t}[a\mathbf{v}_\perp(\mathbf{k})] = 0 \quad \Rightarrow \quad \mathbf{v}_\perp \propto a(t)^{-1}, \\ &\mathbf{v}_{||}(\mathbf{k}) = \frac{a}{ik}\dot{\delta}_{\mathbf{k}}. \end{aligned} \tag{1.89}$$

Thus the rotational modes decay as $a^{-1}(t)$ due to the expansion. Such decay can be attributed to the law of conservation of angular momentum as the universe expands: At any time t the angular momentum of the universe of mass $M \propto \rho a^3$ is proportional to $\rho a^4 |\mathbf{v}_\perp|$. So for a matter-dominated universe where $\rho \propto a^{-3}$, the quantity $|\mathbf{v}_\perp| a$ remains constant and so the rotational velocity decays as $a^{-1}(t)$.

The only modes that grow along with the density perturbations as the universe expands are the irrotational one. So by equation (1.88) the present day velocity field should satisfy $\nabla \times \mathbf{v} = 0$, which means that the velocity could be written as a gradient of a scalar field: $\mathbf{v} = -\nabla\Phi$. This is an important hypothesis that is discussed in more detail in chapter 4.

While luminosity selection and biasing effect may seriously hamper the study of mass density from galaxy distribution, the appeal of using peculiar velocity data lies in the assumption that they are generated directly by mass perturbations, so in principle the study of peculiar velocity could give direct information on the mass distribution, irrespective of the bias relationship between light and mass.

1.13.1 Comparing Peculiar Velocity With Galaxy Survey

Although the study of peculiar velocity gives direct information on the mass distribution, the complication of the mass/light biasing means that any direct comparison between theory and observation involves not just the density parameter Ω_0, but also the bias parameter b. In fact in the linear regime, the velocity potential Φ is related to the observed perturbations $\delta n/n$ via the parameter $\beta \equiv \Omega_0^{0.6}/b$ (see section 4.2.1):

$$\nabla^2\Phi = \beta\frac{\delta n}{n}. \tag{1.90}$$

Therefore observations on the peculiar velocity and galaxy perturbations (directly in chapters 2,4,5, and indirectly in chapter 3) should give us the value of β. The determination of β is in fact very much the centre theme of this thesis.

1.14 IRAS Galaxies

Throughout this thesis, the galaxy catalogue used comes from the observations made by the Infrared Astronomical Satellite (IRAS). The mission was carried out from January to November of 1983 where the satellite measured the spectrum at wavelengths of 12, 25, 60, and 100 μm using an array of 62 infrared detectors. The resolution of the detectors

was rectangular in respect with typical sizes of 0.76'×4.6' at 12 and 25 μm, 1.5'×4.75' at 60 μm and 3'×5' at 100 μm. The positional accuracy of sources detected by IRAS depends on their size, brightness and spetral energy distribution but is usually better than 20". To be included in the IRAS catalogs a source had to be confirmed on timescales of seconds, hours and weeks. The IRAS Point Source Catalog contains about 245,000 objects. The Extragalactic catalog contains 11,444 point sources and about 1,000 small extended sources ($< 8'$).

Although its aim was to obtain a survey with full sky coverage, there are two gaps on opposite sides of the sky centered on ecliptic longitudes of 160° and 340° that were completely missed by the survey. the gaps extends 60° above and below the ecliptic plane and are 5° wide at the widest point. Apart from the two missing gaps, data inside the galactic latitude of around ±5° or more are usually excluded due to high source density confusion. More detail of the IRAS mission can be found in INFRARED ASTRONOMICAL SATELLITE (IRAS) CATALOGS AND ATLASES - EXPLANATORY SUPPLEMENT which was prepared under the supervision of the Joint IRAS Science Working Group (JISWG).

Chapter 2

The Correlation Between Bulk and Shell Velocities in Cosmology

Abstract

Previous studies have shown that the bulk velocity of a sample of elliptical galaxies nearer than 60 h^{-1} Mpc is observed to be high (599 km s^{-1}), whereas the velocity of a shell of galaxies at a distance $\sim$30 h^{-1} Mpc is much smaller, 224 km s^{-1}, and consistent with shot noise only. We investigate the significance of the small ratio of these velocities in the context of Gaussian fluctuation theories for galaxy formation. We find that the shell and bulk velocities are significantly correlated for plausible power spectra, and the possibility of such a large discrepancy between them is small ($\sim$1.5%). However, the probability rises to about 14% since the shell at 30 h^{-1} Mpc is the most extreme of a sample of ten, and we conclude that the small ratio itself does not present a serious problem for the standard model of galaxy formation from gravitational instability of Gaussian fluctuations.

We also investigate the joint distribution of the shell speed and bulk speed, as this allows us to put constraints on the density parameter of the universe. Using the power spectrum of IRAS-selected galaxies as a (possibly biased) indicator of the underlying mass power spectrum, we find acceptable solutions provided that $\Omega_0^{0.6}/b \gtrsim 1$, where b is

the IRAS bias parameter.

2.1 Introduction

If gravity is the cause of the peculiar velocities observed in the galaxy distribution, then in theory the observed peculiar velocity distribution can probe the underlying mass density distribution, namely the two-point correlation function $\xi(r)$ or the power spectrum $P(k)$. Using a catalogue of elliptical galaxies, Lynden-Bell et al. (1988) and Dressler et al. (1987b) reported a bulk flow of 599 km s^{-1} towards l=312° ± 11°, b=6° ± 10° in the Cosmic Microwave Background (CMB) frame for a sample up to a distance of 60 h^{-1} Mpc, where the Hubble constant is H_0=100 h km s^{-1} Mpc^{-1}. However, Martin-Mirones & Goicoechea (1992; hereafter MMG) reported that the shell at 30 h^{-1} Mpc is at rest in the CMB frame using the same elliptical galaxies catalogue (although their selection criteria differed from that of Lynden-Bell et al.). Motivated by this rather interesting question of whether these two results are in contradiction, Calzetti & Giavalisco (1993) attempted to reconcile these two results by using a double power law fit for $1 + \xi(r)$, instead of the usual single power law for $\xi(r)$ itself.

Calzetti & Giavalisco claimed that, with the double power-law model, it is possible to have a bulk motion larger than the ~500 km s^{-1} observed by Lynden-Bell et al. while the shell at 30 h^{-1} Mpc can have a velocity as low as ~55 km s^{-1} in the CMB frame (table 1). This is an interesting proposal, as the ratio of these quantities is (in the absence of noise) dependent only on the shape of the power spectrum, and not on its amplitude. Since the amplitude is free in most galaxy formation theories (even incorporating constraints from CMB fluctuations, if the density parameter is not fixed), the ratio could be a useful test. However, it turns out that shot noise (which was not considered by Calzetti & Giavalisco) is by no means negligible in current surveys, and this complicates the interpretation. In particular, the ratio is no longer independent of the power spectrum amplitude. In addition to the shot noise, one has to take account of the correlation between the two speeds.

Table 1. MMG solution for the motion of the Local Group with respect to various shells. Rx stands for the shell centred at x h^{-1} Mpc with semi-width of 5 h^{-1} Mpc; N is the number of galaxies in each shell; α is the angle formed between $\Delta\mathbf{v} = (\Delta v_{\rm x}, \Delta v_{\rm y}, \Delta v_{\rm z})$ and the velocity they assumed for the Local Group with respect to the CMB: $\mathbf{v}_{\rm LG} = (83, -504, 403)$ (Galactic coordinates and km s^{-1}). Note that the shell velocity in the CMB frame is independent of the $\mathbf{v}_{\rm LG}$ assumed.

Shell	N	Δv	Δv_x	Δv_y	Δv_z	α	$\cos\alpha$
R10	23	160	39	111	-107	158°	-0.93
R15	42	363	-315	-165	72	68°	0.37
R20	57	532	-424	-310	82	63°	0.45
R25	43	519	-324	-316	255	46°	0.70
R30	33	570	94	-294	480	20°	0.94
R35	28	602	470	-52	372	57°	0.55
R40	29	651	424	-66	490	51°	0.63
R45	46	704	-173	-287	619	34°	0.83
R50	41	834	-311	-731	256	35°	0.82
R55	30	852	-90	-847	32	39°	0.78

With these two issues in mind, we calculate the joint probability distribution for the two velocities (including the shot noise error, which increases the expected variance), and quantify the probability of the existence of a near-stationary shell in the environment of a large bulk flow. In section 2.3 the results of our calculations, using different power spectra, are presented and in section 2.4 we discuss the implication of the results for the theory of large-scale structure formation. We find that, for the elliptical galaxy sample analysed by Lynden-Bell et al. (1988) and MMG, the probability of the ratio of the shell to bulk speed being smaller than the observed one is $\sim$1.5 per cent. This result looks significant, but the shell at 30 h^{-1} Mpc is the most extreme of the 10 shells examined by MMG. We therefore conclude that the ratio of the bulk and shell speeds does not present a serious challenge to the standard model of galaxy formation from Gaussian fluctuations.

When we consider the joint distribution of the two speeds, we find that models with low matter amplitude are more severely challenged. Obtaining the shape of the power spectrum from IRAS galaxy clustering studies, the large bulk flow solution is difficult to attain simultaneously with a small shell speed, unless $\beta \equiv \Omega_0^{0.6}/b$ is at least unity.

2.2 Method

2.2.1 Maximum Likelihood Method for the Bulk and Shell Velocities

The interpretation of joint bulk and shell velocities requires knowledge of the correlation between them. In this section, we derive expressions for the bulk and shell velocities in terms of the Fourier coefficients of the overdensity field, $\delta_{\mathbf{k}}$. This allows us to calculate explicitly the joint distribution of the bulk and shell velocities.

The bulk and the shell velocities are determined by maximizing the likelihood func-

tion (see MMG):

$$\ln \mathcal{L} = \ln \left\{ \frac{1}{(2\pi)^{N/2} \parallel C_{ij} \parallel^{1/2}} \exp \left[-\sum_{i=1}^{N} \frac{(\mathbf{u} \cdot \hat{\mathbf{r}}_i - v_i)^2}{2\sigma_i^2} \right] \right\} \tag{2.1}$$

where v_i is the radial component of the peculiar velocity of the ith galaxy, N is the total number of galaxies or objects in the shell or bulk sample, $\sigma_i^2 = \sigma_z^2 + \sigma_{di}^2$ where σ_z and σ_{di} are the dispersions of the measured redshift z and the distance d respectively. i is the label for each galaxy or object, $C_{ij} = \mathrm{diag}(\sigma_i^2)$, $\hat{\mathbf{r}}_i$ is the unit radial vector of the ith object and $\mathbf{u}$ is the shell or bulk velocity derived when equation (2.1) is optimised. In the case of the bulk sample of Lynden-Bell et al. (1988), σ_z=365 km s^{-1} and $\sigma_{di}^2 = \Delta^2 d^2$ where Δ=0.21. In the case of the shell sample, MMG used σ_z ranging from 250 to 400 km s^{-1} depending on which shell is concerned and they used a 'mean' dispersion of $\sigma_i^2 = \sigma_z^2 + \Delta^2 (R_{\mathrm{inn}} + R_{\mathrm{out}})^2/4$ where R_{inn} and R_{out} are the inner and outer radii of the shell. Minimising equation (2.1) by $\partial \ln \mathcal{L}/\partial u^\alpha = 0$ (where α=1,2,3) gives:

$$\sum_{i=1}^{N} \frac{u^\beta \hat{r}_i^\beta \hat{r}_i^\alpha}{\sigma_i^2} = \sum_{i=1}^{N} \frac{v_i \hat{r}_i^\alpha}{\sigma_i^2}. \tag{2.2}$$

Replacing the discrete sum by the integral with the appropriate selection function $\phi(r)$ and using $v_i = \mathbf{v} \cdot \hat{\mathbf{r}}_i$, $\mathbf{u}$ is then (assuming uniform sky coverage – see Kaiser (1988) for the general case)

$$u^\alpha = 3 \int (\mathbf{v} \cdot \hat{\mathbf{r}}) \hat{r}^\alpha W(r) \mathrm{d}^3\mathbf{r} \tag{2.3}$$

where

$$W(r) \equiv \frac{\phi(r)}{\sigma^2(r) \int \frac{\phi(r')}{\sigma^2(r')} \mathrm{d}^3\mathbf{r}'}. \tag{2.4}$$

The selection function was obtained from Lynden-Bell et al. (1988) and MMG. With a Fourier expansion for $\mathbf{v}(\mathbf{r}) = \int \mathbf{v}(\mathbf{k}) \mathrm{e}^{\mathrm{i}\mathbf{k}\cdot\mathbf{r}} \mathrm{d}^3\mathbf{k}$, equation (2.3) can be written:

$$u^\alpha = 12\pi \int \int W(r) r^2 j_2(kr) v^\alpha(\mathbf{k}) \mathrm{d}r \mathrm{d}^3\mathbf{k} \tag{2.5}$$

where $2j_2(kr) = \int_{-1}^{+1} \mu^2 \mathrm{e}^{\mathrm{i}kr\mu}\mathrm{d}\mu$. In proper units, $\mathbf{v}(\mathbf{k}) = \mathrm{i}fH\frac{\mathbf{k}}{k^2}\delta_{\mathbf{k}}$ (Peebles 1980), where $f \simeq \Omega_0^{0.6}$, H is the Hubble constant and $\delta_{\mathbf{k}}$ refers to the mass density fluctuation in k space. The result of all these is to give

$$u^{\alpha} = \mathrm{i}fH \int W(k)\hat{k}^{\alpha}\delta_{\mathbf{k}}\mathrm{d}^3\mathbf{k} \tag{2.6}$$

where the window function is

$$W(k) \equiv \frac{12\pi}{k} \int r^2 W(r) j_2(kr)\mathrm{d}r. \tag{2.7}$$

The quantity $\sigma_{ij}^2 = \frac{1}{3}\langle \mathbf{u}_i \cdot \mathbf{u}_j \rangle$ (where the bracket denotes the average value and i,j denote s (shell) or b (bulk) term) is required to calculate the joint distribution of the velocities (section 2.2.3):

$$\sigma_{ij}^2 = -\frac{f^2H^2}{3} \int W_i(k)W_j(k')\langle \delta_{\mathbf{k}}\delta_{\mathbf{k}'}\rangle \hat{\mathbf{k}} \cdot \hat{\mathbf{k}}' \mathrm{d}^3\mathbf{k}\mathrm{d}^3\mathbf{k}'. \tag{2.8}$$

From homogeneity (e.g. Bertschinger 1991),

$$\langle \delta_{\mathbf{k}}\delta_{\mathbf{k}'}\rangle = \delta^{\mathrm{D}}(\mathbf{k}+\mathbf{k}')P_{\mathrm{mass}}(k), \tag{2.9}$$

where δ^{D} is the Dirac delta function, and $P_{\mathrm{mass}}(k)$ is the matter power spectrum. We estimate $P_{\mathrm{mass}}(k)$ from the power spectrum $P(k)$ of a galaxy catalogue, and assume a bias parameter b such that $P(k) = b^2 P_{\mathrm{mass}}(k)$. Therefore the one-dimensional variances may be written:

$$\begin{aligned}
\sigma_{ss}^2 &= \frac{\beta^2H^2}{3} \int P(k)|W_s(k)|^2\mathrm{d}^3\mathbf{k} \\
\sigma_{BB}^2 &= \frac{\beta^2H^2}{3} \int P(k)|W_B(k)|^2\mathrm{d}^3\mathbf{k} \\
\sigma_{sB}^2 &= \frac{\beta^2H^2}{3} \int P(k)W_s(k)W_B^*(k)\mathrm{d}^3\mathbf{k}
\end{aligned} \tag{2.10}$$

with $\beta \equiv \Omega_0^{0.6}/b$. To this we must add the shot noise which is calculated in the next section. If we are using distance in the unit of h^{-1} Mpc and k in h Mpc^{-1}, then effectively

H=100 in equation (2.10). Figure 2.1 shows $W(r)$ in equation (2.4) for the shell and bulk samples, and figure 2.2 shows $|kW(k)|^2$ in equation(2.7).

The window functions $|W(k)|^2$ drop quite sharply at high k, even for the shell sample which is narrow in real space. For this reason the linear theory relation between $\mathbf{v(k)}$ and $\delta_{\mathbf{k}}$ should be valid for the analysis. To illustrate that this is the case, the fraction of σ_{ss}^2 coming from the nonlinear part $k > 0.29\ h$ Mpc^{-1} of the spectra considered later in this paper is only $\lesssim$0.4 per cent. The broad similarity of the two curves in figure 2.2 indicates that the bulk and shell velocities will be correlated. The bulk sample we have used in this paper runs from $r = 0$ to 60 h^{-1} Mpc and, for the shell sample, r is from 25 to 35 h^{-1} Mpc.

2.2.2 Noise from the Peculiar Velocity Measurement

In equation (2.3) for u^α, the $\mathbf{v}\cdot\hat{\mathbf{r}}$ term in the integrand is the radial peculiar velocity, which is related to the true peculiar velocity $\mathbf{v}_\mathrm{t}$ by $\mathbf{v}\cdot\hat{\mathbf{r}} = \mathbf{v}_\mathrm{t}\cdot\hat{\mathbf{r}} + \varepsilon(\mathbf{r})$ where $\varepsilon(\mathbf{r})$ is the dispersion $\sigma(r)$ due to the distance and redshift errors (Kaiser & Lahav 1987). The σ_{ij}^2 in equation (2.8) is then

$$\langle u_i^\alpha u_j^\beta\rangle = \langle u_{i\mathrm{S}}^\alpha u_{j\mathrm{S}}^\beta\rangle + \langle u_{i\mathrm{N}}^\alpha u_{j\mathrm{N}}^\beta\rangle, \tag{2.11}$$

where the first term is the signal from $\mathbf{v}_\mathrm{t}\cdot\hat{\mathbf{r}}$ and the second term is the shot noise from $\varepsilon(\mathbf{r})$. There is no cross-term between the signal and the noise since $\mathbf{v}_\mathrm{t}\cdot\hat{\mathbf{r}}$ and $\varepsilon(\mathbf{r})$ are uncorrelated. From equation (2.3), the shot noise is

$$\langle u_{i\mathrm{N}}^\alpha u_{j\mathrm{N}}^\beta\rangle = 9\langle\int \varepsilon(\mathbf{r})\varepsilon(\mathbf{r}')W_i(r)W_j(r')\hat{r}^\alpha\hat{r}'^\beta \mathrm{d}^3\mathbf{r}\mathrm{d}^3\mathbf{r}'\rangle. \tag{2.12}$$

If we split the integration volume up into many small cells labelled by I (or J) each containing either n_I (or n_J) = 0 or 1 galaxy, then

$$\langle u_{i\mathrm{N}}^\alpha u_{j\mathrm{N}}^\beta\rangle = \sum_I\sum_J \hat{r}_I^\alpha\hat{r}_J^\beta\langle n_{iI}n_{jJ}\varepsilon_I\varepsilon_J\rangle W_i(r_I)W_j(r_J). \tag{2.13}$$

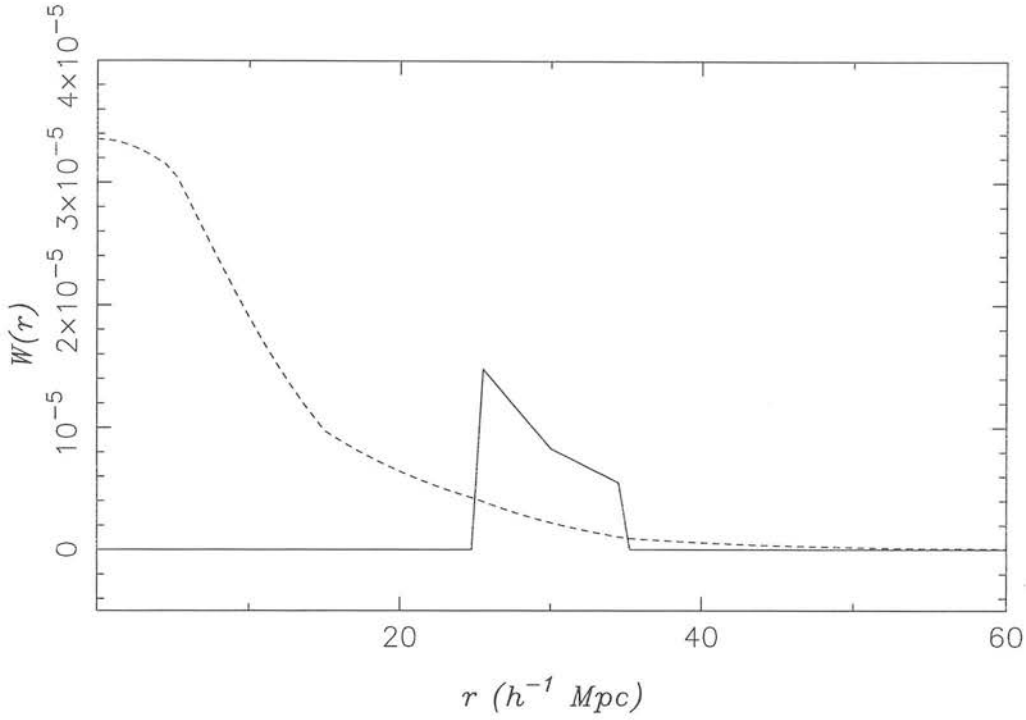

Figure 2.1: Normalised radial distribution $W(r)$ (see equation (2.4)) for the shell sample R30 (solid) and the bulk sample from r=0 to 60 h^{-1} Mpc (dashed).

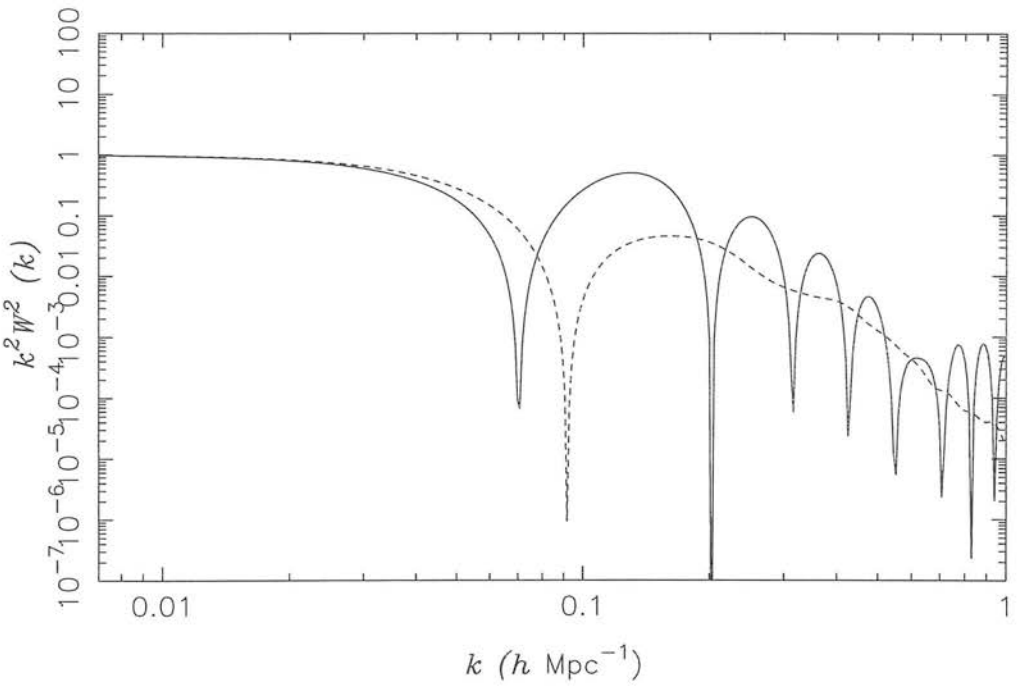

Figure 2.2: Window functions $k^2W^2(k)$ (see equation (2.7)) for the two samples as in figure 2.1.

For $i = j$ (i.e. shell-shell or bulk-bulk term), $n_{iI}n_{jJ} = n_{iI} = 0$ or 1, and the galaxy errors are uncorrelated, $\langle \varepsilon_I \varepsilon_J \rangle = \sigma_I^2 \delta_{IJ}^{\rm K}$ where $\delta_{IJ}^{\rm K}$ is the Kronecker delta. With $\langle n_{iI} \rangle = \phi_i \delta^3 \mathbf{r}$, conversion of the sum (2.13) to an integral gives

$$\langle u_{i\rm N}^{\alpha} u_{i\rm N}^{\beta} \rangle = \frac{3}{4\pi \int {\rm d}r \phi_i r^2 / \sigma_i^2(r)} \delta_{\alpha\beta}^{\rm K}. \tag{2.14}$$

For $i \neq j$ (i.e. shell-bulk term), we note from MMG and Lynden-Bell et al. (1988) that the sample in MMG for the shell analysis is a sub-sample of that used by Lynden-Bell et al. for the bulk flow. Therefore $\langle n_{sI} n_{BJ} \rangle = \langle n_{sI} \rangle = \phi_{sI} \delta^3 \mathbf{r}$ and

$$\langle u_{s\rm N}^{\alpha} u_{B\rm N}^{\beta} \rangle = \frac{3}{4\pi} \frac{\int r^2 {\rm d}r \phi_s(r) / \left[\sigma_s(r) \sigma_B(r) \right]}{\int {\rm d}r \phi_s r^2 / \sigma_s^2(r) \int {\rm d}r \phi_B r^2 / \sigma_B^2(r)} \delta_{\alpha\beta}^{\rm K}. \tag{2.15}$$

The result of adding the noise to equation (2.10) is

$$\begin{aligned}
\sigma_{ss}^2 &= \frac{\beta^2 H^2}{3} \int P(k) |W_s(k)|^2 {\rm d}^3\mathbf{k} + \frac{3}{4\pi \int {\rm d}r \phi_s r^2 / \sigma_s^2(r)} \\
\sigma_{BB}^2 &= \frac{\beta^2 H^2}{3} \int P(k) |W_B(k)|^2 {\rm d}^3\mathbf{k} + \frac{3}{4\pi \int {\rm d}r \phi_B r^2 / \sigma_B^2(r)} \\
\sigma_{sB}^2 &= \frac{\beta^2 H^2}{3} \int P(k) W_s(k) W_B^*(k) {\rm d}^3\mathbf{k} \\
&\quad + \frac{3}{4\pi} \frac{\int r^2 {\rm d}r \phi_s(r) / \left[\sigma_s(r) \sigma_B(r) \right]}{\int {\rm d}r \phi_s r^2 / \sigma_s^2(r) \int {\rm d}r \phi_B r^2 / \sigma_B^2(r)}.
\end{aligned} \tag{2.16}$$

The computed shell velocity has a noise of $\sqrt{3\langle u_{s\rm N}^{\alpha} u_{s\rm N}^{\alpha} \rangle}$= 367 km s^{-1} while the bulk velocity has a noise of $\sqrt{3\langle u_{B\rm N}^{\alpha} u_{B\rm N}^{\alpha} \rangle}$=124 km s^{-1}, so we see that the measured shell velocity could be entirely due to noise, whereas the bulk velocity is detected at a high signal-to-noise ratio.

2.2.3 Probability Distribution of the Bulk and Shell Velocities

For Gaussian fluctuations, the joint distribution of the six variables $x_i = (u_s^{\alpha}, u_B^{\beta})$ is a multivariate Gaussian:

$$\begin{aligned}
p(x_i) {\rm d}^6 x_i &= \frac{1}{(2\pi)^3 \parallel M_{ij} \parallel^{1/2}} \times \\
&\quad \exp\left[-\frac{1}{2} (x_i - \bar{x}_i) M_{ij}^{-1} (x_j - \bar{x}_j) \right] {\rm d}^6 x_i
\end{aligned} \tag{2.17}$$

where

$$M_{ij} \equiv \langle (x_i - \bar{x}_i)(x_j - \bar{x}_j) \rangle \tag{2.18}$$

and

$$\begin{aligned} \langle u_s^\alpha u_B^\beta \rangle &= \sigma_{sB}^2 \delta_{\alpha\beta}^{\rm K} \\ \langle u_s^\alpha u_s^\beta \rangle &= \sigma_{ss}^2 \delta_{\alpha\beta}^{\rm K} \\ \langle u_B^\alpha u_B^\beta \rangle &= \sigma_{BB}^2 \delta_{\alpha\beta}^{\rm K}. \end{aligned} \tag{2.19}$$

Equation (2.17) is then

$$\begin{aligned} p(x_i){\rm d}^6 x_i = & \frac{1}{(2\pi)^3(\sigma_{ss}^2\sigma_{BB}^2 - \sigma_{sB}^4)^{3/2}} \times \\ & \exp\left[-\frac{u_s^2\sigma_{BB}^2 + u_B^2\sigma_{ss}^2 - 2\mathbf{u}_s \cdot \mathbf{u}_B \sigma_{sB}^2}{2(\sigma_{ss}^2\sigma_{BB}^2 - \sigma_{sB}^4)} \right] {\rm d}^6 x_i. \end{aligned} \tag{2.20}$$

Rewriting equation (2.20) in terms of $|\mathbf{u}_s|$,$|\mathbf{u}_B|$ and $\mu = \hat{\mathbf{u}}_s \cdot \hat{\mathbf{u}}_B$:

$$\begin{aligned} p(u_s, u_B, \mu){\rm d}u_s{\rm d}u_B{\rm d}\mu = & \frac{u_s^2 u_B^2}{\pi\Gamma^{3/2}} \times \\ & \exp\left[-\frac{(u_s^2\sigma_{BB}^2 + u_B^2\sigma_{ss}^2 - 2u_s u_B \mu \sigma_{sB}^2)}{2\Gamma} \right] {\rm d}u_s{\rm d}u_B{\rm d}\mu \end{aligned} \tag{2.21}$$

where $\Gamma = (\sigma_{ss}^2\sigma_{BB}^2 - \sigma_{sB}^4)$. Equation (2.21) is essentially the same as equation (8) of Peacock (1992). For our purpose, it would be more useful to work out the probability distribution of the shell-bulk velocity ratio rather than the absolute magnitude of $\mathbf{u}_s$ and $\mathbf{u}_B$. For that we define two new parameters (see Peacock 1992):

$$\begin{aligned} A &\equiv \mu \frac{\sigma_{sB}^2}{\sigma_{ss}\sigma_{BB}} \equiv \mu r \\ B &\equiv \frac{u_s}{u_B}\frac{\sigma_{BB}}{\sigma_{ss}} \equiv \frac{u_s}{u_B} F. \end{aligned} \tag{2.22}$$

In terms of A and B, $p(u_s, u_B, \mu)$ can be rewritten as:

$$p(A, B){\rm d}A{\rm d}B = \frac{8B^2(1-r^2)^{3/2}}{\pi r(1 + B^2 - 2AB)^3}{\rm d}A{\rm d}B. \tag{2.23}$$

To obtain the distribution of velocity ratio $R = u_s/u_B$, equation (2.23) is integrated from $A = -r$ to $A = r$ which gives:

$$p(R)\mathrm{d}R = \frac{16F^3R^2(1-r^2)^{3/2}(1+F^2R^2)}{\pi[(1+F^2R^2)^2 - 4r^2F^2R^2]^2}\mathrm{d}R. \tag{2.24}$$

To obtain the distribution in μ, equation (2.23) is integrated from $B = 0$ to $B = \infty$ which yields

$$p(\mu)\mathrm{d}\mu = \frac{3\mu r(1-r^2)^{3/2}}{\pi(1-\mu^2r^2)^2} + \frac{(1-r^2)^{3/2}(1+2\mu^2r^2)}{\pi(1-\mu^2r^2)^{5/2}}\left[\frac{\pi}{2} - \tan^{-1}\left(\frac{-\mu r}{\sqrt{1-\mu^2r^2}}\right)\right]\mathrm{d}\mu. \tag{2.25}$$

To complete our analysis, we also integrate equation (2.21) from $\mu = -1$ to $\mu = +1$ to get

$$p(u_s,u_B)\mathrm{d}u_s\mathrm{d}u_B = \frac{u_su_B}{\pi\Gamma^{1/2}\sigma_{sB}^2}\times \left\{\exp\left[-\frac{(u_s^2\sigma_{BB}^2 + u_B^2\sigma_{ss}^2 - 2u_su_B\sigma_{sB}^2)}{2\Gamma}\right] - \exp\left[-\frac{(u_s^2\sigma_{BB}^2 + u_B^2\sigma_{ss}^2 + 2u_su_B\sigma_{sB}^2)}{2\Gamma}\right]\right\}\mathrm{d}u_s\mathrm{d}u_B. \tag{2.26}$$

2.3 Results

It is clear that the interpretation of the shell-bulk ratio is dependent on the power spectrum $P(k)$. To calculate the joint probability distribution, we consider two parametrised forms for the power spectrum. We take the empirical power spectrum of Peacock & Dodds (1994), obtained from fits to a variety of galaxy catalogues:

$$\Delta^2(k) = \frac{(k/k_0)^\alpha}{1+(k/k_c)^{\alpha-\beta}}, \tag{2.27}$$

with k_0=0.29±0.01 h Mpc^{-1}, k_c=0.039±0.002 h Mpc^{-1}, α=1.5±0.03, and β=4.0±0.5. Note that, since the shapes of the power spectra of the catalogues used are similar (Peacock 1991), it is plausible that, at least on the reasonably large scales used here,

the mass power spectrum will also have the same shape. The only variable then is the normalisation of the matter power spectrum, which can be expressed in terms of the bias parameter of any of the catalogues. We have chosen to express the matter power spectrum in terms of the IRAS power spectrum, for which (2.27) is a reasonable fit; we will then obtain constraints involving the IRAS bias parameter. This, of course, is entirely independent of the elliptical galaxy sample which has been used to trace the peculiar velocity field. We note in passing that spirals and ellipticals give qualitatively the same velocity fields (Dekel 1994). In addition to this empirical power spectrum, we also consider a CDM-like power spectrum with a shape parameter Γ (Kolb & Turner 1990):

$$P(k) = \frac{Ak^n}{(1 + yk + wk^{1.5} + \gamma k^2)^2}, \tag{2.28}$$

where $y = 1.7\Gamma^{-1}h^{-1}$ Mpc, $w = 9\Gamma^{-1.5}h^{-1.5}$ Mpc$^{1.5}$, $\gamma = 1.0\Gamma^{-2}h^{-2}$ Mpc^2, n=1 for the Harrison-Zeldovich spectrum, and A is the normalisation factor. We allow Γ to be a free parameter, bearing in mind that $\Gamma = \Omega_0 h = 0.5$ in the standard CDM scenario, and $\Gamma \simeq 0.2$ is an approximate fit to the galaxy data. A is chosen to be normalised to the COBE spectrum (Efstathiou et al. 1992) for the spatially flat models:

$$A = \frac{3}{20\pi}\left(\frac{Q_{\rm rms}}{T_0}\right)^2\left(\frac{2c}{H_0}\right)^4\Omega_0^{-1.54}, \tag{2.29}$$

where $Q_{\rm rms} = 19.4^{+2.3}_{-2.1}$ μK (Banday et al. 1994), T_0 is the mean temperature of the background radiation ($T_0 = 2.735 \pm 0.006$K), and c is the speed of light. Figure 2.3 shows the plot of these two power spectra with Γ=0.2 for equation (2.28).

For the power spectrum of Peacock & Dodds (1994), figures 2.4 and 2.5 show the plots of the probability distributions $p(R)$ and $p(\mu)$ (see equations (2.24) and (2.25)) with β=0.1, 0.5, 1.0 and 1.5 for the R30 shell and a bulk radius of 60 h^{-1} Mpc. We also calculated the probability that the shell-bulk velocity ratio is smaller than 0.4; and in this case the probability turns out to be around 0.3 per cent–1.6 per cent depending on the value of β, with a value of 1.5 per cent being favoured by recent determinations of $\beta \simeq 1$ (e.g. Heavens & Taylor 1995). Varying β alters the amplitude of the matter power spectrum, if Ω_0 is fixed, and the distribution of the shell-bulk ratio then changes only

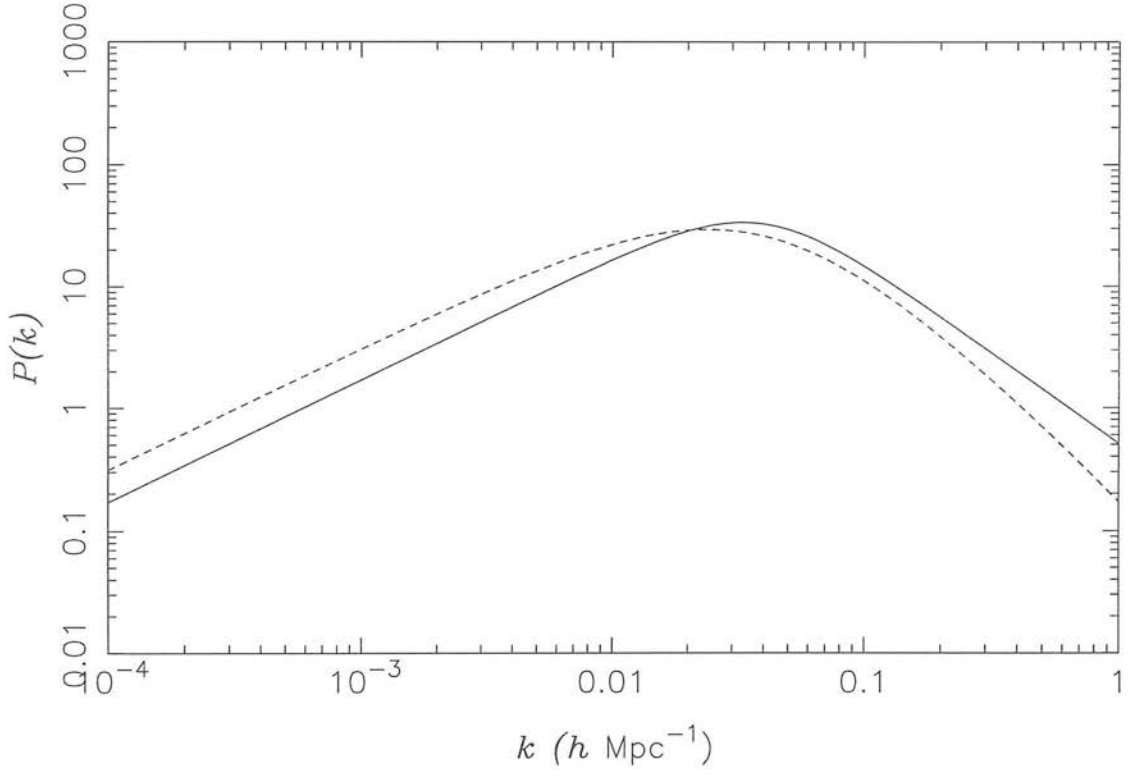

Figure 2.3: Power spectrum $P(k)$. The solid line represents the galaxy power spectrum of Peacock & Dodds (1994) while the dashed line represents the CDM model normalised to COBE with $\Gamma = 0.2$ and $\Omega_0 = 1$.

Table 2. Results of $\sqrt{3}\sigma_{ss}$, $\sqrt{3}\sigma_{BB}$ (in km s^{-1}), the correlation coefficient r, the percentage chance of u_s/u_B being smaller than 0.4, and the integral $\int p$ over $p \leq p(u_s = 240, u_B = 600)$ (in per cent) for different values of β for the power spectrum of Peacock & Dodds (1994). Note that the rms shell and bulk velocities are $\sqrt{3}\sigma_{ss}$ and $\sqrt{3}\sigma_{BB}$.

	$\sqrt{3}\sigma_{ss}$	$\sqrt{3}\sigma_{BB}$	r	$p(R < 0.4)/\%$	$\int p/\%$
$\beta = 0.1$	369	129	0.35	0.4	2.1×10^{-12}
$\beta = 0.5$	413	213	0.50	0.9	1.2×10^{-3}
$\beta = 1.0$	529	367	0.67	1.5	1.9
$\beta = 1.5$	679	533	0.75	1.6	10.4

as a result of the difference in the relative contribution from shot noise. Table 2 shows the results of $\sqrt{3}\sigma_{ss}$, $\sqrt{3}\sigma_{BB}$, the correlation coefficient r, and the percentage chance of $u_s \leq 0.4u_B$ for different values of β. We apply a slightly less stringent ratio than the observed one, since the solar motion with respect to the CMB used by Lynden-Bell et al. has a modest error. The high value of the correlation coefficient r suggests that the shell and the bulk velocities are strongly correlated, and so it is unusual to find a stationary shell in a large bulk flow environment for this power spectrum. Indeed, inspection of the window function (figure 2.2) suggests that, with almost any smooth $P(k)$, the shell and bulk velocities will be strongly correlated, unless the variances are completely dominated by shot noise. In passing, we note that the cosine of the misalignment angle, $\mu = 0.62$, is quite compatible with the results shown in figure 2.5.

It is important to note that the 1.5 per cent probability is not as significant as it appears, since this shell has been chosen for analysis as the most extreme of a sample of N=10. If all shells had the same $p(R \leq 0.4)$, then the probability of the most extreme R being ≤ 0.4 would be $1 - (1 - 0.015)^{10}$=14 per cent $\simeq Np(R \leq 0.4)$.

The results for the COBE-normalised flat CDM-like models are shown in table 3, with the probability distributions $p(R)$ shown in figure 2.6. Once again we find consistently a probability of about 1.5 per cent for $u_s \leq 0.4\,u_B$. The results are insensitive to the

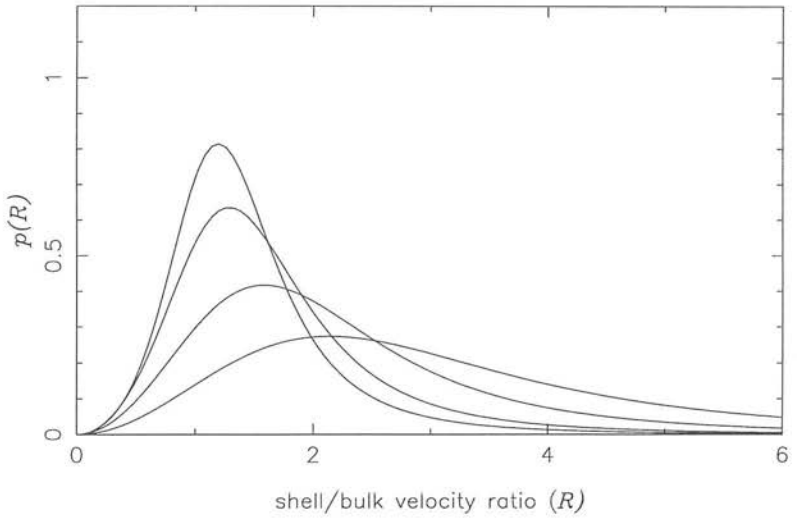

Figure 2.4: Probability distribution $p(R)$ of $R = u_s/u_B$ for the R30 shell at 30 h^{-1} Mpc and a bulk radius of 60 h^{-1} Mpc. The power spectrum used is that from Peacock & Dodds (1994) and the values of β chosen are, in order of increasing peak height, 0.1, 0.5, 1.0, and 1.5.

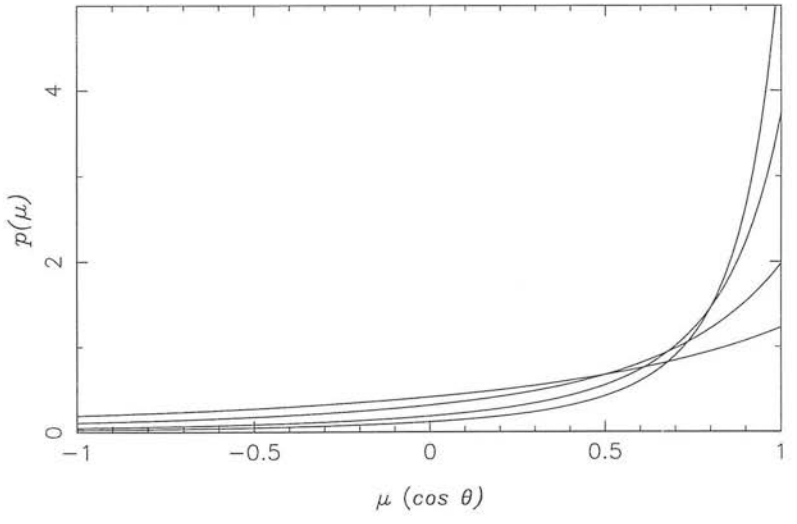

Figure 2.5: Probability distribution $p(\mu)$ of $\mu = \hat{\mathbf{u}}_s \cdot \hat{\mathbf{u}}_B$ for the R30 shell at 30 h^{-1} Mpc and a bulk radius of 60 h^{-1} Mpc using the power spectrum of Peacock & Dodds (1994). The values of β chosen are, in increasing order at the right of the graph, 0.1, 0.5, 1.0, and 1.5.

Table 3. Results of $\sqrt{3}\sigma_{ss}$, $\sqrt{3}\sigma_{BB}$ (in km s^{-1}), the correlation coefficient r, the percentage chance of u_s/u_B being smaller than 0.4, and the integral $\int p$ over $p \leq p(u_s = 240, u_B = 600)$ (in per cent) for different values of Γ and Ω_0 for the CDM-like model normalised to COBE. As the COBE temperature variations arise from mass fluctuations, the effective bias parameter b is unity.

	Ω_0:	0.1	0.5	1.0	1.5
$\Gamma = 0.2$	$(\sqrt{3}\sigma_{ss})$	653	551	518	501
	$(\sqrt{3}\sigma_{BB})$	518	400	341	339
	(r)	0.76	0.70	0.68	0.66
	$(p(R \leq 0.4))$	1.6	1.6	1.5	1.5
	$(\int p)$	8.6	2.8	0.7	0.9
$\Gamma = 0.3$	$(\sqrt{3}\sigma_{ss})$	793	650	599	575
	$(\sqrt{3}\sigma_{BB})$	620	478	430	404
	(r)	0.76	0.72	0.69	0.68
	$(p(R \leq 0.4))$	1.6	1.6	1.5	1.5
	$(\int p)$	14.7	7.5	4.8	3.5
$\Gamma = 0.5$	$(\sqrt{3}\sigma_{ss})$	1037	824	750	714
	$(\sqrt{3}\sigma_{BB})$	752	577	516	483
	(r)	0.71	0.69	0.68	0.67
	$(p(R \leq 0.4))$	1.5	1.5	1.5	1.4
	$(\int p)$	17.3	14.1	11.0	8.9

value of Ω_0 since the normalisation of the amplitude of the power spectrum $\propto \Omega_0^{-0.77}$ more-or-less cancels the growth rate $\propto \Omega_0^{0.6}$.

In figure 2.7, we show the joint distribution of shell and bulk speeds, for a variety of models. The striking aspect of this is that the high amplitude of the bulk flow is difficult to achieve unless the matter power spectrum has high amplitude. Tables 2 and 3 show the probability of the observations lying outside the contour passing through u_s=240, u_B=600 km s^{-1}. We see a consistent story with the ratio test: low-amplitude

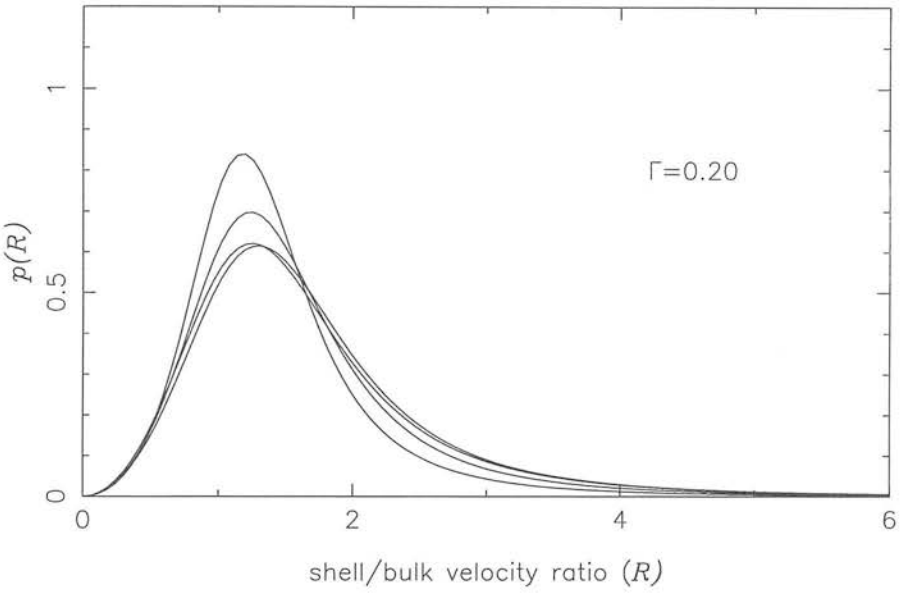

(a) $\Gamma = 0.2$

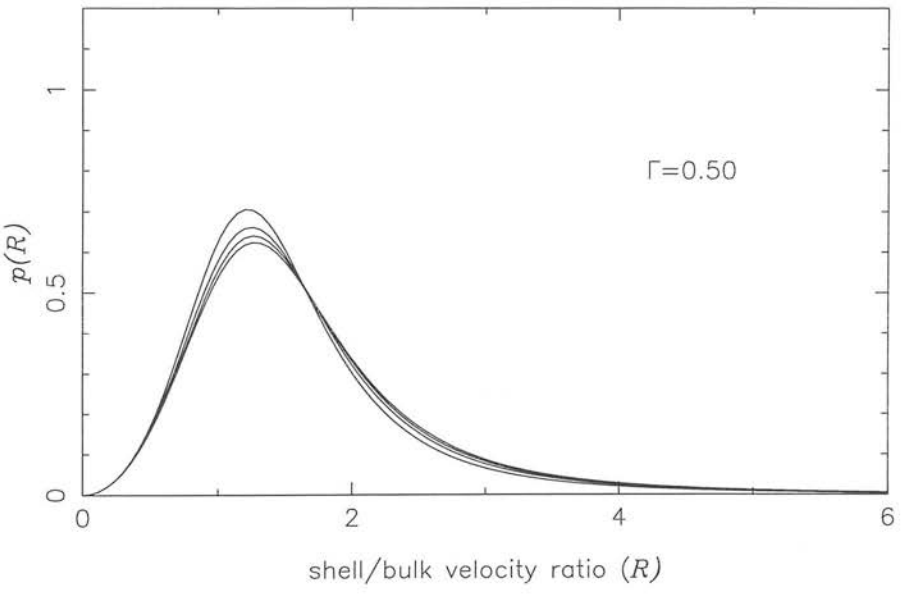

(b) $\Gamma = 0.5$

Figure 2.6: The distribution of the shell-bulk velocity ratio for the CDM-like models normalised to COBE with Γ= (a) 0.2 and (b) 0.5, for values of Ω_0, in decreasing order of peak height, of 0.1, 0.5, 1 and 1.5.

models with $\beta \lesssim 1$ are strongly excluded, but the probability is $\sim$1 per cent for the high-amplitude β=1 model and the COBE-normalised Γ=0.2 model.

2.4 Discussion

We have calculated the joint distribution for the shell and bulk velocities, concentrating on the probability distribution for the ratio of the two magnitudes, assuming Gaussian fluctuations. The main motivation for this is that the ratio is, in the absence of noise, a test of the shape of the power spectrum, independent of its amplitude. In practice this turns out not to be the case, since shot noise in the shell velocities of current surveys is very large, and the shell solutions tend to be of limited use. However, the joint distribution of shell and bulk speeds can be used effectively to test galaxy formation models, provided that the noise and correlation are correctly accounted for.

We have applied the analysis to the shell of galaxies at $30\pm5\ h^{-1}$ Mpc investigated by MMG, and the bulk elliptical galaxy sample within $60\ h^{-1}$ Mpc of Lynden-Bell et al. (1988). We find that the probability of the ratio of the shell and bulk speeds being lower than the observed one is approximately 1.5 per cent, for power spectra of the shape required to fit the galaxy data and amplitude and Ω_0 sufficient to account for the magnitude of the bulk motion. Since we have considered the most extreme shell (of ten) in the MMG sample, we conclude that the small observed ratio does not itself present any serious challenge to the standard model of galaxy formation, i.e. gravitational instability of initially Gaussian fluctuations.

We have made two simplifying assumptions in the analysis. First, the sky coverage of the samples was assumed to be uniform, which allows us to use a scalar window function. Had the results of this analysis been highly significant, a more detailed treatment using the exact dataset would be justified. Secondly, the original shell and bulk velocity calculations involved some pre-grouping of galaxies in order to reduce noise, a process which we have ignored. The effect of this is, however, only significant nearby, since the

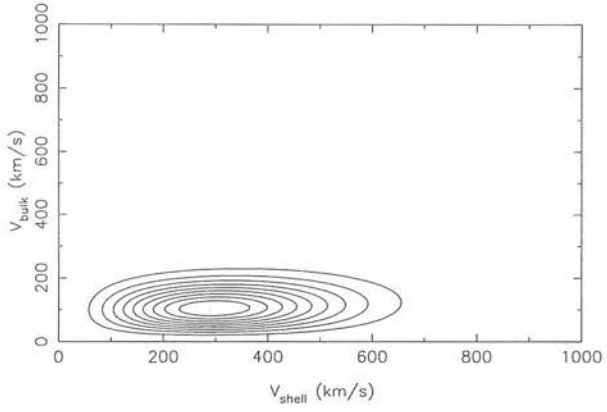

(a) $\beta = 0.1$

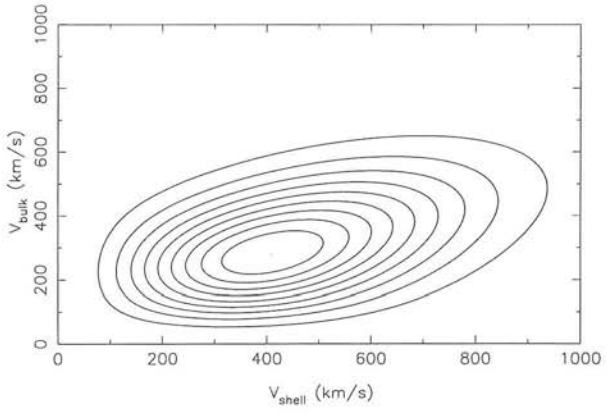

(b) $\beta = 1.0$

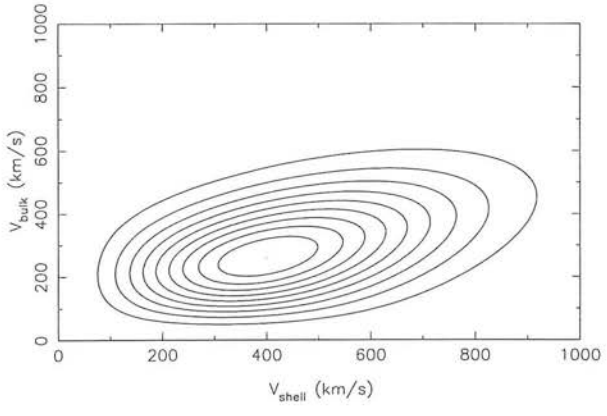

(c) $\Gamma = 0.2$, $\Omega_0 = 1.0$

Figure 2.7: Contour plot of the probability distribution $p(u_s, u_B)$ (equation (2.26)) of the bulk and shell velocities for the power spectrum of Peacock & Dodds (1994) with β= (a) 0.1, (b) 1.0. (c) shows a CDM-like model with $\Gamma = 0.2$, normalised to COBE with $\Omega_0 = 1$.

variance for a group of N galaxies (Lynden-Bell et al. 1988)

$$\sigma^2 = \sigma_z^2 + r^2[\exp(\Delta^2/N) - 1] \tag{2.30}$$

tends to $r^2\Delta^2/N$ at large r and the group behaves like N independent galaxies. We investigated the effect of the grouping by reducing the nearby selection function to that for groups. Taking the most pessimistic assumptions of largest group size and group variance equal to the galaxy variance, we find that the probabilities are virtually unchanged. We therefore do not think that the pre-grouping matters.

The joint distribution of the shell speed and the bulk speed is a more sensitive test of the amplitude than of the shape. Here we find that the high-amplitude model based on the IRAS galaxy power spectrum is acceptable provided that IRAS galaxies have $\beta \simeq 1$. Similarly the Γ=0.2 COBE-normalised flat models are not excluded for any value of Ω_0. As expected, if β for the IRAS sample drops below unity, it becomes very difficult to account for the high bulk speed observed.

Chapter 3

A Likelihood Analysis of The Redshift Distortion

Abstract

In this chapter the effect of redshift distortion on the galaxy distribution is examined in the formalism of spherical harmonics. According to the standard cosmological principle, distribution of galaxies in real space should be homogeneous and isotropic. Such assumption becomes invalid in the redshift space when the effect of inhomogeneity on the peculiar velocity is not negligible. This inhomogeneity can be exploited to measure β.

Using the spherical harmonic analysis with a first order correction for the redshift distortion (Heavens & Taylor 1995, hereafter HT), the density field is decomposed into radial and angular eigenfunctions of the Laplacian operator. Such a decomposition has the advantage that it complements well the redshift survey which is nearly spherically symmetric. The first order distortion in the redshift space with respect to the real space involves the cosmological density parameter, via $\beta \equiv \Omega_0^{0.6}/b$, where Ω_0 is the present density parameter and b is the bias parameter of the galaxy number and mass perturbations. The first order analysis also encompasses the power spectrum $P(k)$ whose

amplitude may be characterised by the fractional perturbations in a sphere of radius 8 h^{-1} Mpc, σ_8.

With the two parameters β and σ_8, a theoretical model of the expected perturbation can be constructed. This model was then compared with the data obtained from the IRAS 1.2 Jy survey to obtain β and σ_8 by a maximum likelihood analysis. Here a radially continuous spherical transformation was realised by setting a boundary at large distance. The advantage of using a continuous transformation as opposed to a discrete one is that we do not need to specify the boundary conditions. The likelihood analysis presented in this chapter should in theory be able to constrain β and σ_8.

3.1 Introduction

According to Hubble's expansion law, the recession velocity $\mathbf{v}$ of a galaxy is related to its distance $\mathbf{r}$ via $\mathbf{v} = H_0\mathbf{r}$, where H_0 is the Hubble constant. So in principle, the distance of any galaxy from us can be determined if we can measure the recession velocity by its Doppler shift. However, the local inhomogeneity around a galaxy induces a gravitational perturbation which causes the galaxy to deviate from its Hubble flow. This is rather unfortunate as it means that the distribution of galaxies in a three dimensional real space cannot be obtained straightforwardly from the redshift data. To measure the true distance of a galaxy from us, one could employ the Infrared Tully-Fisher method for spiral galaxies (e.g. Aaronson et al. 1989) or the $D_n - \sigma$ laws for the ellipticals (e.g. Lynden-Bell et al. 1988). However, the distance data obtained from these methods are not very accurate (typical error is about 10-20% of the measured distance) and their error increases with larger distances making it difficult to map the large-scale distribution accurately.

This redshift distortion transforms the real space coordinate (r, θ, ϕ) to a redshift space coordinate (s, θ, ϕ):

$$(s, \theta, \phi) = (r, \theta, \phi) + (u, 0, 0), \tag{3.1}$$

where u is the radially projected galaxy peculiar velocity divided by the Hubble con-

stant. Taking this distortion into account and using the first order Taylor expansion, the fractional overdensity is dependent on the ratio of the linear growth $f(\Omega_0) \simeq \Omega_0^{0.6}$ and the galaxy bias parameter b in the form of the parameter $\beta \equiv \Omega_0^{0.6}/b$. So in principle β can be constrained by comparing the model with the perturbation data obtained from any survey, the IRAS 1.2 Jy catalogue in this case. As the distortion u is dependent on both $f(\Omega_0)$ and the mass perturbation in $\mathbf{k}$ (wavenumber) space, $\delta(\mathbf{k})$ (Peebles 1980), it is inherent that the likelihood analysis will also constrain the power spectrum of mass fluctuations.

There are other methods in which β can be estimated from a galaxy survey. For example, in the linear perturbation theory, the velocity field is linearly related to the density field obtained from the survey; the constant of linearity is the parameter β itself (e.g. chapter 4; Strauss & Willick 1995). So in theory plotting the velocity field data (obtained from the POTENT method of e.g. Dekel et al. 1990) against the density field from the galaxy survey should yield a slope which constraints the value of β. However this method relies on the actual measurements of the true distance and thus becomes unreliable at large distance. The problem lies in the smoothing required to obtain the velocity field: The effective volume of the smoothing required to reduce the errors increases with distance and this limits the number of independent volumes in which reliable velocity data can be extracted.

Another way in which β can be estimated is by resolving the velocity and density potentials into their spherical harmonic components l, m. By taking into account the redshift distortion, one arrives at a differential equation for each l, m velocity potential which is β dependent (chapter 5). By integrating this differential equation for different l, m and then reconstructing the potential, one obtains a velocity field which can then be compared to the velocity field from POTENT. The main problem with this method is that for multipoles of the potential higher than that of the dipole (i.e. $l > 1$), the differential equation requires a boundary condition at infinity and the present galaxy survey may not provide enough buffer for the integration to be carried out reliably up to a large distance.

In the analysis of chapter 4 and 5, β is essentially determined dynamically and locally:

the velocity and density fields are compared point by point in real space using dynamic equations. The analysis presented here differs from the dynamic approach in that the parameters are constrained using the statistical properties of the redshift distortion and density field. It exploits the isotropy of the galaxy distribution in real space, and uses the observed anisotropy in redshift space to constrain β and the power spectrum $P(k)$ which in this case is assumed to have σ_8 as the only free parameter.

Given the nature of the redshift survey, an analysis using spherical coordinates becomes a logical and an attractive one as the problems associated in the radial (i.e. luminosity selection effect and redshift distortion) and the angular (incomplete sky coverage in (θ, ϕ)) direction can be dealt with independently. Expansion of the redshift-space density in the spherical coordinate has been considered in e.g. HT; Ballinger et al. (1995); Fisher et al. (1994a); Lahav (1993); Scharf et al. (1992) and Scharf & Lahav (1993).

Essentially, the analysis in this chapter is similar to the Spherical Bessel method used in HT with one crucial difference: we have set the boundary of our survey at large r so that the radial spherical transform is approximately continuous. In the analysis of HT, the boundary condition at a fixed survey radius meant that the wavenumbers k ($k = |\mathbf{k}|$) allowed to be analysed were preset by the spherical Bessel coefficients l, n. A continuous transform has the advantage that one can choose whatever k mode to be analysed rather than those that satisfy some boundary conditions at a fixed r. Moreover, as the boundary conditions might not be satisfied in the real universe, this method should in principle be superior. The mathematical development here follows closely to that of HT, the differences being the boundary at infinite radius and the consequent continuous range of wavenumbers considered. The orthogonality relation of (3.23) is derived here.

In section 3.2, the method of spherical Bessel harmonic is introduced. It shows how the redshift distortion and luminosity selection affect the expected perturbation. The method of data extraction from the IRAS survey is also outlined. The statistical approach in analysing the perturbation data is then done in section 3.3 and the results of the likelihood analysis are presented in section 3.4. It shows how the statistics are dependent upon the wavenumber and spherical Bessel coefficients analysed. Finally, the merits and shortfalls of this analysis are discussed in section 3.5.

3.2 Method

3.2.1 Introduction

In this section the notation and main equations of spherical harmonics are introduced. By analysing the scalar quantity in the context of spherical Bessel functions and harmonics, one is able to derive equations which relate the transform of the density field in redshift space to the underlying density perturbation. In other words a theoretical expression for the real space perturbation can be obtained with the appropriate weighting and selection functions of the galaxies. The procedures in which the perturbation data were obtained from the galaxy survey are also outlined. With both the theoretical and the measured perturbation available, it is then feasible to compare the two in the likelihood analysis to constrain the relevant parameters.

3.2.2 Spherical Bessel Harmonics

Any scalar quantity $G(\mathbf{r})$ can be decomposed as a linear combination of orthonormal eigenfunctions of an operator. The familiar one is the density fluctuation $\delta(\mathbf{r})$ decomposition in the Fourier modes. The Fourier modes are eigenfunctions of the Laplace operator ∇^2, written in cartesian coordinates. Our approach is to expand in eigenfunctions of ∇^2 now written in spherical coordinates. These eigenfunctions are products of spherical Bessel functions and spherical harmonics. Thus:

$$G(\mathbf{r}) = \sqrt{\frac{2}{\pi}} \sum_{lm} \int G_{lm}(k) j_l(kr) Y_{lm}(\theta, \phi) k^2 \mathrm{d}k \tag{3.2}$$

$$G_{lm}(k) = \sqrt{\frac{2}{\pi}} \int G(\mathbf{r}) j_l(kr) Y^*_{lm}(\theta, \phi) \mathrm{d}^3\mathbf{r}, \tag{3.3}$$

where $k = |\mathbf{k}|$. The spherical Bessel functions $j_l(z)$ are related to the ordinary Bessel functions by $j_l(z) = \sqrt{\pi/(2z)} J_{l+\frac{1}{2}}(z)$, the factor $\sqrt{2/\pi}$ is the normalisation factor chosen to be symmetrical in the transform and its inverse (Appendix A), and $Y_{lm}(\theta, \phi)$ are the Spherical Harmonic functions

$$Y_{lm}(\theta,\phi) = \sqrt{\frac{2l+1}{4\pi}\frac{(l-|m|)!}{(l+|m|)!}}\ P_l^{|m|}(\cos\theta) \times\exp(im\phi)\times\begin{cases}(-1)^m & m\geq 0\\ 1 & m<0\end{cases} \tag{3.4}$$

3.2.3 Redshift Distortion

The *observed* density at certain redshift $\mathbf{s}$ is different from the true *real* space density due to the luminosity selection effect that is inherent in any galaxy survey, plus the fact that the peculiar motions distort $\mathbf{r}$ to $\mathbf{s}$ (equation (3.1)). The observed density in redshift space $\rho(\mathbf{s})$ is related to the background mean density $\rho_0(\mathbf{r})$ by

$$\rho(\mathbf{s}) = \rho_0(\mathbf{r})[1+\delta(\mathbf{s})]. \tag{3.5}$$

It is important to note that $\rho_0(\mathbf{r})$ is the background mean density that also takes into account the selection effect and thus it is also spatially varying.

In order to use the likelihood analysis to constrain any parameter at all, one has to construct a theoretical model that is parameter-dependent which can be compared with the survey data. As one shall see later, the quantity $\rho_{lm}(k) - (\rho_0)_{lm}(k)$ defined by

$$\rho_{lm}(k) \equiv \sqrt{\frac{2}{\pi}}\int \rho(\mathbf{s})w(s)j_l(ks)Y^*_{lm}(\theta,\phi)\mathrm{d}^3\mathbf{s} \tag{3.6}$$

$$(\rho_0)_{lm}(k) \equiv \sqrt{\frac{2}{\pi}}\int \rho_0(\mathbf{r})w(r)j_l(kr)Y^*_{lm}(\theta,\phi)\mathrm{d}^3\mathbf{r} \tag{3.7}$$

is just one such case. The arbitrary weighting functions $w(r)$ and $w(s)$ are introduced here which one can set at freewill. For this analysis, these weighting functions were chosen so that a minimum variance in the power estimate can be achieved (section 3.2.5).

3.2.4 Fluctuations in the Redshift Space

In order to analyse the quantity

$$D_{lm}(k) \equiv \rho_{lm}(k) - (\rho_0)_{lm}(k) \tag{3.8}$$

mentioned in the last section, one has to carry out the integral of $\rho_{lm}(k)$ in redshift and $(\rho_0)_{lm}(k)$ in real space. Using the expansion of $j_l(ks)w(s)$ to first order:

$$j_l(ks)w(s) \simeq j_l(kr)w(r) + (s-r)\frac{\mathrm{d}}{\mathrm{d}r}[j_l(kr)w(r)], \tag{3.9}$$

together with equation (3.5), and the continuity $\rho(\mathbf{s})\mathrm{d}^3\mathbf{s} = \rho(\mathbf{r})\mathrm{d}^3\mathbf{r}$, $D_{lm}(k)$ is then

$$\begin{aligned} D_{lm}(k) &= \sqrt{\frac{2}{\pi}}\int \rho_0(\mathbf{r}) j_l(kr) w(r) \delta(\mathbf{r}) Y^*_{lm}(\theta,\phi)\mathrm{d}^3\mathbf{r} \\ &\quad + \sqrt{\frac{2}{\pi}}\int \rho_0(\mathbf{r})(s-r)\frac{\mathrm{d}}{\mathrm{d}r}[j_l(kr)w(r)]Y^*_{lm}(\theta,\phi)\mathrm{d}^3\mathbf{r}. \end{aligned} \tag{3.10}$$

Expanding $\delta(\mathbf{r})$ in terms of $\delta_{lm}(k)$ as in equation (3.2) and $u \equiv s - r$ as (Appendix B):

$$u = \beta\sqrt{\frac{2}{\pi}}\sum_{lm}\int \delta_{lm}(k)\frac{\mathrm{d}}{\mathrm{d}r}j_l(kr)Y_{lm}(\theta,\phi)\mathrm{d}k, \tag{3.11}$$

the expression for $D_{lm}(k)$ is now

$$D_{lm}(k) = \sum_{l'm'}\int \left[\Phi^{mm'}_{ll'}(k,k') + \beta V^{mm'}_{ll'}(k,k')\right]\delta_{l'm'}(k')k'^2\mathrm{d}k, \tag{3.12}$$

where

$$\begin{aligned} \Phi^{mm'}_{ll'}(k,k') &\equiv \frac{2}{\pi}\int \rho_0(\mathbf{r})w(r) \\ &\quad \times j_l(kr)j_{l'}(k'r)Y^*_{lm}(\theta,\phi)Y_{l'm'}(\theta,\phi)\mathrm{d}^3\mathbf{r} \end{aligned} \tag{3.13}$$

$$\begin{aligned} V^{mm'}_{ll'}(k,k') &\equiv \frac{2}{\pi k'^2}\int \rho_0(\mathbf{r})\frac{\mathrm{d}}{\mathrm{d}r}[w(r)j_l(kr)] \\ &\quad \times \frac{\mathrm{d}}{\mathrm{d}r}j_{l'}(k'r)Y^*_{lm}(\theta,\phi)Y_{l'm'}(\theta,\phi)\mathrm{d}^3\mathbf{r}. \end{aligned} \tag{3.14}$$

The first term in equation (3.12) represents the convolution in transform space arising from the multiplicative selection function in real space. The second term represents the redshift distortion. We have now constructed a theoretical model of the expected observable by virtue of equation (3.12). For a fixed boundary survey of size $r_{\max}$, it is necessary to specify the boundary conditions and as such the values of k allowed

to be analysed are preset by the Bessel coefficients l, n. In Binney & Quinn (1991), $j_l(k_{ln}r_{\max}) = 0$ whereas in HT, $\frac{\mathrm{d}}{\mathrm{d}r}j_l(k_{ln}r) = 0$ at $r = r_{\max}$. There are also different boundary conditions assumed by Taylor & Rowan-Robinson (1993) where the potential is set to zero and Lahav (1993) and Fisher et al. (1995b) who assumed a continuous derivative of the potential at the boundary. All these boundary conditions have the effect of turning the continuous transform into a discrete one and in so doing exclude the k values which do not satisfy the boundary condition. One advantage of using the continuous transform in k space of equation (3.2) is that it allows us to choose any k values to be analysed and there is no need to postulate any boundary condition.

For a survey where $\rho_0(\mathbf{r}) = \rho_0(|\mathbf{r}|)$, the $\Phi_{ll'}^{mm'}(k,k')$ and $V_{ll'}^{mm'}(k,k')$ can both be separated into the radial and angular matrix

$$\begin{aligned}\Phi_{ll'}^{mm'}(k,k') &= \Phi_{ll'}(k,k')W_{ll'}^{mm'} \\ V_{ll'}^{mm'}(k,k') &= V_{ll'}(k,k')W_{ll'}^{mm'},\end{aligned} \tag{3.15}$$

with

$$\begin{aligned}\Phi_{ll'}(k,k') &\equiv \frac{2}{\pi}\int \rho_0(r)w(r)j_l(kr)j_{l'}(k'r)r^2\mathrm{d}r \\ V_{ll'}(k,k') &\equiv \frac{2}{\pi k'^2}\int \rho_0(r)\frac{\mathrm{d}}{\mathrm{d}r}[w(r)j_l(kr)] \\ &\quad \times\frac{\mathrm{d}}{\mathrm{d}r}j_{l'}(k'r)r^2\mathrm{d}r \\ W_{ll'}^{mm'} &\equiv \int_\Omega Y_{l'm'}M(\Omega)Y_{lm}^*\mathrm{d}\Omega, \qquad \Omega \equiv (\theta,\phi),\end{aligned} \tag{3.16}$$

where $W_{ll'}^{mm'}$ is the masking matrix which takes into account the incomplete sky coverage of the IRAS survey by setting $M(\Omega) = 0$ in the excluded region and 1 in the observed parts of the sky. In the case of the IRAS survey, the region around the galactic plane and two narrow strips nearly perpendicular to the galactic plane are excluded due to source confusion and unsurveyed regions. If $M(\Omega)$ is continuous from ϕ=0 to 2π along a fixed galactic latitude, then $W_{ll'}^{mm'}$ matrix will be real. With the two exclusion strips, one can still approximate $W_{ll'}^{mm'}$ to be real given that the two strips are quite narrow.

The separation of $\Phi_{ll'}(k,k')$ and $V_{ll'}(k,k')$ into radial and angular parts in equation (3.15) shows the advantage of using spherical coordinates for the transform. For a

transformation using the Fourier expansion (e.g. Cole et al. 1994; Fisher et al. 1994b, Hatton & Cole 1997; Zaroubi & Hoffman 1996), no such simplification is possible.

3.2.5 Obtaining Data from Survey

To obtain $\rho_{lm}(k)$ of equation (3.6), one can in theory do so if the $\rho(\mathbf{s})$ observed is smooth and continuous in s space. Given that the IRAS survey is a discrete collection of galaxies in s space, the integral now approximates a discrete sum:

$$\rho_{lm}(k) \equiv \sqrt{\frac{2}{\pi}} \sum_{n=1}^{N} w(s_n) j_l(k s_n) Y_{lm}^*(\theta_n, \phi_n), \tag{3.17}$$

where n is the label for each galaxy and N is the total number of galaxies in the survey. For $(\rho_0)_{lm}(k)$ of equation (3.7), we use the analytic selection function of

$$\rho_0(r) = a r^{-2\alpha} \left[1 + \left(\frac{r}{r_*} \right)^2 \right]^{-\beta_*}, \tag{3.18}$$

where a=0.189, α=0.421, r_*=50.1h^{-1}Mpc, and β_*=1.913 (HT and references therein). For the weighting function, the optimal weighting scheme adopted by HT which minimises the variance of the σ_8 estimate was chosen:

$$w(r) \approx \frac{1}{1 + P(k)\rho_0(r)}, \tag{3.19}$$

where $P(k)$ is the power spectrum of the galaxies. As the weighting function allows $P(k)$ to be a function of k, it should improve the results obtained in HT where a single value of $P(k)$ was used for all modes analysed. To ensure that the boundary of the integrals of $(\rho_0)_{lm}(k)$ and indeed of $\Phi_{ll'}(k,k')$ and $V_{ll'}(k,k')$ of equation (3.16) was effectively at infinity, the integrals were tested with an upper r limit of $r_{\max}$=5000 and 10000 h^{-1} Mpc. The results were virtually identical in both cases.

3.3 Likelihood Analysis

3.3.1 The Covariance Matrix for $D_{lm}(k)$

The purpose of the likelihood analysis here is to evaluate the probability distribution of β and σ_8 with the given data $D_{lm}(k)$. From Bayes theorem, this probability (denoted by $p(\beta, \sigma_8|D_{lm}(k))$ here) is related to the probability of the simultaneous occurrence of β, σ_8 and the data $D_{lm}(k)$ (denoted by $p(\beta, \sigma_8, D_{lm}(k))$) and the probability of the occurrence of the data $p(D_{lm}(k))$ by

$$\begin{aligned} p(\beta, \sigma_8|D_{lm}(k)) &= \frac{p(\beta, \sigma_8, D_{lm}(k))}{p(D_{lm}(k))} \\ &= \frac{p(D_{lm}(k)|\beta, \sigma_8)p(\beta, \sigma_8)}{p(D_{lm}(k))}, \end{aligned} \tag{3.20}$$

where $p(D_{lm}(k)|\beta, \sigma_8)$ is the probability of the occurrence of the data $D_{lm}(k)$ with a given value of β and σ_8. With the prior assumption that the probability $p(\beta, \sigma_8)$ is uniformly distributed, we can thus deduce that $p(\beta, \sigma_8|D_{lm}(k))$ is proportional to $p(D_{lm}(k)|\beta, \sigma_8)$. For a Gaussian field, the probability of the occurrence of a data set $D_{lm}(k), D_{l'm'}(k')$ with some given values of β and σ_8 is

$$p(D_{lm}(k), D_{l'm'}(k')|\beta, \sigma_8) = \frac{1}{(2\pi)^{N/2}(\det \mathbf{C})^{1/2}} \exp -\frac{1}{2} \sum D_{lm}(k) \mathbf{C}^{-1}_{lmkl'm'k'} D_{l'm'}(k'), \tag{3.21}$$

where $\mathbf{C}_{lmkl'm'k'} = \langle D_{lm}(k) D_{l'm'}(k') \rangle$ and N is the number of coefficients of $D_{lm}(k)$. So for comparison between the model and the observation in the likelihood analysis, it is necessary to construct the statistical averages:

$$\begin{aligned} \langle D_{lm}(k) D^*_{l'm'}(k') \rangle &= \sum_{\bar{l}\bar{m}} \int \left[\Phi^{m\bar{m}}_{l\bar{l}}(k, \bar{k}) + \beta V^{m\bar{m}}_{l\bar{l}}(k, \bar{k}) \right] \\ &\quad \times \left[\Phi^{m'\bar{m}}_{l'\bar{l}}(k', \bar{k}) + \beta V^{m'\bar{m}}_{l'\bar{l}}(k', \bar{k}) \right]^* P(\bar{k}) \bar{k}^2 \mathrm{d}\bar{k} \end{aligned} \tag{3.22}$$

where one has used (Appendix C; cf. the Kronecker delta function that appears in the discrete transform of HT)

$$\langle \delta_{lm}(k) \delta^*_{l'm'}(k') \rangle = \frac{\delta^{\mathrm{D}}(k - k')}{k^2} P(k) \delta^{\mathrm{K}}_{ll'} \delta^{\mathrm{K}}_{mm'}, \tag{3.23}$$

where $\delta^{\rm D}(k-k')$ is the Dirac delta function in $k-k'$, and $\delta^{\rm K}_{ll'}$ is a Kronecker delta function. In practice, the coefficients in equation (3.22) can be split into real-real and imaginary-imaginary parts. Given that the actual galaxy survey is a collection of discrete positions, a shot noise term has to be added to $\langle D_{lm}(k)D^*_{l'm'}(k')\rangle$ in the model. The full covariance matrix is thus

$$\begin{aligned}\langle D_\mu D_\nu\rangle &= \frac{1}{2}\sum_{\alpha\bar{k}}\int(\Phi_\mu^{\alpha\bar{k}}+\beta V_\mu^{\alpha\bar{k}})(\Phi_\nu^{\alpha\bar{k}}+\beta V_\nu^{\alpha\bar{k}})P(\bar{k})\bar{k}^2{\rm d}\bar{k} \\ &\quad +\Lambda^0_{\mu\nu} \end{aligned} \tag{3.24}$$

where the compact notation $D_\mu \equiv D_{lm}(k)$ and so on is used here. The factor of $1/2$ is present in the signal term to take into account that one is actually modelling the real-real and the imaginary-imaginary coefficients. The $\Lambda^0_{\mu\nu}$ is the discrete shot noise term (appendix D):

$$\begin{aligned}\Lambda^0_{\mu\nu} &= \frac{2}{\pi}\int\rho_0(r)w^2(r)j_l(kr)j_{l'}(k'r)r^2{\rm d}r \\ &\quad \times\int\mathcal{P}_\mu[Y_{lm}(\Omega)]M(\Omega)\mathcal{P}_\nu[Y^*_{l'm'}(\Omega)]{\rm d}\Omega,\end{aligned} \tag{3.25}$$

where $\mathcal{P}_{\mu,\nu}$ represents real or imaginary parts, depending on whether $D_{\mu,\nu}$ is real or imaginary. To obtain an accurate value of $\langle D_\mu D_\nu\rangle$, one would do an infinite sum and integral in α and k_α of equation (3.24) for any given μ and ν, which is of course impractical. Instead a sum of $\bar{l}$ from 0 to 30 was used and the infinite integral in k_α was replaced by a discrete sum from 0.01 to 0.2 h Mpc^{-1} with a spacing of 0.01 h Mpc^{-1}. Such approximation is justified by the fact that the biggest contributions to $\langle D_\mu D_\nu\rangle$ come from $\Phi_{l\bar{l}}(k,\bar{k})$ and $V_{l\bar{l}}(k,\bar{k})$ with $\bar{l}\simeq l$ and $\bar{k}\simeq k$. Modes with $l>16$ and $k>0.1$ h Mpc^{-1} were not analysed. The dominance of $\bar{l}\simeq l$ and $\bar{k}\simeq k$ term is apparent when the mixing matrices $\Phi_{ll'}(k,k')$ and $V_{ll'}(k,k')$ are plotted, as shown in figure 3.1.

For the power spectrum, the parametrised form of Peacock & Dodds (1994) was used:

$$P(k)=\frac{2\pi^2A(k/k_0)^{1.5}}{k^3\left[1+(k/k_c)^{-2.5}\right]} \tag{3.26}$$

where k_0=0.29 h Mpc^{-1} is the non linear scale, k_c=0.039 h Mpc^{-1} is the break scale, and A is a free parameter which is related to the fractional fluctuations in the real space

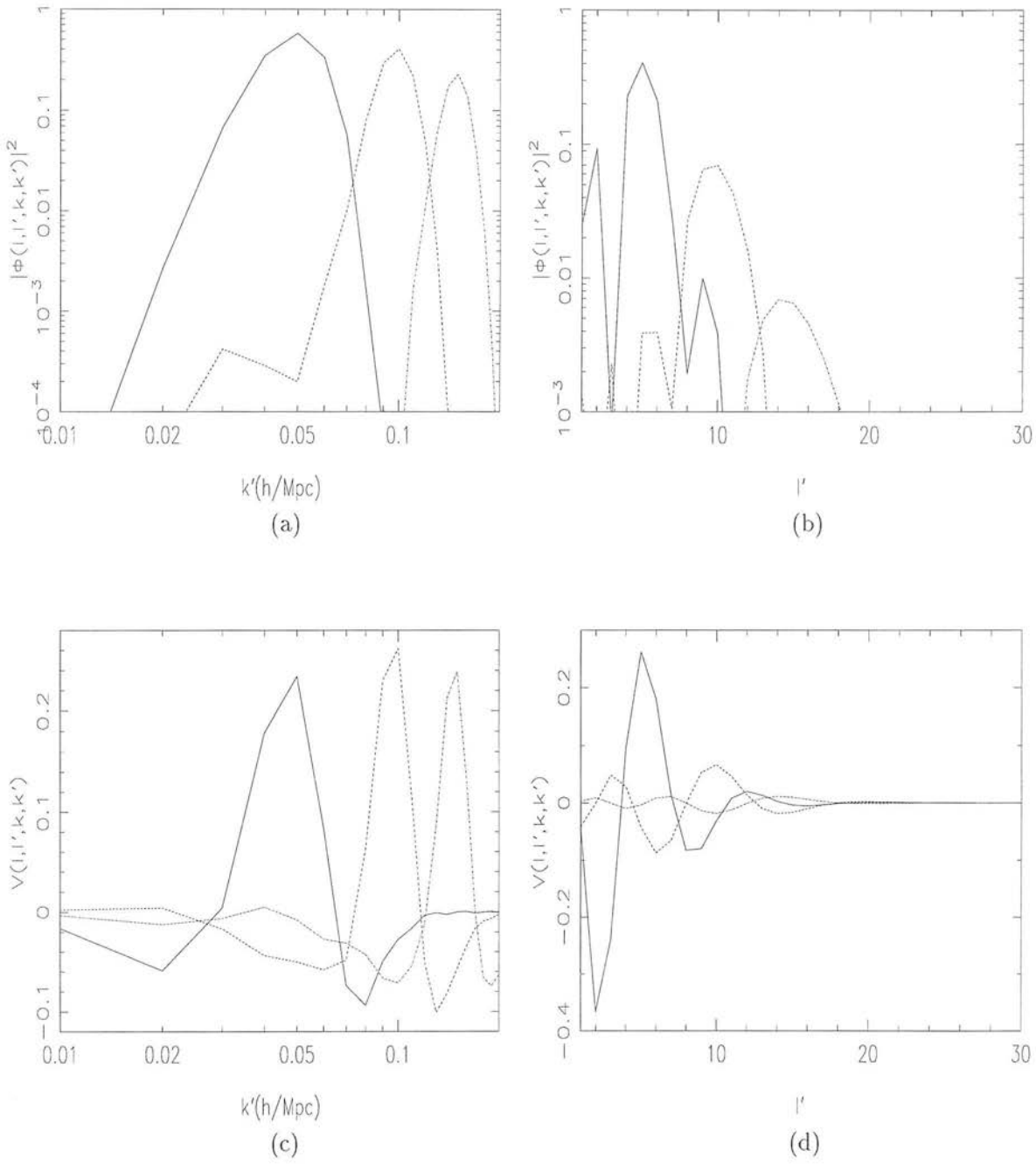

Figure 3.1: Mixing matrixes $\Phi_{ll'}(k,k')$ and $V_{ll'}(k,k')$ due to luminosity selection in the first case and redshift distortion in the second. The plot of $|\Phi_{ll'}(k,k')|^2$ and $V_{ll'}(k,k')$ against k' [(a) and (c)] has coefficients $l = l' = 5$ and $k = 0.05$ (solid), 0.1 (dashed), and 0.15 (dot-dashed) h Mpc^{-1}. For the plot against l' [(b) and (d)], $k = k' = 0.05$ h Mpc^{-1} and l=5 (solid), 10 (dashed), and 15 (dot-dashed). Minimum variance weighting adopted by HT was used.

number density in an 8 h^{-1} Mpc sphere via $\sigma_{8,\mathrm{IRAS}} = 0.69\sqrt{A}$. We take this to be a free parameter.

So effectively the theoretical model of $\langle D_\mu D_\nu \rangle$ has two free parameters: β and σ_8. The main idea in the likelihood analysis is to compare the model to the IRAS survey data in order to constraint these two parameters.

3.3.2 Likelihood Analysis of the Observables

In the theory of structure formation in cosmology, it is often assumed that the initial density perturbations required to seed the structure are Gaussian. In other words the probability distributions of the real and imaginary parts of $\delta_{lm}(k)$ are Gaussian and independent of each other. Such a condition arises from the assumption that the natural condition in the early formation of $\delta_{lm}(k)$ has random phases. There is no direct evidence to prove this assumption but if one is to assume otherwise, then one has to postulate a non-random phase theory which on the face of it, seems unnatural and difficult to justify. There is also observational evidence which is consistent with fluctuations being Gaussian on linear scales (Stirling & Peacock 1996; Kogut et al. 1996)

Assuming that the real and imaginary parts of $\delta_{lm}(k)$ are independent of each other, the likelihood of a configuration δ is then the product of the two:

$$\mathcal{L}[\delta] = P[\mathcal{R}e(\delta_{lm}(k))]P[\mathcal{I}m(\delta_{lm}(k))]. \tag{3.27}$$

With Gaussian distribution for each component, the likelihood becomes (HT; Scharf & Lahav 1993; Fisher et al. 1994a)

$$\begin{aligned}\mathcal{L}[\beta, P(k)] \;=\; & (\det \mathbf{C}_{\mathcal{R}e})^{-1/2} (\det \mathbf{C}_{\mathcal{I}m})^{-1/2} \\ & \times \exp\left[-\frac{1}{2}\sum_{\mu\nu} \mathcal{R}e(D_\mu)(\mathbf{C}_{\mu\nu\mathcal{R}e})^{-1}\mathcal{R}e(D_\nu)\right] \\ & \times \exp\left[-\frac{1}{2}\sum_{\mu\nu} \mathcal{I}m(D_\mu)(\mathbf{C}_{\mu\nu\mathcal{I}m})^{-1}\mathcal{I}m(D_\nu)\right],\end{aligned} \tag{3.28}$$

where $\mathbf{C}_{\mu\nu}$ is the real-real or imaginary-imaginary matrix of $\langle D_\mu D_\nu \rangle$, and $\mathcal{R}e(D_{\mu,\nu})$,

$\mathcal{I}m(D_{\mu,\nu})$ are the real and imaginary component of the $D_{\mu,\nu}$ data obtained from the survey.

It is interesting to note that here the covariance matrix $\mathbf{C}_{\mu\nu}$ for $\mu \neq \nu$ is non zero; in other words there is a coupling relationship between D_μ and D_ν of different modes. Such correlation arises as a consequence of the spatial variation in the selection and weighting functions plus the existence of redshift distortion. The masking of the sky also mixes modes with different l and m. The redshift distortion renders the $V^\alpha_{\mu,\nu}$ of equation (3.24) to be non-zero (see equation (3.10)) and the variation of $\rho_0(r)$ and $w(r)$ mixes different modes in $\Phi^\alpha_{\mu,\nu}$, $V^\alpha_{\mu,\nu}$ and $\Lambda^0_{\mu\nu}$ and as a result these matrixes all have a finite width shown in figure 3.1. If the galaxy survey does not suffer the selection and masking problems (i.e. $\rho_0(r)$=constant, $M(\Omega)$=1) and one can set the weighting function $w(r)$ to be spatially non-varying, these matrixes would then behave as a spike function and no mixing of different modes would have occurred.

Fortunately the widths of the mixing matrixes are not too big that those modes that are far apart will give a significant contribution to the covariance matrix.

3.4 Application to the IRAS Data

3.4.1 Choice of Modes

It would be unwise and inefficient to just blindly apply the likelihood equation of (3.28) to the IRAS data for all the modes. One needs to consider modes to be excluded either because of the nature of the IRAS survey itself, or that modes that do not yield much information will be inefficient to analyse. Firstly the $l = 0$ mode was excluded as it is radial, and may be partially eliminated by the procedure to estimate the selection function. Secondly as the IRAS data can be analysed in e.g. the Local Group or Cosmic Microwave Background frame, the $l = 1$ dipole mode was excluded so that the likelihood analysis does not become frame dependent. For the $m = 0$ mode, $D_{\mu,\nu}$ becomes real and one needs to modify the likelihood analysis for this special case. For convenience $m = 0$ mode was not included in this analysis.

Despite the exclusion of the $l = 0, 1$ and $m = 0$ modes, it is still very inefficient to include all other modes for analysis. At a given wavenumber k, analysing l beyond certain value does not yield much more information on the likelihood but the inclusion of these modes increases the size of the covariance matrix and greatly reduces the speed of calculation. For any given k, the first maximum of the spherical Bessel function $j_l(kr)$ occurs at a greater r the bigger the l. At r below the first maximum, $j_l(kr)$ is close to zero and galaxies are effectively excluded within this range by virtue of equations (3.6) and (3.7). If l is chosen to be so large that the first maximum occurs at r that is bigger than the reliable survey radius, analysis of these modes will be noisy and inefficient. For large l, the first maximum occurs at $kr \sim (l + 1/2)$ (e.g. Abramowitz & Stegun 1970). If one chooses the maximum reliable survey to be at 200 h^{-1} Mpc, then the upper limit of l to be analysed for a given k is $l \sim 200k$. The selection of l presented here is in fact not very dissimilar to the discrete k imposed by the boundary condition in HT. In their analysis, the derivative of $j_l(kr)$ at the boundary is zero.

Due to the mixing property of the covariance matrix (see §3.3.2) for different modes, k beyond 0.1 h Mpc^{-1} were excluded so that the analysis was not contaminated by small scale (high k) nonlinear effect. The signal to noise ratio is generally higher at low l, but drops to a low value at high l.

It is important to realise that although not all the modes were included in the calculation, the analysis is by no means wrong or much more inferior. By excluding modes that are noisy and of negligible contribution, the likelihood calculation still achieved the result that is similar to that where if all modes were included, but at a faster speed. Figure 3.2 illustrates the difference between the likelihood contour at $k = 0.8h$ Mpc^{-1} for upper limit of l= 14 and 20. Whereas increasing l seems to have improved the contour slightly, such slight improvement has to be weighted against the great expense of speed.

3.4.2 Results

With β and σ_8 as the free parameters and the $\sim$ 5000 galaxies in the IRAS 1.2 Jy survey, the likelihood analysis was carried out with k running from 0.01 to 0.1 h Mpc^{-1} with an interval of 0.01 h Mpc^{-1}. The upper limits of l for each k were 2,3,4,6,8,11,13,14,15 and

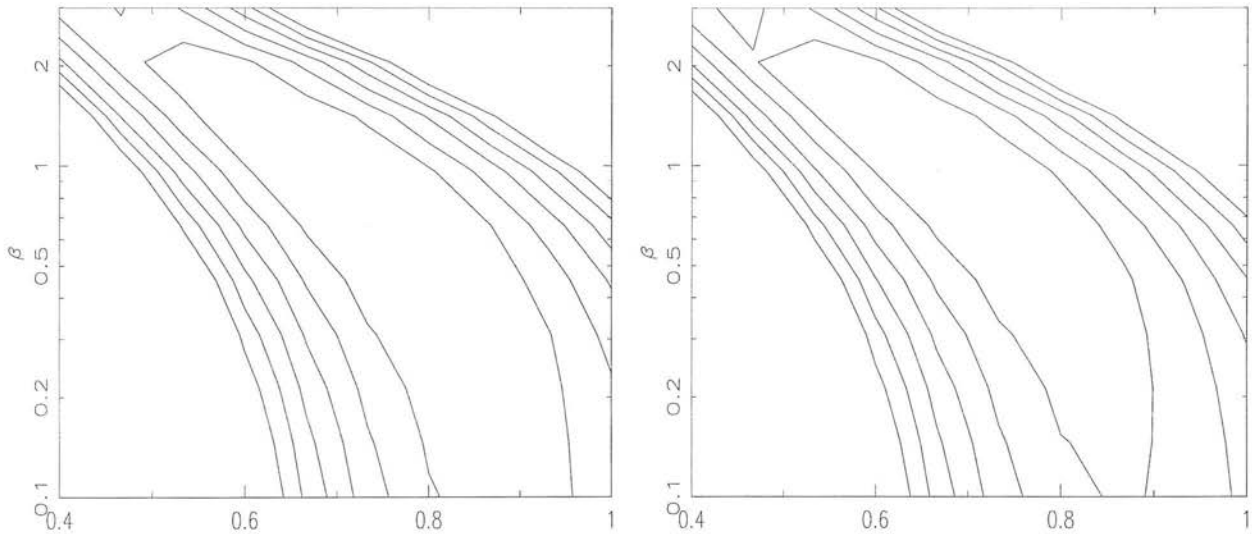

Figure 3.2: Likelihood contours for β and σ_8 of the IRAS 1.2 Jy sample. A parametric form of the power spectrum was assumed. A wavenumber of $k = 0.8h$ Mpc^{-1} was used and the upper limits of l were (a) 14 , and (b) 20. The contour spacing corresponds to $\delta \ln \mathcal{L} = 0.5$.

16 making it a total of 584 modes.

A k spacing of 0.01 h Mpc^{-1} was chosen as a compromise so that it is neither too wide nor too narrow. In an ideal world, one would choose the k spacing to be as narrow as possible. In practice however, modes that are close together in k are strongly correlated as figure 3.1 shows. As a consequence the covariance matrix $\langle D_\mu D_\nu \rangle$ becomes almost singular and this presents some numerical problems of inversion and calculating its determinant. The speed of a closely-spaced k analysis will also be greatly reduced due to the increase in the size of the matrix.

The likelihood contours in the β-σ_8 plane are shown in figure 3.3. The contour levels are separated by $\delta \ln \mathcal{L} = 0.5$. In addition to the analysis of up to $k = 0.1h$ Mpc^{-1}, likelihood contours for k up to values of 0.07, 0.08, and 0.09 h Mpc^{-1} are also presented. The maximum of the contour seems to be shifting towards the bottom right the higher the k used in the calculation, suggesting that perhaps small-scale fluctuations analysis favours low value of β and high value in σ_8. This may be understood as follows: the signature of redshift distortion on large, linear scales is the flattening along the line-of-sight of structures, due to the large-scale infall onto clusters. However, the presence of small-scale virialised regions give rise to the opposite effect: structures are elongated along the line-of-sight giving rise to the so-called "Fingers of God". The contribution of this effect, which was not included in the analysis, is thus to reduce the estimate of β, with a reduction which becomes more severe as one looks to higher k.

3.5 Discussion

Figure 3.3 shows clearly that the peak of the likelihood contour changes position as a function of the upper limit of k analysed. It is clearer to present the estimated values of β and σ_8 along with their error bars against the k limit. If the two parameters have normal distribution for different realisation of the universe, then projecting the ellipses horizontally (for β) and vertically (for σ_8) at one (this number is just an arbitrary choice here) contour level, which amounts to $\delta \ln \mathcal{L} = 0.5$, gives confidence level of $\approx 68\%$ for each parameter individually (chapter 15, Press et al. 1992) and is chosen to be the

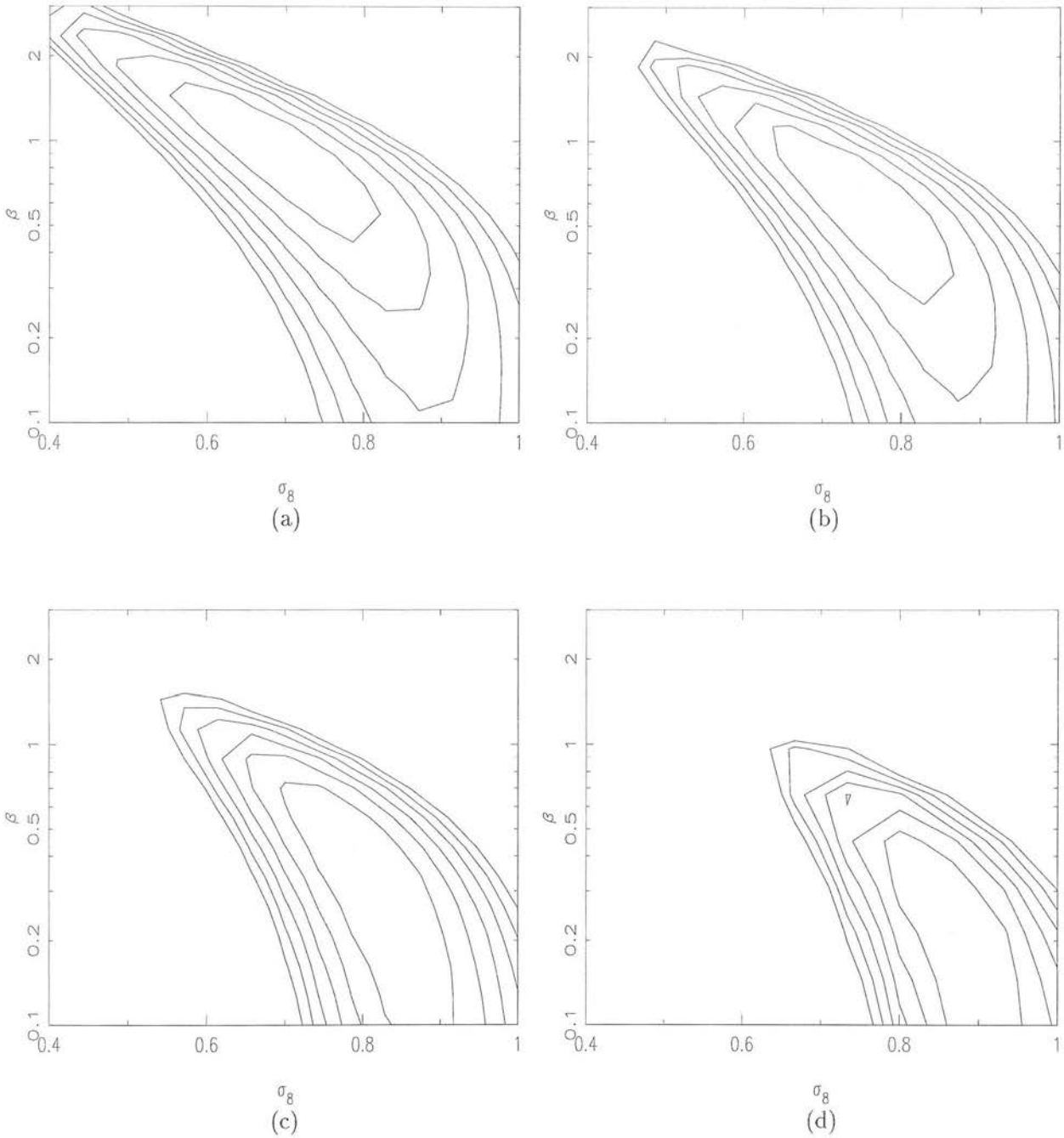

Figure 3.3: Likelihood contours for β and σ_8. A parametric form of the power spectrum in which the amplitude was allowed to vary and a minimum variance weighting scheme devised by HT were used. The contour levels are separated by $\delta \ln \mathcal{L} = 0.5$. The values of k analysed went from 0.01 up to (a) 0.07, (b) 0.08, (c) 0.09, and (d) 0.1 h Mpc^{-1} in step of 0.01 h Mpc^{-1}.

magnitude of error bars in figure 3.4.

The results here show that analysis with high k mode seems to have the effect of lowering the value of β while raising that of σ_8. In fact taking $\delta \ln \mathcal{L} = 0.5$ as the upper and lower limits, figure 3.4 indicates that analysis with k greater than about 0.1 h Mpc^{-1} gives β and σ_8 values that are marginally inconsistent with the low k analysis. This is most likely to be due to the small-scale velocity dispersion effect at high k which was not corrected for. Such high k contamination is more severe here than the analysis of HT because of the variable $P(k)$ used here (as opposed to $P(k)$ with a fixed value in HT). The result of using this variable $P(k)$ is that the mixing matrix is broader in k space than that in HT and so more high k modes will be mixed in. Cole et al. (1994) also suggested that the nonlinear effects can underestimate the true value of β.

Although the analysis presented here assumes a boundary at infinity, the fact that the selection function is not well known beyond about 200 h^{-1} Mpc forced us to choose it to be zero beyond that distance. This is far less than ideal but such assumption was necessary.

Here the presence of peculiar velocities was exploited to estimate β and σ_8. However this method does not rely on the actual measurements of peculiar velocities which can be prone to large errors. One can also limit the calculation inside the linear regime by choosing the k modes to be analysed. For a nearly all-sky galaxy catalogue, this method has the advantage that the mixing matrixes are not too wide and so mixing of different l, m, k modes is limited.

Although the continuous transform presented here sets the boundary effectively at infinity, the actual galaxy catalogue does not extend beyond a few hundred h^{-1} Mpc. At large distances where galaxies are sparse, the discrete shot noise overwhelms the signal itself. It is for this reason that the result here does not show an enormous improvement over that of HT, where the boundary was set at 200 h^{-1} Mpc. HT found a maximum likelihood of $\beta \simeq 1.1 \pm 0.3$ which is somewhat higher than the result here but still within bound of each other, and the value of β here is at least consistent with the 0.65 found by Hamilton (1993a) using the IRAS 2 Jy survey. However, it is clear from the results of figure 3.4 that we have been unable to unambiguously determine β, and that it is clearly

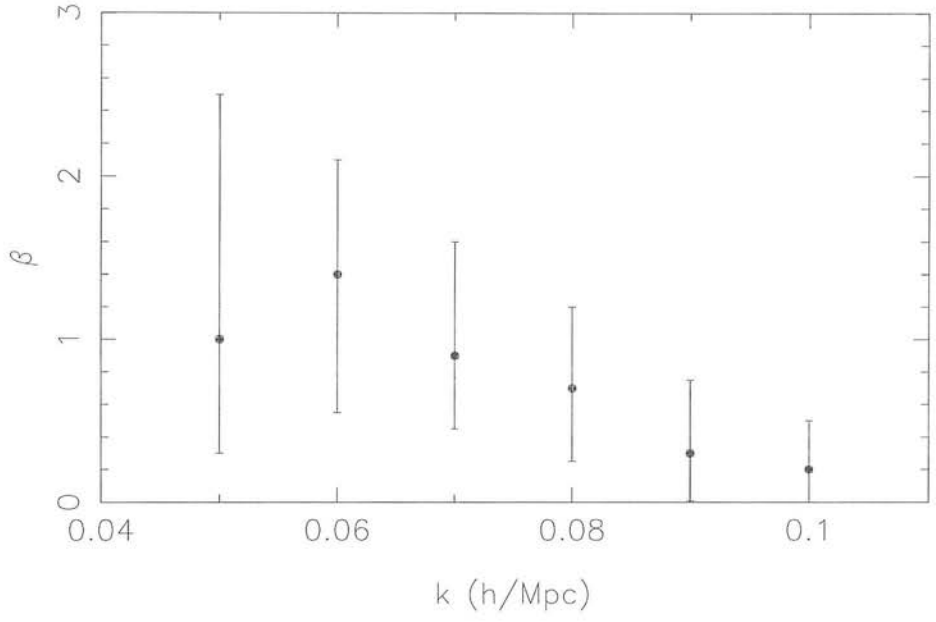

(a)

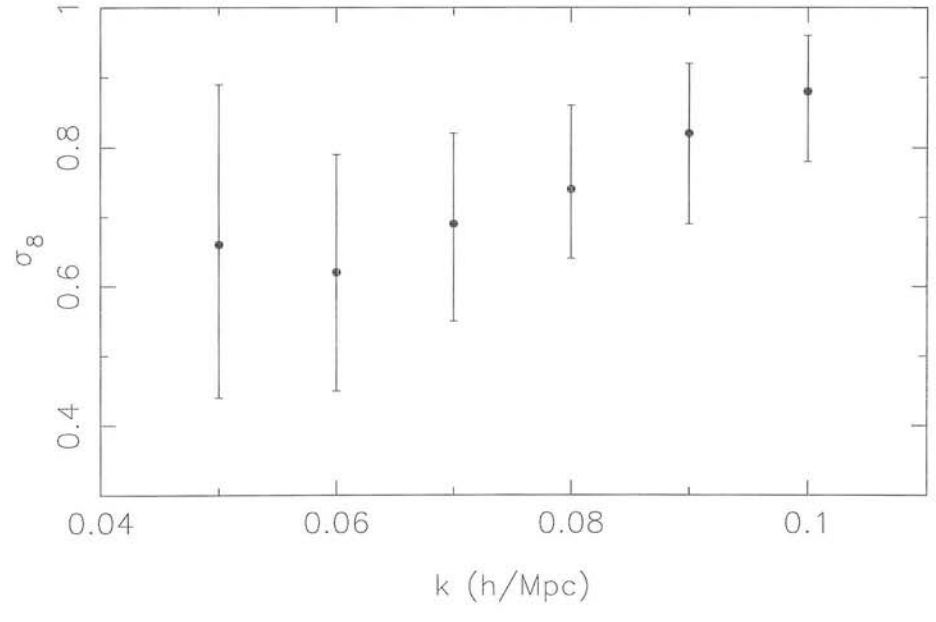

(b)

Figure 3.4: Estimated values of (a) β and (b) σ_8 for different upper limit of k analysed. The error bars lie within the horizontal and vertical projections of the likelihood contours that correspond to $\delta \ln \mathcal{L} = 0.5$.

necessary in future work to model the small-scale velocity dispersion. The qualitative effect if this will be to increase β at high k, and reduce σ_8, and one might hope to obtain stable results. Other notable values of β using maximum likelihood analysis are e.g. $0.96^{+0.20}_{-0.18}$ in Fisher et al. (1994a) and 1.04 ± 0.3 in Ballinger et al. (1995).

If desired, this method can also be adapted to allow the shape of the power spectrum to be free and this is currently being investigated by Ballinger, Heavens & Taylor. Because of the radial nature of the redshift distortion and selection function, and masking of the sky is specified in angular terms, analysis using the spherical coordinates here has the advantage over the plane-wave method of Kaiser (1987) in that selection, weighting and masking can be easily incorporated. As with many other methods of analysing any galaxy catalogue, the advantages of this method will hopefully be realised in future surveys which probe deep into space with lower shot noise than that of the IRAS 1.2 Jy survey.

The $\Phi_{ll'}(k,k')$, $V_{ll'}(k,k')$, and the $\Lambda^0_{\mu\nu}$ matrix were computed by myself. The $W^{mm'}_{ll'}$ matrix was obtained from Andy Taylor and all the $\rho_{lm}(k)$ data were generated by my own programme.

Chapter 4

Peculiar Velocity and Number Density of IRAS Galaxies

Abstract

In this chapter, I present a way in which the relationship between the peculiar velocity potential and density field derived from the IRAS 1.2 Jy galaxies can be used to probe some of the most important parameters in cosmology: namely the density parameter and the bias relationship between mass and light distribution. One can derive a simple relationship between the velocity and the density field via these parameters whose values can be estimated if one can somehow obtain an accurate distribution of galaxies and their velocities. The main goal of this chapter is to present a method in which the velocity potential from POTENT can be utilised directly with the IRAS catalogue to estimate $\beta \equiv \Omega^{0.6}/b$, where Ω and b are the density and bias parameter respectively.

4.1 Introduction

In chapter 2 and 3, β was estimated or constrained by means of statistical analysis in which a maximum likelihood method was employed. Such a statistical approach tackles the problem by comparing peculiar velocity and density fields globally (chapter 3). Here

however, a different way of estimating β is presented. It is essentially a dynamical approach in which the velocity potential is compared point by point (locally throughout part of the survey volume) with a predicted potential obtained from the IRAS 1.2 Jy survey. Unlike the method used in chapter 3, the analysis here does rely on the actual measurement of the peculiar velocity in order that such dynamical comparison can be made.

If gravity is responsible for the observed galactic motion, and if light does indeed reflect in some way the underlying mass, then the observed galaxy distribution should tell us something about how the large-scale motion of the galaxies will behave. The galaxy and peculiar velocity fields have previously been compared in various ways. For example, $\nabla^2\Phi$ and δ (where Φ and δ are the peculiar velocity potential and density perturbation respectively) are compared in the POTENT analysis of Dekel et al. 1990; and more recently in e.g. Dekel et al. (1993) which yielded $\beta = 1.28^{+0.75}_{-0.59}$ at 95% confidence; Hudson et al. (1995, $\beta_{\rm opt} = 0.74 \pm 0.13$); and Sigad et al. (1997, $\beta = 0.89 \pm 0.12$). The predicted and measured peculiar velocities $-\nabla\Phi$ are compared in e.g. Strauss (1989); Kaiser et al. (1991); Hudson (1994); Shaya et al. (1995); Willick et al. (1997) and Webster et al. (1997). In this study we make a direct comparison of Φ itself, with the potential predicted from the galaxy positions in the IRAS 1.2 Jy sample. However it is not a straightforward process of obtaining the peculiar number potential from the galaxy catalogue. This is because galaxy positions are given in redshift coordinates. Added to that we also have the problems of luminosity-selection bias and the incomplete sky coverage of the survey. The velocity potential data also suffer from the difficulty of measuring the peculiar velocity, especially at large distances. The difficulty in obtaining the velocity potential is further enhanced by the fact that one can only measure the radial velocity of any galaxy whereas in an ideal situation, one would use the full three dimensional velocity vector to deduce its potential.

Throughout the whole analysis, three important assumptions were made. The first being the existence of a simple linear relationship between the galaxy and mass perturbations as described in section 1.12. Secondly the large-scale peculiar motion of galaxies is irrotational (i.e. $\nabla \times \mathbf{v} = 0$). This hypothesis is discussed in more detail in section 1.13. Finally the fluid equations were analysed under linear condition where the mass

perturbation is assumed to be much less than unity. These assumptions allow us to derive a simple linear relationship between the two potentials mentioned above.

In section 4.2, the relationship between the velocity and density field is derived quantitatively using the Newtonian treatment of a fluid. This theoretical analysis gives a linear relationship between the two fields. The process of obtaining the density field from the IRAS 1.2 Jy survey is tackled in section 4.3. In particular, I concentrate on the methods of weighting and smoothing of the galaxy data. In section 4.4, the methods of the so-called POTENT which extracted the peculiar velocity field are briefly presented and the results of comparing the velocity and the density field are shown in section 4.5, where the pros and cons of this method and analysis are also discussed.

4.2 Newtonian Treatment of Linear Perturbation

In section 1.11 the fluid equations in cosmology were developed using the Newtonian treatment of linear perturbation. Under such treatment, one arrives at an equation governing the growth of the perturbation against time or scale factor. Our purpose here is to use the same Newtonian treatment to probe the relationship between the velocity field potential and the potential obtained from the distribution of galaxies. It turns out that these two potentials are simply linearly related to each other by the cosmological parameter β. The main problem with using this method to estimate β lies in the practicality of obtaining the accurate value of the potentials. Such problem will be addressed later in sections 4.3 and 4.4.

4.2.1 Velocity and Density Field

To obtain a relationship between the velocity and the density field, we proceed from the fluid equations derived in section 1.11.1. In the linear perturbation ($\delta \ll 1$) with zero pressure, equations (1.71) become

$$\frac{\partial \mathbf{v}}{\partial t} + \frac{\dot{a}}{a}\mathbf{v} = \mathbf{g} \quad , \quad \frac{\nabla.\mathbf{v}}{a} + \frac{\partial \delta}{\partial t} = 0, \tag{4.1}$$

where $\mathbf{g} = -\nabla\phi_{\rm grav}/a$ is the peculiar gravitational acceleration and can be shown to be (Peebles 1980, §7)

$$\mathbf{g}(\mathbf{x}) = G\bar{\rho}a \int \delta(\mathbf{x}', t)\, \frac{(\mathbf{x}' - \mathbf{x})}{|\mathbf{x}' - \mathbf{x}|^3}\, \mathrm{d}^3\mathbf{x}'. \tag{4.2}$$

The solution to the second equation of (4.1) is

$$\mathbf{v} = a\frac{\partial}{\partial t}\left(\frac{\mathbf{g}}{4\pi G\bar{\rho}a}\right). \tag{4.3}$$

The perturbation δ is a sum of two terms (see section 1.11.2), each of which varies as a solution $D_\alpha(t)$:

$$\delta(\mathbf{x}, t) = A(\mathbf{x})D_1(t) + B(\mathbf{x})D_2(t). \tag{4.4}$$

So by equation (4.2), we can say that $\mathbf{g}$ is the sum of two terms that vary as

$$\mathbf{g}_\alpha \propto \bar{\rho}aD_\alpha. \tag{4.5}$$

The velocity associated with each mode is, according to equation (4.3),

$$\mathbf{v}_\alpha = \frac{\mathbf{g}_\alpha}{4\pi G\rho_b}\, \frac{1}{D_\alpha}\, \frac{\mathrm{d}D_\alpha}{\mathrm{d}t}, \tag{4.6}$$

which can be written as

$$\mathbf{v} = \frac{2f\mathbf{g}}{3H\Omega} \quad , \quad f \equiv \frac{a}{D}\, \frac{\mathrm{d}D}{\mathrm{d}a}. \tag{4.7}$$

If the growing mode (where e.g. $D_1 \propto t^{2/3}$ for the Einstein de-Sitter model) dominates, then f can be approximately related to Ω (Peebles 1980, §14) as $f(\Omega) \simeq \Omega^{0.6}$.

In the linear perturbation approximation, only the irrotational component of the peculiar velocity grows as a result of the expansion of the universe (section 1.13) and we expect the current peculiar velocity to obey $\nabla_{\mathbf{r}} \times \mathbf{v} = 0$. If this is the case, then one

can write the velocity in terms of a peculiar velocity potential defined by $\mathbf{v} \equiv -\nabla\Phi_{\rm vel}/a$. With this definition, equation (4.7) can be integrated to give

$$\Phi_{\rm vel} = \frac{2f(\Omega)}{3H\Omega}\,\phi_{\rm grav}. \tag{4.8}$$

Suppose we define a new potential $\Phi_{\rm num}$ in terms of the perturbation of galaxy *number*, by $\nabla^2_{\mathbf{r}}\Phi_{\rm num} \equiv (\delta n/n)$ where n is the number of galaxies, and if we further assume the existence of a linear relationship between *number* and *mass* perturbation via a bias parameter b: $(\delta n/n) \equiv b(\delta\rho/\rho_{\rm b})$, then clearly by equation (1.76) we get $\phi_{grav} = 4\pi G\bar{\rho}\Phi_{\rm num}/b$.

The way to compute $\Phi_{\rm num}$ will be the subject of next section; but for the moment we see that equation (4.8) can now be written in a simple form:

$$\Phi_{\rm vel} = \frac{\Omega^{0.6}}{b}\,\Phi_{\rm num}. \tag{4.9}$$

So in theory a plot of $\Phi_{\rm vel}$ against $\Phi_{\rm num}$ should give us a slope of $\Omega^{0.6}/b$. By this method alone, it is clearly not possible to resolve the values of Ω and b individually. To do that, one would have to determine either the value of Ω or b by another means. For example, if one is to assume that inflation did occur in the early epoch of the universe, then $\Omega = 1$ is the value that is generally expected (e.g. Kolb & Turner 1990). With an assumed value of Ω, we can then shed some light on the value of b by this method.

4.3 Density Field From the IRAS Survey

The IRAS 1.2 Jy catalogue consists of 5313 galaxies, all of which are flux-limited at a wavelength of 60 μm. The sample covers 87.6% of the sky. The raw data of the IRAS survey are the galactic redshifts s_i (where i is the label for each galaxy) along with their angular positions in the sky. In theory then, one would obtain the gravitational potential by

$$\Phi_{\rm grav}(\mathbf{s}) = \sum_i \frac{GM_i}{|\mathbf{s} - \mathbf{s}_i|}, \tag{4.10}$$

where G is the gravitational constant and M_i is the mass of the i^{th} galaxy. However, Such method is slow and there will be problems when $\mathbf{s}$ is very close to $\mathbf{s}_i$. The fact that not all galaxies will be included in the catalogue (due to flux limit) plus the uncertainties between distribution of galaxies and that of mass all add up to further complications. Another main reason for not carrying out such computation is that the velocity potential from POTENT is heavily smoothed and such smoothing process can be carried out much more efficiently when it is done in Fourier space.

4.3.1 Inverse Selection Weighting

In a flux-limited survey, the fraction of galaxies observed is a decreasing function of distance. This is because a smaller fraction of the luminosity function lies above the flux limit at greater distances. In order to convert the raw number counts into true densities, it is therefore necessary to divide them by the selection function $\phi(r)$: the fraction of galaxies included in the catalogue at distance r. To be more precise,

$$N_{\text{obs}}(r) = 4\pi r^2 \bar{\rho} \phi(r) \mathrm{d}r, \tag{4.11}$$

where $N_{\text{obs}}(r)$ is the number of galaxies observed in a shell at a distance r and width $\mathrm{d}r$, and $\bar{\rho}$ is the true mean number density. For the IRAS 1.2 Jy catalogue, the selection function is

$$\phi(r) = A r^{-2\alpha} \left[1 + \left(\frac{r}{r_*} \right)^2 \right]^{-\beta_*}, \tag{4.12}$$

where A=0.189, α=0.421, r_*=50.1h^{-1}Mpc, and β_*=1.913 (Heavens & Taylor 1995 and references therein). For a simple and naive analysis, the galaxies are weighted in the redshift space by the inverse of its redshift selection function $\phi(s)$ which has been optimised as in section 5.3.1. The optimised parameters that were obtained by minimising the χ^2 using a survey radius of 10,000 km/s in the Cosmic Microwave Background (CMB) frame and 60 bins are A=0.5572, α=0.6439, r_*=59.44h^{-1}Mpc, and β_*=1.536. The final result is however not very sensitive to the actual value of the parameters.

With every galaxy carrying its inverse selection weight, a 3-dimensional $128 \times 128 \times 128$ grid was constructed in the supergalactic coordinates and each weighted galaxy is assigned to the nearest grid point. At each grid point the weighted density is the sum of the inverse selection function of all the galaxies that were assigned to that point. The density perturbation at the grid point with position $\mathbf{s}$ is then defined by:

$$\delta(\mathbf{s}) = \frac{n(\mathbf{s})}{\bar{n}} - 1, \tag{4.13}$$

where $n(\mathbf{s})$ is the sum of the weight of galaxies that were truncated to $\mathbf{s}$, and $\bar{n}$ is the average weighted density per grid cell:

$$\bar{n} = \frac{V_{\text{grid}}}{V} \sum_{i=1} \frac{1}{\phi(s_i)}, \tag{4.14}$$

where V_{grid} is the volume of a grid cell, V is the survey volume, and $\phi(s_i)$ is the selection function of the i^{th} galaxy at redshift s.

As the IRAS survey covered only 87.6% of the full sky, those grid points that are in the unobserved region will be given a false negative density perturbation. To counter this flaw, the perturbation at these grid points were set to zero. This is perhaps a democratic solution but it is by no means the correct one for we do not know how many galaxies actually lie in those regions. However, it is a reasonable guess that when it comes to smoothing the data (which is discussed in next section), a zero perturbation in the unobserved region will probably contribute less error to the density of the adjacent observed region compare with the negative perturbation smoothing. Briefly, the excluded regions are the galactic plane ($|b| \lesssim 5 - 10°$), two narrow bands at certain ecliptic longitude, and several ecliptic lune bins which have high source density (section 1.14). With greater distances, the volume of the excluded regions becomes larger and so the contribution to the observed part of the sky increases when smoothing is carried out. It is thus important to limit the comparison with the POTENT field at a small distance. In any case, the POTENT data has errors that increase with distance.

4.3.2 Smoothing the Data

Without processing the data from the IRAS survey, the density field derived from a set of discrete galactic positions will just be a series of spike function in redshift **s**. This does not reflect the underlying density distribution and so one needs to somehow construct a smooth and continuous density field out of a set of discrete data. This process of smoothing usually takes some form of averaging of data in certain region of the sky by means of convolving the nearby galaxy with a window function. One could for example employ a top hat function which convolves only the data that lie within a certain fix radius from the places of interest. A more common window function is the Gaussian one where nearby galaxies are given more weight than those further away. Quantitatively, a smooth density field $\delta_{\rm sm}(\mathbf{s})$ was constructed from the discrete data $\delta(\mathbf{s})$ by

$$\delta_{\rm sm}(\mathbf{s}) = C \int \delta(\mathbf{s}')\, e^{-\frac{|\mathbf{s}-\mathbf{s}'|^2}{2R^2}}\, \mathrm{d}^3\mathbf{s}', \tag{4.15}$$

where $C = (2\pi)^{-3/2}R^{-3}$ is the normalisation factor, and R is the Gaussian radius which was chosen to be 1200 km/s to coincide with that used by POTENT. If there are n grid points in the survey, then the smoothing by equation (4.15) requires each grid point to convolve its data with all other n-1 grid points, and so the total number of convolutions to obtain data for all the n grid points will be in the order of n^2. This is computationally expensive and inefficient. However if the smoothing is done in the wavenumber **k** (where $k \equiv 2\pi/\lambda$ and λ is the length scale) space, the number of calculations will be reduced from n^2 to $n \log n$ by using a fast Fourier transform (NAG Fortran Library Manual, Mark 16, 1993).

The Fourier transform of the smooth $\delta_{\rm sm}(\mathbf{s})$, defined by $\delta_{\rm sm}(\mathbf{k})$ is

$$\delta_{\rm sm}(\mathbf{k}) = \frac{1}{(2\pi)^3} \int \delta_{\rm sm}(\mathbf{s})\, e^{-i\mathbf{k}\cdot\mathbf{s}}\, \mathrm{d}^3\mathbf{s}. \tag{4.16}$$

The Fourier transform of the discrete $\delta(\mathbf{s})$, $\delta(\mathbf{k})$, is also defined in the same way. Equation (4.15) is essentially a convolution equation and one can apply the theory of convolution which states that the Fourier transform of a convolution is the product of the Fourier transform of the separate functions. So $\delta_{\rm sm}(\mathbf{k})$ can be obtained by multiplying $\delta(\mathbf{k})$ with a Gaussian filter $e^{-k^2R^2/2}$.

To obtain $\Phi_{\rm num}(\mathbf{s})$ in $\mathbf{k}$ space, $\Phi_{\rm num}(\mathbf{k})$, one merely needs to multiply $\delta_{\rm sm}(\mathbf{k})$ by $-1/|\mathbf{k}|^2$. The proof goes as follow: The peculiar number density field $\Phi_{\rm num}(\mathbf{s})$ is the inverse Fourier transform of $\Phi_{\rm num}(\mathbf{k})$:

$$\Phi_{\rm num}(\mathbf{s}) = \int \Phi_{\rm num}(\mathbf{k})\, e^{i\mathbf{k}\cdot\mathbf{s}}\, {\rm d}^3\mathbf{k}. \tag{4.17}$$

Differentiating equation (4.17) gives

$$\nabla^2\Phi_{\rm num}(\mathbf{s}) = -\int k^2\Phi_{\rm num}(\mathbf{k})\, e^{i\mathbf{k}\cdot\mathbf{s}}\, {\rm d}^3\mathbf{k}. \tag{4.18}$$

Thus the Fourier transform of $\nabla^2\Phi_{\rm num}(\mathbf{s})$ is $-k^2\Phi_{\rm num}(\mathbf{k})$. If one then takes the Fourier transform of $\nabla^2\Phi_{\rm num} = \delta_{\rm sm}(\mathbf{s})$, it is obvious that

$$\Phi_{\rm num}(\mathbf{k}) = -\frac{\delta_{\rm sm}(\mathbf{k})}{k^2}, \tag{4.19}$$

which is where the afore-mentioned $-1/k^2$ comes in. With $\Phi_{\rm num}(\mathbf{k})$, it is then a straightforward process of inverse Fourier transforming it to obtain $\Phi_{\rm num}(\mathbf{s})$.

Figure 4.1 shows the contour plot of the smoothed IRAS 1.2 Jy peculiar density potential at various supergalactic Z plane within the survey radius of 10,000 km/s in the CMB frame. 3956 galaxies were included within this survey radius.

4.4 Peculiar Velocity Potential from POTENT

At present one does not fully understand the relationship between the galaxy and the underlying mass distribution (i.e. biasing). Given that the assumption of gravity being responsible for the large-scale structure that we observe today seems plausible, the study of peculiar velocities becomes a useful means of probing the mass density in cosmology. In principle, equation (4.8) will be sufficient to extract any information on the gravitational field from the study of peculiar velocity alone. This section gives a brief description of the method known as POTENT which was first introduced by Bertschinger & Dekel (1989) and also in Dekel et al. (1990; hereafter DBF) for constructing the velocity field.

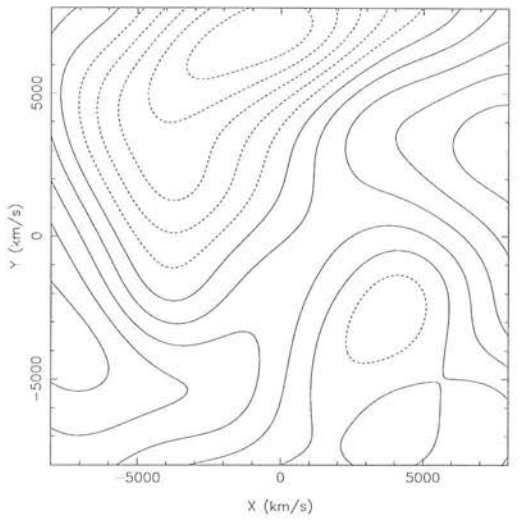

(a) Z=1000 km/s

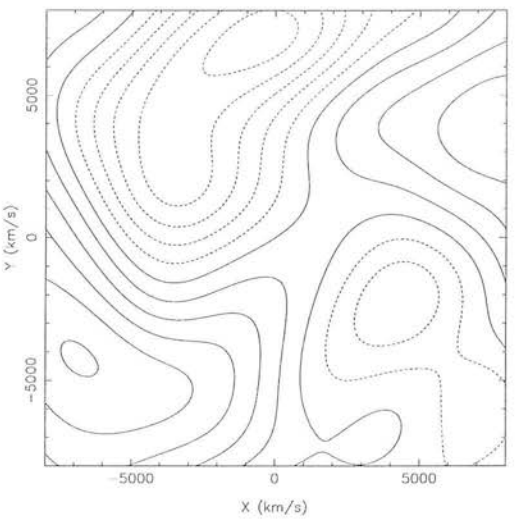

(b) Z=0 km/s

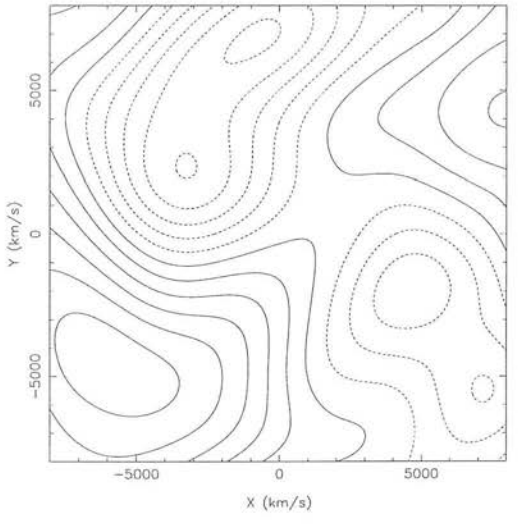

(c) Z=-1000 km/s

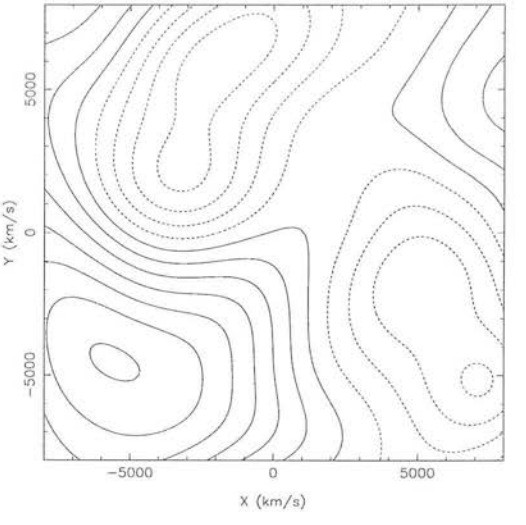

(d) Z=-2000 km/s

Figure 4.1: The peculiar density potential $\Phi_{\rm num}$ of the IRAS 1.2 Jy galaxies at supergalactic Z = (a) 1000 km/s, (b) 0 km/s, (c) -1000 km/s, and (d) -2000 km/s. Each galaxy was weighted by its inverse selection function $\phi(s)$ and a Gaussian smoothing window of 1200 km/s was used. A grid of $128 \times 128 \times 128$ was used in truncating the galaxies to the grid points. The data were produced by myself using the method described in section 4.3. The solid and dashed lines denote positive and negative density perturbations respectively. The contour spacing is 2.94×10^5 (km/s)^2.

The pillar of this method is the assumption of a potential flow with no vorticity, i.e. $\nabla \times \mathbf{v} = 0$. Without the tangential component of the peculiar velocities, this assumption is not testable. But one theoretical justification for this assumption is that in the linear perturbation theory of an expanding universe, the growing mode corresponds to an irrotational flow (section 1.13). Also according to Kelvin circulation theorem, the fluid circulation around a closed contour fixed in the fluid is conserved for an isentropic flow. So if the flow was irrotational during the linear regime, the zero circulation of the potential flow is preserved. The circulation theorem breaks down for a collisional fluid if the flow is not isentropic or if viscous dissipation occurs. It also fails for the collisionless flow when the fluid trajectories cross. Thus, in a collapsing regions where there might be particle orbits mixing, vorticity can be generated. However, it is expected that such vorticity will have negligible amplitude on the scales that the POTENT is concerned, so that when the velocity field is smoothed to remove small-scale nonlinearity, potential flow remains a good approximation. A more detailed justification of the potential flow is given in DBF.

If the assumption of the potential flow is true, one can write $\mathbf{v}$ in the form of a scalar velocity potential:

$$\mathbf{v} = -\nabla \Phi_{\rm vel}. \tag{4.20}$$

The obvious way of obtaining $\Phi_{\rm vel}$ is to integrate $\mathbf{v}$ spatially. However this is not possible as we can only measure the radial component of $\mathbf{v}$, v_r. The only way the potential at any spatial point can can be obtained is to integrate v_r radially:

$$\Phi_{\rm vel}(r, \theta, \phi) = -\int_0^r v_r(r', \theta, \phi)\, \mathrm{d}r'. \tag{4.21}$$

This in essence is the method of POTENT. Although this method sounds plausible in theory, the actual measurement of v_r is itself flawed with both systematic and random biases. Most of the efforts in DBF have been spent in dealing with such biases.

The raw ingredients of POTENT are a set of distances r_i and redshifts z_i (corrected to the CMB frame) for a set of N galaxies along with the angular directions $\hat{\mathbf{r}}_i$. The

quantity r_i is the actual distance from us and its measurement is independent of the redshift of the object. For spiral galaxies, r_i is measured by the infrared Tully-Fisher law (Tully & Fisher 1977), which relates rotation velocity to the absolute magnitude (e.g. Aaronson et al. 1979). For ellipticals, the $D_n - \sigma$ law is used, where the velocity dispersion is related to a photometrically measured diameter (e.g. Dressler et al. 1987a; Djorgovski & Davis 1987).

With these measurements, the radial peculiar velocity is $v_i = cz_i - r_i$. The errors in measuring z_i and $\hat{\mathbf{r}}_i$ are negligible, but measurements in r_i do give errors that are significant. These errors arise because galaxies do not obey the scaling law exactly and the variances σ_i^2 increase with the distance, $\sigma_i^2 = (\Delta r_i)^2$. In the paper of DBF, Δ=0.16 and 0.21 for spirals and ellipticals respectively, reduced by a factor of N for a group with N measured galaxies.

4.4.1 Maximum Likelihood Smoothing

Given that $\Phi_{\rm vel}(\mathbf{r})$ needs the radial integration of v_r, it is essential to somehow construct a smooth v_r out of the sparse and noisy data. The simplest way of obtaining a smoothed radial velocity at $\mathbf{r}$ is to average the radial velocities of nearby galaxies with weights given by a window function. As different galaxies do not have the same radial direction as $\hat{\mathbf{r}}$, a tensor window function was used which projected the radial velocities onto $\hat{\mathbf{r}}$. In obtaining the estimate of the local radial velocity, DBF maximised the likelihood function which incorporated the window function W:

$$\mathcal{L}(\mathbf{r}) = -\frac{1}{2}\sum_i W(\mathbf{r},\mathbf{r}_i)\,[v_i - \hat{\mathbf{r}}_i\cdot\mathbf{v}(\mathbf{r})]^2, \tag{4.22}$$

where v_i is the radial peculiar velocity of the $i^{\rm th}$ galaxy which lies in the direction $\hat{\mathbf{r}}_i$ and has a distance of r_i. The estimated peculiar velocity at $\mathbf{r}$ is $\mathbf{v}(\mathbf{r})$, of which one is interested in the radial component $v_r(\mathbf{r})$. By maximising the likelihood with respect to $v_r(\mathbf{r})$, DBF obtained

$$v_r(\mathbf{r}) = \sum_i \tilde{W}(\mathbf{r},\mathbf{r}_i)\,v_i, \tag{4.23}$$

$$\tilde{W}(\mathbf{r}, \mathbf{r}_i) = \left[\hat{\mathbf{r}}.\mathbf{A}^{-1}(\mathbf{r}).\hat{\mathbf{r}}_i\right] W(\mathbf{r}, \mathbf{r}_i) \quad , \quad \mathbf{A} \equiv \sum_i W(\mathbf{r}, \mathbf{r}_i)\hat{\mathbf{r}}_i\hat{\mathbf{r}}_i.$$

It was the quantity $v_r(\mathbf{r})$ so obtained that provided the input of the integration of equation (4.21).

4.4.2 Optimal Window Function

To obtain an estimate of the local velocity at $\mathbf{r}$ by averaging the velocities of the neighbouring galaxies, the window function should have the property of giving more weight to galaxies that are close to $\mathbf{r}$ than those that are further away. A simple and convenient window function that has such property is a spherically symmetric Gaussian centred on $\mathbf{r}$. This simple Gaussian however gives $v_r(\mathbf{r})$ that has large variance. To reduce the variance, it is necessary to give less weight to galaxies that have large distance errors. So a better window function will be

$$W(\mathbf{r}, \mathbf{r}_i) = \frac{1}{\sigma_i^2} \exp\left[-\frac{|\mathbf{r} - \mathbf{r}_i|^2}{2{R_w}^2}\right], \tag{4.24}$$

where R_w is the Gaussian width that one can freely choose, and σ_i^2 is the variance in radial peculiar velocity. Lynden-Bell et al. (1988) and DBF used $\sigma_i^2 = \Delta^2 r_i^2 + \sigma_f^2$ and $\sigma_f = 150$ km/s was adopted by DBF.

This spherical Gaussian window with inverse variance weighting does however, suffer from the sampling gradient bias. Imagine for the moment that if velocity gradients do exist in a region with the size comparable to the smoothing radius R_w, the velocity field from patches of high galaxy density will artificially propagate into patches of low density. This is because overall the window function of (4.24) gives less weight to velocity field of low density regions than that of high density regions when a galaxy sum is performed by equation (4.23). So instead of getting the expected velocity gradient, the region will have a velocity field that resembles that of the high galaxy density. This systematic bias will persist even if the random errors σ_i for every galaxy are eliminated. To minimise this bias, one would weight the galaxy by the inverse of its ambient density.

In a region of high galaxy density such as a cluster with N galaxies, the variance in distance measurement is reduced by a factor of $N^{-1/2}$. However the requirement to weight each galaxy by the inverse of its ambient density means that the appropriate weighting becomes a question of nontrivial optimisation: a high density region will have high weighting in its $1/\sigma_i^2$ term but then this is reduced by the inverse weighting of its density. The same problem arises for the low density region as well. A compromise was chosen by DBF which took into the account of weighting by inverse distance variance and inverse density bias:

$$W(\mathbf{r}, \mathbf{r}_i) = \frac{R_{4i}^3}{\sigma_i^2} \exp\left[- \frac{|\mathbf{r} - \mathbf{r}_i|^2}{2{R_w}^2} \right], \tag{4.25}$$

where R_{4i} is the distance from the i^{th} galaxy to its 4^{th} nearest neighbour. The number 4 was chosen after the trial and error efforts of DBF to minimise the bias in Monte Carlo simulations. A Gaussian window radius of $R_w = 1200$ km/s was chosen in POTENT.

Figure 4.2 shows the contour plot of the POTENT mark II (Dekel, private communication) velocity field at various supergalactic Z plane. The are $33 \times 33 \times 33$ grid points with a spacing of 500 km/s. The location of the depression in the contour is consistent with that of the so-called Great Attractor found in e.g. Lynden-Bell et al. (1988) which has a supergalactic coordinate $X \approx -4000$ km/s, $Y \approx 1000$ km/s, and $Z \approx -500$ km/s. It is thought that this attractor could be due to the presence of the Hydra-Centaurus supercluster.

4.5 Results and Discussion

With the velocity field of POTENT and the peculiar number density field of the IRAS 1.2 Jy galaxies, one should be able to estimate the quantity $\beta \equiv \Omega^{0.6}/b$ by virtue of equation (4.9). The plot of these two fields within a radius of 2500 and 3000 km/s is shown in figure 4.3. Each point in the plot of figure 4.3 has a spacing of 1500 km/s along the three directions of the grid. A spacing of 1500 km/s instead of the 500 km/s POTENT grid spacing was chosen to ensure that every point in the plot is more or less independent of each other even though the data was smoothed within a Gaussian radius

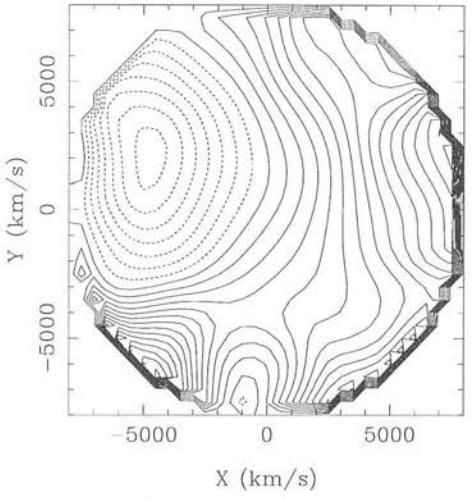

(a) Z=1000 km/s

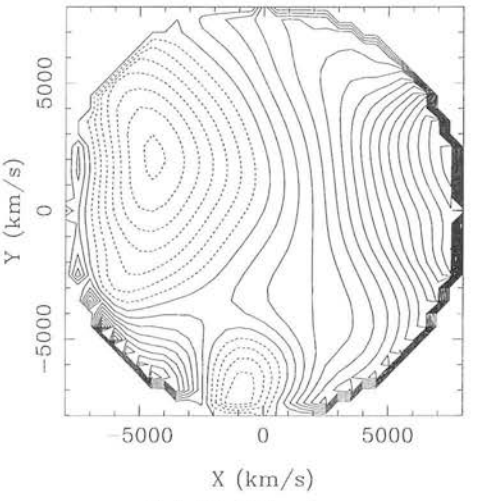

(b) Z=0 km/s

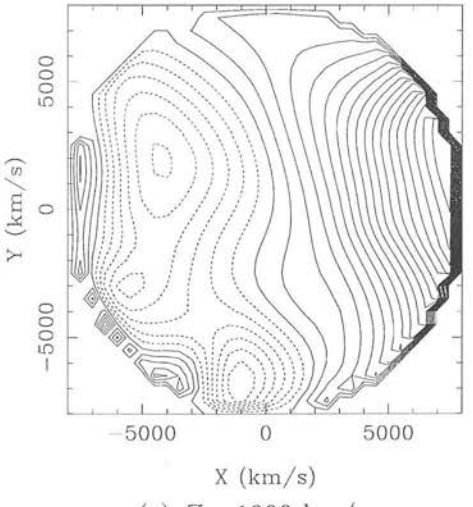

(c) Z=-1000 km/s

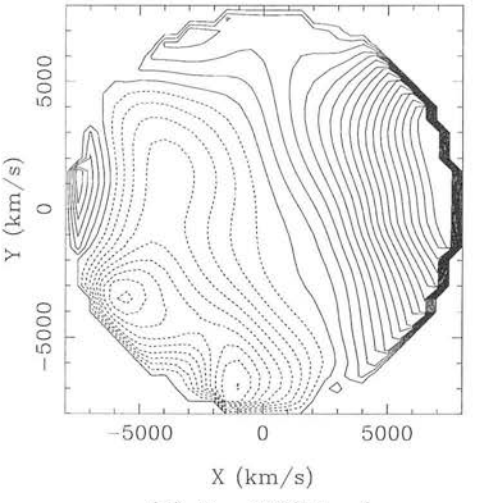

(d) Z=-2000 km/s

Figure 4.2: Contour plot of the POTENT velocity field by DBF in supergalactic (a)Z=1000 km/s, (b)Z=0 km/s, (c)Z=-1000 km/s, and (d)Z=-2000 km/s planes. The contour spacing is 2.94×10^5 (km/s)^2 and a Gaussian smoothing radius of R_w=1200 km/s was used. The solid and dashed lines denote positive and negative contours respectively. These contour plots were produced using POTENT data of DBF which were obtained by private communication with Dekel.

of 1200 km/s. For the POTENT grid points that were included in the plot, the number density field at those points were estimated by a 3D linear interpolation to the nearest 8 IRAS cubic points.

We see from figure 4.3 that locally the correspondence between the predicted and measured potential fields is good, and the comparison yields a value of $\beta \simeq 1$. However, as the comparison radius is increased, the correspondence becomes poor. This is also shown by inspection of the potentials in figures 4.1 and 4.2. There are several possible sources of this discrepancy. Firstly, comparisons of this sort are very noisy, at least when applied to individual galaxies (see Kaiser et al. 1991), but this should be reduced by the smoothing applied here. This scatter ultimately arises from scatter in the distance indicators and also from the nonlinear contribution to the gravity field. A residual effect is the systematic error in $\Phi_{\rm POTENT}$ which comes from the construction method of POTENT: the integration propagates errors to all larger radii, and this will not be removed by the smoothing. The obvious way in which this method can be improved is to have accurate distance measurements to all galaxies instead of having to rely on their redshift distances.

The potential contour in figures 4.1 and 4.2 are consistent with the existence of the Great Attractor found by Lynden-Bell et al. (1988) at supergalactic $X \approx -4000$ km/s, $Y \approx 1000$ km/s, and $Z \approx -500$ km/s. The process in obtaining the IRAS density field is however flawed in that the effect of the redshift distortion by the peculiar velocity was not taken into account. In other words, the density distribution in real space might be very different from that of redshift space. The typical peculiar velocity of a galaxy is in the region of a few hundred km/s and the process of truncation of a galaxy to a grid point and smoothing might have erased such information even if such distortion was taken into account. The results of comparing the data from IRAS and that of POTENT in this analysis are thus slightly primitive and simplistic. Nevertheless, within the error bounded by this analysis, it seems very unlikely that a linear plot of the IRAS and POTENT field could occur by chance. It is therefore reasonable to conclude that there is a relationship (perhaps a linear one) between the velocity and the distribution of galaxies.

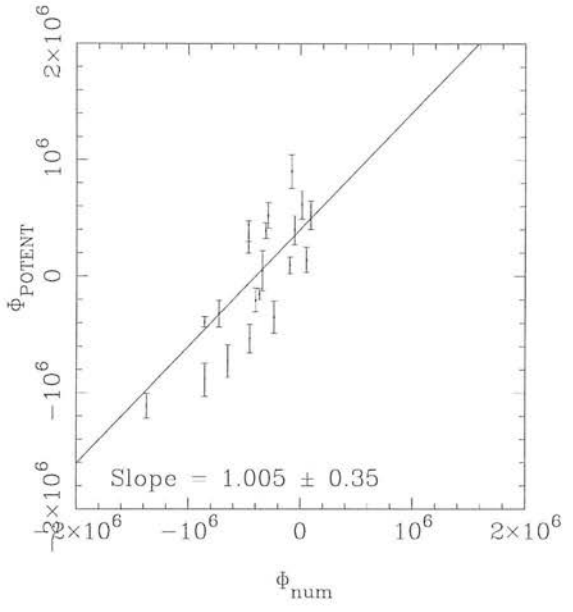

(a)

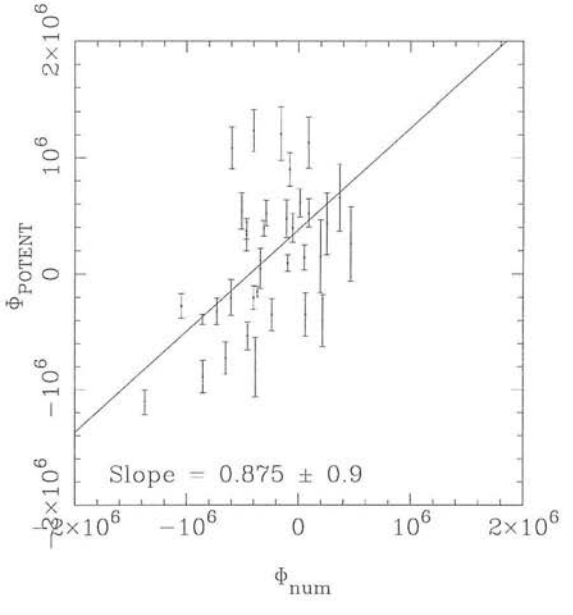

(b)

Figure 4.3: Plot of the POTENT velocity field of DBF against the density field of the IRAS 1.2 Jy survey within a radius of (a) 2500 km/s, and (b) 3000 km/s. Both fields were smoothed by a Gaussian window of 1200 km/s. Each point on the plot has a separation of 1500 km/s along the three directions of the grid and the unit is in $(km/s)^2$. The error bars in Φ_{POTENT} were reproduced from POTENT data of DBF. The slope gives the value of β from the analysis of section 4.2.2.

Although not rigorous enough because the redshift distortion was ignored (treated in chapter 5), the purpose of this chapter is to show a possible way forward of analysing the velocity and density field. At present, the uncertainties in the distance determination and the absence of the full sky coverage are still the biggest hurdles to overcome if this analysis is to be useful in determining the value of β.

Chapter 5

Multipole Velocity Field From Galaxy Samples

Abstract

Using spherical harmonics, a differential equation relating the predicted peculiar velocity field to the galaxy perturbation distribution was solved for different multipole coefficients. The predicted dipole velocity field constructed using terms up to $l = 1$ was then compared with that from the measurement of POTENT. The same comparison was also carried out with $l > 1$ multipole velocity field. The results of these comparisons are presented for different value of β, where $\beta \equiv \Omega^{0.6}/b$ is the ratio of the density to the bias parameter.

5.1 Introduction

In the last chapter, we made an attempt of estimating β by comparing the potential predicted by density field to the velocity potential of POTENT. The analysis is however flawed by the fact that the redshift distortion was not taken into the account. As the result in chapter 3 shows, this redshift distortion is not negligible and so any credible analysis should correct such distortion. Also the smoothing process in chapter 4 effectively cuts off the influence of galaxy distribution outside the regions of interest.

If gravity is the dominant force dictating the motion of the present universe, then the mass distribution should tell us the dynamics of the universe. Such dynamics will be manifested through the motion of galaxies. In principle, this theory can be tested if we know the mass distribution, which can then be compared to the observed galactic motion. However, the observed distribution of galaxies in redshift space differs significantly from the actual mass distribution due to three main effects: (1) There is a distortion in converting from redshift to real space; (2) Distribution of galaxies may differ from the mass distribution; and (3) galaxy surveys are prone to flux-limit selection bias.

Such limitations are of course unfortunate but all is not lost if we can utilise the galaxy survey under certain assumptions and approximations. The first assumption is that the redshift and real space coordinates are linearly related to each other via the growth factor $f(\Omega) \simeq \Omega^{0.6}$ (e.g. Kaiser 1987, Nusser & Davis 1994, hereafter ND) and that one can extract the mass perturbation from galaxy count by the bias parameter b.

The real space and the redshift coordinates are related to each other via the peculiar velocity $\mathbf{v}$, which is assumed to be curl free (i.e. $\nabla \times \mathbf{v}=0$) and thus can be written in terms of a velocity potential Φ by $\mathbf{v} \equiv -\nabla\Phi$. With this assumption, the density perturbation in redshift space can be written in terms of this velocity potential in the form of a modified form of the peculiar Poisson equation. This partial differential equation (P.D.E.) has only one free parameter, $\beta \equiv \Omega^{0.6}/b$. By resolving the velocity potential in the spherical harmonics and using the redshift density perturbation data from the IRAS 1.2 Jy survey, the P.D.E. changes to a set of O.D.Es. (equation (5.20)), it is then possible to solve each harmonic component of the potential for different value of β, subject to certain boundary conditions. For $l = 0$ (monopole) and $l = 1$ (dipole) harmonic terms, the potential at redshift $\mathbf{s}$ depends only on the distribution of matter inside a sphere of radius $s = |\mathbf{s}|$; while $l > 1$ potential is affected by the matter distribution from the origin out to infinity. Therefore monopole and dipole potential can be easily solved by initial value shooting method from the origin (i.e. using some suitable boundary conditions at the origin). For the $l > 1$ multipole potential, one needs to choose a suitable boundary condition at large s and utilise a shoot and match method and hence the O.D.E. is generally more difficult to solve.

The potential constructed from the O.D.E. is then compared with that from the POTENT (section 4.4) which also assumed a curl free potential flow but its potential was constructed using the measurement of the peculiar velocities of galaxies. By requiring both of these velocity potentials to be consistent with each other, one could in theory constrain the value of β.

The structure of this chapter is arranged as follows: In section 5.2 the effect of the peculiar velocity on the mass perturbation observed in the redshift space is examined under the Zel'dovich approximation (which was first analysed in ND). In section 5.3 the relationship between the velocity field and the perturbation in mass and observed galaxy number is established, in the context of spherical harmonics. This enables the velocity potential to be extracted from the redshift distribution of galaxies in the form of a differential equation. In section 5.4, the appropriate boundary conditions for the O.D.E. are discussed. One derives at two distinctly different boundary conditions for the $l \leq 1$ (monopole and dipole) terms where the velocity is determined only by the source inside the region of interest, and $l > 1$ multipole where the solution depends on the source distribution throughout the universe. In section 5.5, I describe the method for obtaining the perturbation data from the galaxy survey; the basic idea is to first smooth the discrete galaxy distribution with a Gaussian window, and then convert the smoothed data into their spherical harmonic component. In section 5.6, the potential obtained from the O.D.E. with different values of β is compared to that of the POTENT for the monopole and dipole component, and that of higher multipole. Finally the result of all the analysis is discussed in section 5.7 .

5.2 Redshift Distortions

Given a distribution of galaxies in redshift space, we want to know what the gravity induced velocity field is. This is not a straight forward process from the redshift survey as the galaxies will be attracted to regions of high *mass* density in *real* space rather than towards regions of high *number* density in *redshift* space. We follow the derivation of ND.

Let $\mathbf{x}$, $\mathbf{s}$, $\mathbf{v}$, $\mathbf{q}$ be, respectively, the present comoving real space coordinate, the present comoving redshift space coordinate, the comoving peculiar velocity and the initial comoving Lagrangian coordinate of a galaxy; the redshift and real coordinates are related by

$$\mathbf{s} = \left[x + \frac{\mathbf{v}\cdot\hat{\mathbf{x}}}{H_0}\right]\hat{\mathbf{x}}, \tag{5.1}$$

where x and $\hat{\mathbf{x}}$ are the magnitude and the unit vector of $\mathbf{x}$, and H_0 is the Hubble constant (which is equal to 1 if distances are expressed in km/s). To relate the redshift density $\rho(\mathbf{s})$ to the Lagrangian density ρ_q, one needs to relate $\mathbf{x}$ to $\mathbf{q}$ in order that $\mathbf{s}$ can be expressed in terms of $\mathbf{q}$. Provided that the motion of galaxies is not severely affected by nonlinear effects, then one can use the Zel'dovich approximation (ND; Zel'dovich 1970) to predict the evolution of $\mathbf{q}$ to $\mathbf{x}$ via

$$\mathbf{x} = \mathbf{q} + \frac{1}{f(\Omega)}\mathbf{v}, \tag{5.2}$$

where $f(\Omega) \simeq \Omega^{0.6}$. With (5.1) and (5.2), $\mathbf{s}$ can now be written:

$$\mathbf{s} = \mathbf{q} + \frac{1}{f}\mathbf{v} + (\mathbf{v}\cdot\hat{\mathbf{s}})\hat{\mathbf{s}}, \tag{5.3}$$

where $\hat{\mathbf{s}} \equiv \mathbf{s}/s = \hat{\mathbf{x}}$. By mass conservation,

$$\rho(\mathbf{s})\mathrm{d}^3\mathbf{s} = \rho_q \mathrm{d}^3\mathbf{q}. \tag{5.4}$$

The mass density contrast $\delta_s \equiv \delta(\mathbf{s}) = [\rho(\mathbf{s}) - \rho_q]/\rho_q$ can therefore be approximated by

$$\begin{aligned}
\delta_s &= \left\| \frac{\partial q_i}{\partial s_j} \right\| - 1 \\
&= \left\| I - \frac{1}{f}\frac{\partial v_i}{\partial s_j} - \frac{\partial([\mathbf{v}\cdot\hat{\mathbf{s}}]\hat{\mathbf{s}})_i}{\partial s_j} \right\| - 1 \\
&\simeq -\frac{1}{f}\nabla_s\cdot\mathbf{v} - \nabla_s\cdot([\mathbf{v}\cdot\hat{\mathbf{s}}]\hat{\mathbf{s}}),
\end{aligned} \tag{5.5}$$

where I is the identity matrix, the subscript s refers to differentiation in redshift space, i, j=1,2,3 are the label for the coordinate (e.g. x, y, z), and the double bar denotes the determinant of the matrix.

5.3 Velocity Field from Perturbation Theory

In linear perturbation theory, the growing mode of the velocity is curl free, i.e. $\nabla \times \mathbf{v}=0$ (section 1.13), and so $\mathbf{v}$ can be written in terms of a velocity potential Φ by $\mathbf{v} \equiv -\nabla_s \Phi$. With this definition, equation (5.5) is then

$$\frac{1}{f}\nabla_s^2\Phi + \frac{1}{s^2}\frac{\partial}{\partial s}\left(s^2\frac{\partial \Phi}{\partial s}\right) = \delta_s. \tag{5.6}$$

For equation (5.6) to be useful, the mass perturbation δ_s has to be converted to the observable number perturbation δ_s^n. This is done first by deriving the mass perturbation in real space, which reads (cf. equation (5.5))

$$\delta_x = -\frac{1}{f}\nabla_x \cdot \mathbf{v}, \tag{5.7}$$

where subscript x refers to real space coordinate. To first order, $\nabla_x = \nabla_s$, so equations (5.5) and (5.7) give

$$\delta_s = \delta_x - \nabla_s \cdot ([\mathbf{v} \cdot \hat{\mathbf{s}}]\hat{\mathbf{s}}). \tag{5.8}$$

In real space, it is often assumed that the mass perturbation δ_x is related to the number perturbation δ_x^n by the bias parameter b:

$$\delta_x^n = b\delta_x. \tag{5.9}$$

Using the conservation law of galaxy numbers, $n_s \mathrm{d}^3\mathbf{s} = n_x \mathrm{d}^3\mathbf{x}$ where n_s and n_x are the number density in $\mathbf{s}$ and $\mathbf{x}$ space,

$$\begin{aligned}(1+\delta_s^n) &= (1+\delta_x^n)\left\|\frac{\partial x_i}{\partial s_j}\right\| \\ &= (1+\delta_x^n)\left(1 - \nabla_s \cdot ([\mathbf{v} \cdot \hat{\mathbf{s}}]\hat{\mathbf{s}})\right).\end{aligned} \tag{5.10}$$

To first order,

$$\delta_s^n \simeq b\delta_x - \nabla_s \cdot ([\mathbf{v} \cdot \hat{\mathbf{s}}]\hat{\mathbf{s}}). \tag{5.11}$$

Using equation (5.8), the mass perturbation in redshift space is now

$$\delta_s = \frac{1}{b}\left(\delta_s^n + \nabla_s\cdot([\mathbf{v}\cdot\hat{\mathbf{s}}]\hat{\mathbf{s}})\right) - \nabla_s\cdot([\mathbf{v}\cdot\hat{\mathbf{s}}]\hat{\mathbf{s}}). \tag{5.12}$$

With equations (5.6) and (5.12), the velocity potential can now be expressed in terms of the number perturbation in redshift space:

$$\frac{1}{\beta}\nabla_s^2\Phi + \frac{1}{s^2}\frac{\partial}{\partial s}\left(s^2\frac{\partial\Phi}{\partial s}\right) = \delta_s^n, \tag{5.13}$$

where $\beta \equiv f(\Omega)/b$. The form of equation (5.13) and the nature of the galaxy survey suggest that the potential should be separated into its radial and angular components. This is best done by expanding the potential in spherical harmonics. In the context of spherical harmonics, any scalar quantity can be obtained by an infinite sum of the orthonormal bases with the appropriate coefficients, i.e.

$$\Phi(\mathbf{s}) = \sum_{l=0}^{\infty}\sum_{m=-l}^{m=l}\Phi_{lm}(s)Y_{lm}(\theta,\varphi), \tag{5.14}$$

where (θ,φ) are the spherical polar angles; δ_s^n can also be resolved in the same manner. There are different definitions of the spherical harmonic functions; here the function $Y_{lm}(\theta,\varphi)$ is defined as in equation (3.4). With spherical harmonics, equation (5.13) can now be resolved into its individual components:

$$\frac{1}{s^2}\frac{\mathrm{d}}{\mathrm{d}s}\left(s^2\frac{\mathrm{d}\Phi_{lm}}{\mathrm{d}s}\right) - \frac{1}{1+\beta}\frac{l(l+1)\Phi_{lm}}{s^2} = \frac{\beta}{1+\beta}\delta_{slm}^n. \tag{5.15}$$

The δ_{slm}^n is determined from the true perturbation in redshift space which is different from the observed one due to the selection effect. If $n_0(\mathbf{s})$ is the number of galaxies observed, then the true number will be $n(\mathbf{s}) = n_0(\mathbf{s})/\phi(|\mathbf{x}|)$, where $\phi(|\mathbf{x}|)$ is the selection function at real space $\mathbf{x}$. The selection function at $x = |\mathbf{x}| = s - u(\mathbf{s})$ where $u(\mathbf{s}) \equiv \mathbf{v}\cdot\hat{\mathbf{s}}$ can be approximated by $\phi(x) \approx \phi(s) - (\mathrm{d}\phi/\mathrm{d}s)u(s)$ which gives us

$$n(\mathbf{s}) = \frac{n_0(\mathbf{s})}{\phi(x)} \approx \frac{n_0(\mathbf{s})}{\phi(s)}\left[1 + \frac{1}{s}\frac{\mathrm{d}\ln\phi}{\mathrm{d}\ln s}u(\mathbf{s})\right], \tag{5.16}$$

and thus

$$\delta_s^n = \frac{n(\mathbf{s}) - \bar{n}}{\bar{n}} = \delta_0^n(\mathbf{s}) + \frac{1}{s}\frac{\mathrm{d}\ln\phi}{\mathrm{d}\ln s}u(\mathbf{s}), \tag{5.17}$$

where $\bar{n}$ is the average of $n(\mathbf{s})$ over the survey volume, and $\delta_0^n(\mathbf{s})$ is the perturbation of the quantity $n_0(\mathbf{s})/\phi(s)$. The quantity $n_0(\mathbf{s})$ can be obtained without ambiguities from the observation. The selection function $\phi(s)$ however, will have to be determined analytically from the catalogue by some arbitrary optimisation processes.

5.3.1 Selection Function

Given that there is a flux limit on any telescope, faint and/or far galaxies will escape detection and so the number of galaxies observed will not be the true number at that distance. To take account of this effect, the selection function $\phi(s)$ is defined as:

$$\mathrm{d}N(s) = 4\pi s^2\phi(s)\mathrm{d}s, \tag{5.18}$$

where $\mathrm{d}N(s)$ is the number of galaxies observed within the redshift width of $\mathrm{d}s$ centered on s. With the discrete distribution of galaxies in s space, we determine the optimum $\phi(s)$ by minimising the variance χ^2 defined by:

$$\chi^2 = \sum_i \frac{\left[N_i - 4\pi s_i^2\phi(s_i)\mathrm{d}s_i\right]^2}{\sigma_i^2}, \tag{5.19}$$

where i denotes the redshift bin centered on s_i, N_i is the number of galaxies observed in the i^{th} bin, $\mathrm{d}s_i$ is the width of the i^{th} bin and σ_i is the Poisson dispersion of the i^{th} bin and is defined as $\sigma_i = \sqrt{4\pi s_i^2\phi(s_i)\mathrm{d}s_i}$. The analytic selection function for the IRAS 1.2 Jy galaxies in real space x is given by equation (3.18). Using $\phi(s)$ of the same form as in equation (3.18), the four parameters a, α, r_*, and β_* are allowed to vary until the minimum of χ^2 is achieved.

5.4 Differential Equation of the Velocity Field

With the relationship between δ_s^n and the observed $\delta_0^n(\mathbf{s})$ being established (equation (5.17)), we can now finally arrive at the differential equation relating the velocity field and the observed galaxy perturbation using equations (5.15) and (5.17):

$$\frac{1}{s^2}\frac{\mathrm{d}}{\mathrm{d}s}\left(s^2\frac{\mathrm{d}\Phi_{lm}}{\mathrm{d}s}\right) - \frac{1}{1+\beta}\frac{l(l+1)\Phi_{lm}}{s^2} = \frac{\beta}{1+\beta}\left(\delta_{0lm}^n - \frac{1}{s}\frac{\mathrm{d}\ln\phi}{\mathrm{d}\ln s}\frac{\mathrm{d}\Phi_{lm}}{\mathrm{d}s}\right), \tag{5.20}$$

where $\delta_s^n(\mathbf{s}) = \sum_{l=0}^{\infty}\sum_{m=-l}^{m=l}\delta_{0lm}^n(s)Y_{lm}(\theta,\varphi)$. In the absence of the source term (i.e. δ_{slm}^n=0), equation (5.15) has the homogeneous solution of

$$\Phi_{lm}(s) \propto s^{\tilde{l}}, \tag{5.21}$$

where the two roots of $\tilde{l}$ are

$$\begin{aligned} \tilde{l} &= -\frac{1}{2} + \frac{1}{2}\sqrt{1+\frac{4l(l+1)}{1+\beta}} \\ \text{and} \quad -(\tilde{l}+1) &= -\frac{1}{2} - \frac{1}{2}\sqrt{1+\frac{4l(l+1)}{1+\beta}}. \end{aligned} \tag{5.22}$$

The inhomogeneous solution with the source term can be obtained by trying the linear combination of the two homogeneous solutions (see e.g. Mathews & Walker 1970):

$$\Phi_{lm}(s) = C_1(s)s^{\tilde{l}} + C_2(s)s^{-(\tilde{l}+1)}. \tag{5.23}$$

By imposing (for convenience) $C_1's^{\tilde{l}} + C_2's^{-(\tilde{l}+1)} = 0$, where C_1' and C_2' are the derivatives of $C_1(s)$ and $C_2(s)$ with respect to s, equation (5.15) is then

$$(1+\beta)\left[\tilde{l}C_1's^{\tilde{l}-1} - (\tilde{l}+1)C_2's^{-(\tilde{l}+2)}\right] = \beta\delta_{slm}^n. \tag{5.24}$$

With $C_1' = -C_2's^{-(2\tilde{l}+1)}$ from the imposed condition and equation (5.24), $C_1(s)$ and $C_2(s)$ are

$$\begin{aligned} C_1(s) &= \frac{\beta}{1+\beta}\frac{1}{(2\tilde{l}+1)}\int_{s1}^{s}\delta_{s'lm}^n s'^{-(\tilde{l}-1)}\mathrm{d}s', \\ C_2(s) &= -\frac{\beta}{1+\beta}\frac{1}{(2\tilde{l}+1)}\int_{s2}^{s}\delta_{s'lm}^n s'^{\tilde{l}+2}\mathrm{d}s'. \end{aligned} \tag{5.25}$$

The general solution for $\Phi_{lm}(s)$ is then

$$\Phi_{lm}(s) = \frac{\beta}{1+\beta}\frac{1}{(2\tilde{l}+1)}\left[s^{\tilde{l}}\int_{s2}^{s}\delta^{n}_{s'lm}s'^{-(\tilde{l}-1)}\mathrm{d}s' - s^{-(\tilde{l}+1)}\int_{s1}^{s}\delta^{n}_{s'lm}s'^{(\tilde{l}+2)}\mathrm{d}s'\right]. \quad (5.26)$$

The constants $s1$ and $s2$ are fixed by the boundary conditions and for this purpose, we need the radial velocity multipole $v_{lm}(s) = -\mathrm{d}\Phi_{lm}/\mathrm{d}s$, which is

$$\begin{aligned} v_{lm}(s) &= -\frac{\beta}{1+\beta}\frac{1}{(2\tilde{l}+1)}[(\tilde{l}+1)s^{-(\tilde{l}+2)}\int_{s1}^{s}\delta^{n}_{slm}s'^{(\tilde{l}+2)}\mathrm{d}s' \\ &\quad + \tilde{l}s^{\tilde{l}-1}\int_{s2}^{s}\delta^{n}_{slm}s'^{-(\tilde{l}-1)}\mathrm{d}s']. \end{aligned} \quad (5.27)$$

This is the velocity multipole equation obtained by ND. In the Local Group (LG) frame, the velocity vanishes at small s. Since $\tilde{l} \leq l$ from equation (5.22), $\tilde{l} \leq 1$ for monopole ($l = 0$) and dipole ($l = 1$). To avoid the divergence of both $\Phi_{lm}(s)$ and $v_{lm}(s)$ at small s, $s1 = s2 = 0$ for $l = 0$ and 1. For multipoles with $l > 1$, the requirement that the $\Phi_{lm}(s)$ to be finite at large s gives $s1 = 0$ and $s2 = \infty$. Thus in terms of integrating equation (5.20) by numerical method, $l = 0, 1$ terms can be obtained by initial value boundary shooting from $s = 0$ up to s without worrying about the boundary condition beyond s. Such property is not unexpected as $l = 0, 1$ velocity is merely a translational movement without any distortion of the shell and so any matter outside the sphere will attract both the LG and the shell equally. For $l > 1$ terms, $\Phi_{lm}(s)$ are affected by the galaxy distribution outside s and one needs to assume certain boundary conditions beyond s. The boundary conditions and the numerical methods for the two cases will be discussed separately in section 5.6.

5.5 Obtaining the Density Perturbation

Using the fact that $\int Y_{lm}(\Omega)Y^{*}_{l'm'}(\Omega)\mathrm{d}\Omega = \delta^{\mathrm{K}}_{ll'}\delta^{\mathrm{K}}_{mm'}$ where $\Omega = (\theta, \varphi)$, $\delta^{\mathrm{K}}_{ll'}$ and $\delta^{\mathrm{K}}_{mm'}$ are the Kronecker delta functions (i.e. $\delta^{\mathrm{K}}_{ll'} = 1$ for $l = l'$ and 0 otherwise),

$$\delta^{n}_{0lm}(s) = \int \delta^{n}_{0}(\mathbf{s})Y^{*}_{lm}(\theta, \varphi)\mathrm{d}\Omega. \quad (5.28)$$

The observed galaxy perturbation $\delta_0^n(\mathbf{s})$ in the LG frame is obtained using the IRAS 1.2 Jy catalogue up to a redshift of 20,000 km/s. Within this radius, there are 4921 galaxies. However, as there is about 12% of the sky that was not observed, the $\delta_{0lm}^n(s)$ obtained will favour some particular l and m (e.g. for modes that have nodal lines in the unobserved regions $\delta_{0lm}^n(s)$ will be bigger). To counter this effect, an artificial catalogue of galaxies is generated in the masked region so that a full sky coverage is achieved. To ensure that the generated galaxies have the same radial profile as the original one, a random number $s_{\rm ran}$ between 0 and $V_{\rm max}^{1/3}$ (where $V_{\rm max} = (20{,}000\ {\rm km/s})^3$, the choice is arbitrary) is generated, a second random number $n_{\rm ran}$ between 0 and 1 is also generated and one condition that an artificial galaxy has to satisfy is that $\phi(s_{\rm ran})$ is greater than $n_{\rm ran}$. In addition a random angular φ between 0 and 2π and $\cos\theta$ between -1 and 1 were also generated and an artificial galaxy will only be generated when $\phi(s_{\rm ran}) > n_{\rm ran}$ and its angular position lies in the excluded regions. If the angular position lies in the observed part of the sky, a *supposed* observed galaxy is generated (which is of course not added to the survey). This process is continued until the supposed observed galaxy number equals that of the real catalogue. The four optimised parameters of the selection function utilised corresponds to survey radius of 20,000 km/s and 80 bins (see section 5.3.1). There were 651 artificial galaxies generated which account for 11.7% of the 5572 final total number. Figure 5.1 shows the histogram of the artificial galaxies.

With this new catalogue each galaxy is assigned a weight of its inverse selection function $1/\phi(s)$. $\bar{n}$ is then the volume averaged weight:

$$\bar{n} = \frac{1}{V}\sum_{i=1}\frac{1}{\phi(s_i)}, \tag{5.29}$$

where V is the survey volume and i is the label for each galaxy. Using a box of 64^3 grid points, the weight of each galaxy is then split linearly among the 8 corners of the cube where the galaxy happens to be lying in according to the distance from each corner to the galaxy. $\delta_0^n(\mathbf{s})$ at the grid point position $\mathbf{s}$ is then determined by:

$$\delta_0^n(\mathbf{s}) = \frac{\sum_{i=1} W(\mathbf{s}_i) - \bar{n}}{\bar{n}}, \tag{5.30}$$

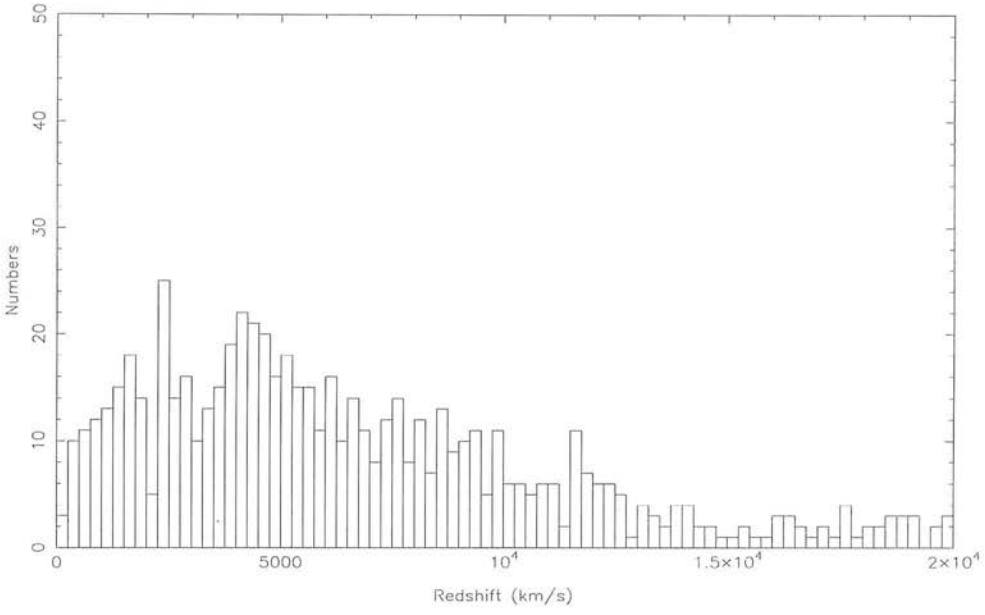

Figure 5.1: Histogram of the 651 artificial galaxies generated in the unobserved region of the IRAS 1.2 Jy catalogue.

where $W(\mathbf{s}_i)$ is the weight contributed by the i^{th} galaxy at the grid point $\mathbf{s}$. The analysis so far has assumed that a smooth $\delta_0^n(\mathbf{s})$ in $\mathbf{s}$ can be observed. In reality, the discrete galaxy distribution will render the $\delta_{0lm}^n(s)$ to be rather noisy. To reduce the noise level, it is essential to obtain a smooth $\delta_0^n(\mathbf{s})$ from the discrete distribution. This can be achieved by convolving every galaxy with a Gaussian window. The details of the smoothing process are outlined in section 4.3.2. As this analysis will compare the potential field from the POTENT, the same Gaussian window of 1200 km/s was used in the smoothing. With a smooth $\delta_0^n(\mathbf{s})$, it is then a straight forward process to obtain $\delta_{0lm}^n(s)$ via equation (5.28). 40 points were used and linear interpolation between two points was used to obtain $\delta_{0lm}^n(s)$ at any particular s.

5.6 Comparison of Potential Field

5.6.1 POTENT Data in the Local Group Frame

As the POTENT data give velocity potential in the Cosmic Microwave Background (CMB) frame, it is necessary to transform the data to the LG frame. POTENT potential is obtained by integrating the velocity data in equation (4.21) where v_r is the radial component of the velocity $\mathbf{v}$ in the CMB frame. By replacing $\mathbf{v}$ with $\mathbf{v} - \mathbf{v}_{\rm LG}$ where $\mathbf{v}_{\rm LG}$ is the Local Group velocity in the CMB frame, The POTENT potential in the LG frame is then

$$\Phi_{\rm LG}(r, \theta, \varphi) = \Phi(r, \theta, \varphi) + \mathbf{v}_{\rm LG} \cdot \mathbf{r}. \tag{5.31}$$

The $\mathbf{v}_{\rm LG}$ used was 622 ± 20 km/s towards galactic $l = 277° \pm 2°$, $b = 30° \pm 2°$ (Dressler et al. 1987b, and references therein). Figures 5.2 and 5.3 show the potential contours in the CMB and the LG frame on the supergalactic $Z = 0$ km/s and $X = 0$ km/s planes. 33^3 grid points with a spacing of 500 km/s were used.

5.6.2 Monopole And Dipole Potential

As the analysis in section 5.4 shows, the monopole ($l = 0$) and the dipole ($l = 1$) potential can be obtained by imposing a boundary condition at $s = 0$. In the LG frame, $\Phi_{lm}(s) = \mathrm{d}\Phi_{lm}(s)/\mathrm{d}s = 0$ at the origin and integration of the O.D.E of (5.20) was carried out with different β. A potential using only the $l = 0, 1$ terms is then constructed on 32^3 grid points. To compare the Monopole and the Dipole terms of the POTENT field, the POTENT data in the LG frame was resolved into its spherical harmonic components and then reconstructed using only the $l = 0, 1$ terms. Figure 5.4 shows the potential contour of the POTENT and that of the O.D.E. using $\beta = 1.0$.

To make a quantitative comparison, the POTENT velocity potential is plotted against that from the O.D.E. integration (see figure 5.5) for $\beta = 0.1$, 0.5, 1.0, 1.5 and 2.0 . As a Gaussian smoothing was used, points that are close together will be strongly correlated. To avoid such correlation from biasing the result, every point in the plot has along any

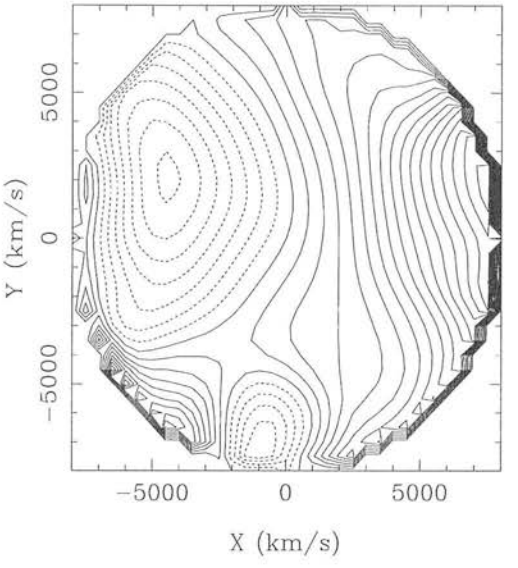

(a)

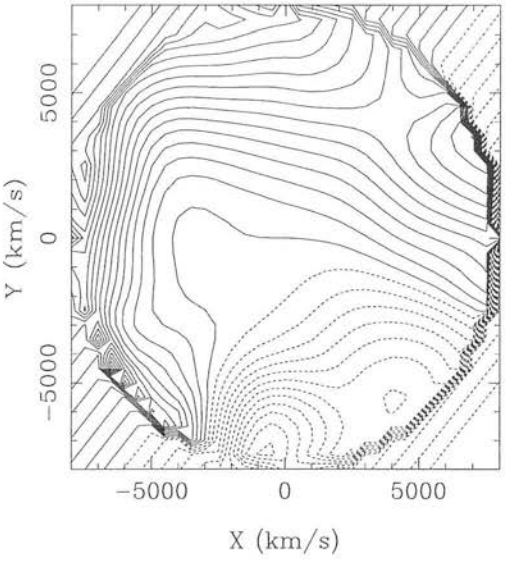

(b)

Figure 5.2: The POTENT velocity potential for the $Z = 0$ km/s supergalactic plane in the (a) CMB and (b) Local Group frame. The LG velocity used was 622 ± 20 km/s towards galactic $l = 277° \pm 2°$, $b = 30° \pm 2°$.

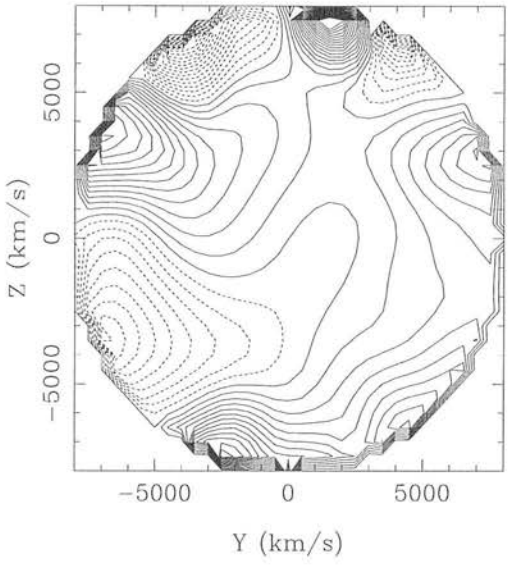

(a)

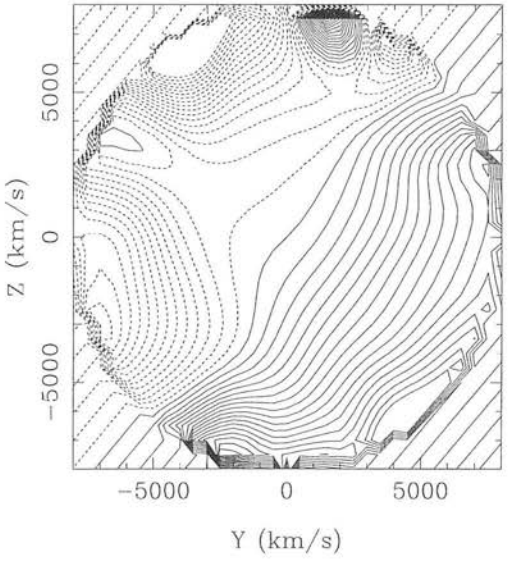

(b)

Figure 5.3: The POTENT velocity potential for the $X = 0$ km/s supergalactic plane in the (a) CMB and (b) Local Group frame. The LG velocity used was 622 ± 20 km/s towards galactic $l = 277° \pm 2°$, $b = 30° \pm 2°$.

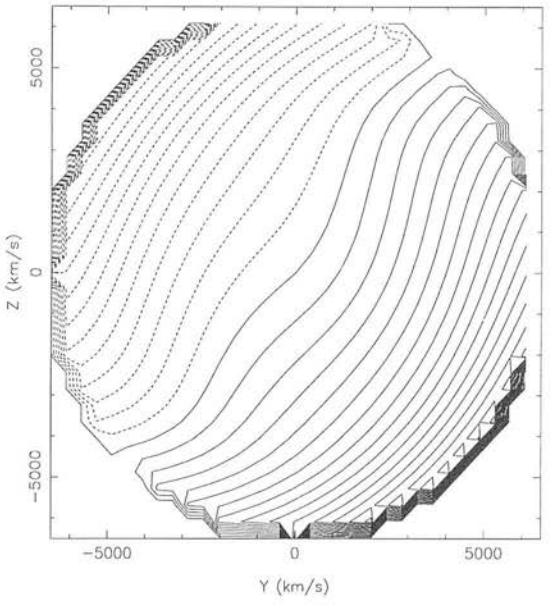

(a)

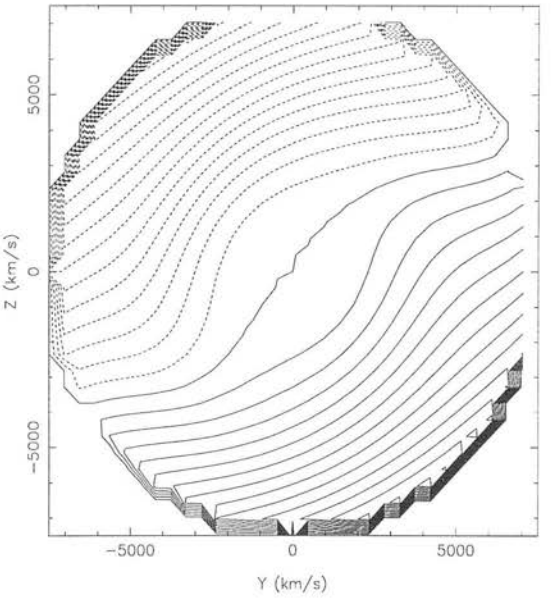

(b)

Figure 5.4: Potential contour in the LG frame (X=0 km/s plane) constructed using $l = 0, 1$ for (a) POTENT and (b) O.D.E. with $\beta = 1.0$.

grid direction a spacing of 1200 km/s, the Gaussian smoothing length. This spacing enables every comparison points to be more or less independent of each other. A radius of 6000 km/s comparison limit in the supergalactic space was set to minimise the big error associated with POTENT data at large distance. Unlike the analysis in chapter 4 where β is determined by measuring the gradient of the potential plot, here we need to find the β which gives a line of unit slope in figure 5.5.

From the result of comparing the monopole and dipole potential field of the POTENT and that obtained from the O.D.E., a high value of β seems to be more favourable. Here the results suggest a value of β in excess of about 2. This contradicts the value of $\simeq$0.6 found by Nusser & Davis (1994) where the dipole velocity was compared. However as Newsam et al. (1995) pointed out, the POTENT data are contaminated with systematic errors and it is unclear how these errors will affect our results.

5.6.3 $l > 1$ Multipole Potential

As concluded in section 5.4, $l > 1$ multipole potentials are dependent on the boundary condition at infinity. Numerically, such approximation is achieved by solving the O.D.E. equation inside a radius of 20,000 km/s which should provide a big enough buffer for $\Phi_{lm}(s)$ within a radius of 8000 km/s, the survey radius of the POTENT.

Close to the origin, the velocity multipole term $\mathrm{d}\Phi_{lm}(s)/\mathrm{d}s$ in LG frame is negligible and $\delta^n_{0lm} = 0$ for $l \neq 0$. So equation (5.20) becomes:

$$\frac{\mathrm{d}^2\Phi_{lm}}{\mathrm{d}s^2} \approx \frac{l(l+1)}{1+\beta}\frac{\Phi_{lm}}{s^2}. \tag{5.32}$$

The asymptotic solutions to equation (5.32) are $\Phi_{lm} \propto s^{\tilde{l}_1}$ and $\Phi_{lm} \propto s^{(1-\tilde{l}_1)}$ where

$$\tilde{l}_1 = \frac{1}{2}\left[1 + \sqrt{1 + \frac{4l(l+1)}{1+\beta}}\right]. \tag{5.33}$$

Since $\tilde{l}_1 > 1$ and $(1 - \tilde{l}_1) < 0$, the correct asymptotic solution for the potential near the origin is

$$\Phi_{lm}(s) = C_1 s^{\tilde{l}_1}. \tag{5.34}$$

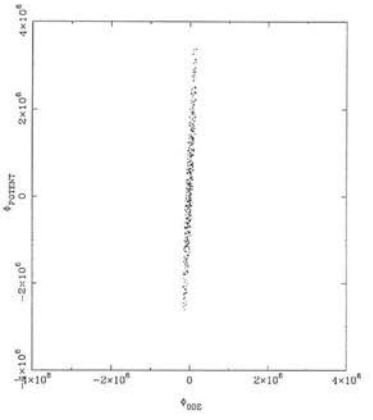

(a) β=0.1

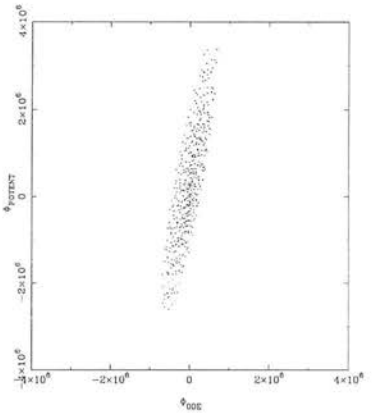

(b) β=0.5

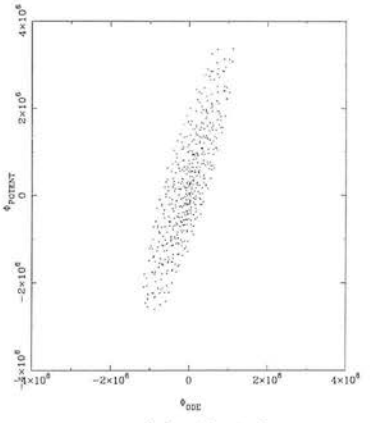

(c) β=1.0

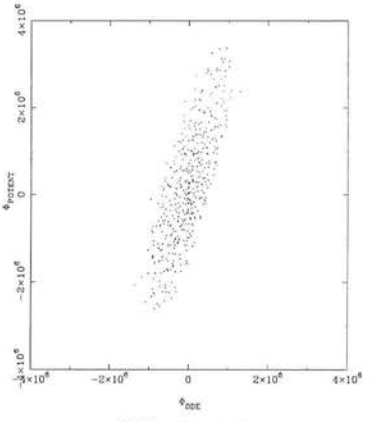

(d) β=1.5

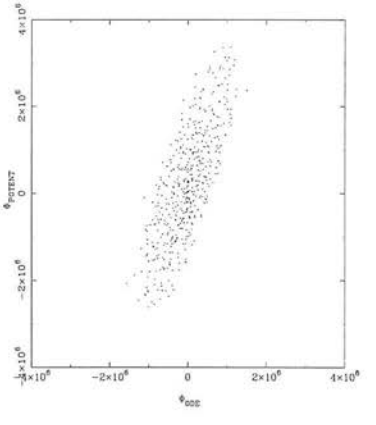

(e) β=2.0

Figure 5.5: Plot of monopole ($l = 0$) plus dipole ($l = 1$) component of POTENT velocity potential in the LG frame $\Phi_{\rm POTENT}$ against velocity potential obtained by O.D.E. $\Phi_{\rm ODE}$ within a 6000 km/s radius for β of (a) 0.1, (b) 0.5, (c) 1.0, (d) 1.5 and (e) 2.0 . Each comparison point has a spacing of 1200 km/s along any grid direction and the unit of the potential is in $(\mathrm{km/s})^2$.

where C_1 is a free parameter.

For a given thickness of a shell, its volume increases with s and statistically, the value of $n(s)$ for the shell at large s should approach that of $\bar{n}$. It is then reasonable to assume that $\delta^n_{0lm}(s)$ becomes negligible. Using the selection function of the form of equation (3.18), equation (5.20) becomes

$$\frac{\mathrm{d}^2\Phi_{lm}}{\mathrm{d}s^2} \approx \frac{l(l+1)}{1+\beta}\frac{\Phi_{lm}}{s^2} + 2\left[\frac{\beta}{1+\beta}\left(\frac{\alpha}{s} + \frac{\beta_* s}{r_*^2\left(1+\frac{s^2}{r_*^2}\right)}\right) - \frac{1}{s}\right]\frac{\mathrm{d}\Phi_{lm}}{\mathrm{d}s}. \tag{5.35}$$

Again with the asymptotic solution of $\Phi_{lm}(s) \propto s^{\tilde{l}_2}$, the two roots of $\tilde{l}_2$ are

$$\begin{aligned} \tilde{l}_2 &= \frac{1}{2}\left[k + \sqrt{k^2 + \frac{4l(l+1)}{1+\beta}}\right], \\ k - \tilde{l}_2 &= \frac{1}{2}\left[k - \sqrt{k^2 + \frac{4l(l+1)}{1+\beta}}\right]. \end{aligned} \tag{5.36}$$

with

$$k = \frac{2\beta}{1+\beta}\left[\alpha + \frac{\beta_*}{\left(1+\left(\frac{S_{\mathrm{boun}}}{r_*}\right)^2\right)}\left(\frac{S_{\mathrm{boun}}}{r_*}\right)^2\right] - 1, \tag{5.37}$$

where S_{boun} is the survey boundary. As $\tilde{l}_2 > 0$ and $k - \tilde{l}_2 < 0$, for $\Phi_{lm}(s)$ to remain finite at large s, the appropriate asymptotic solution for the potential is

$$\Phi_{lm}(s) = C_2 s^{k-\tilde{l}_2}. \tag{5.38}$$

where C_2 is again a free parameter.

With the two asymptotic forms of $\Phi_{lm}(s)$, numerical computation was performed on equation (5.20) where C_1 and C_2 were allowed to vary freely. As in the case of the monopole and dipole potential, a multipole potential was then constructed on a 32^3 grid with a spacing of 400 km/s. l of up to 4 were used for the construction which was then added on to the monopole and dipole potential. This potential was then compared to that of POTENT constructed using the same l. Figure 5.6 shows the plot of Φ_{POTENT} against Φ_{ODE}. The spacing of every point in the figure again corresponds to 1200 km/s in any grid direction.

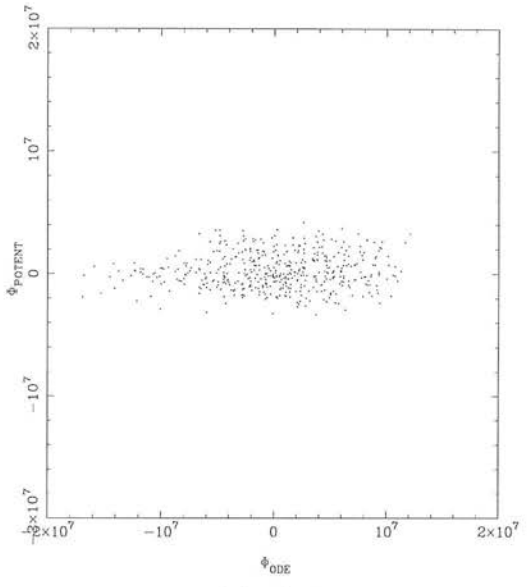

(a) β=0.1

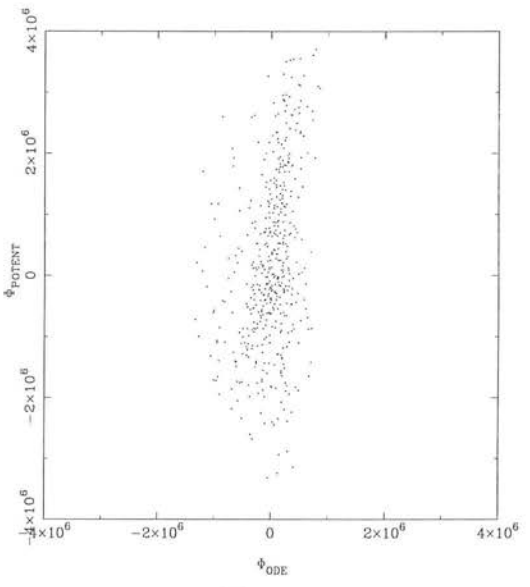

(b) β=0.5

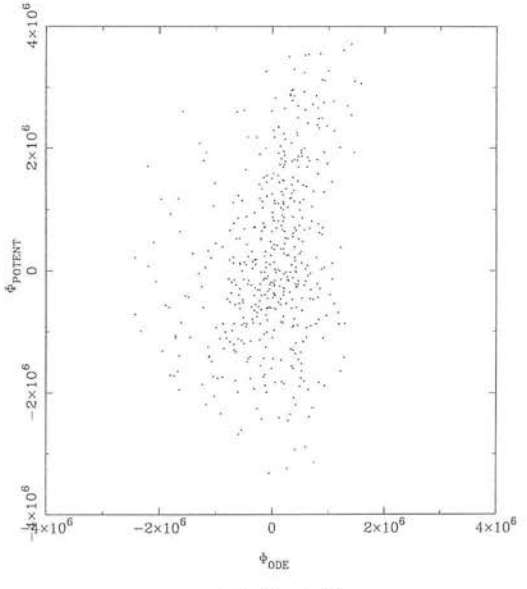

(c) β=1.0

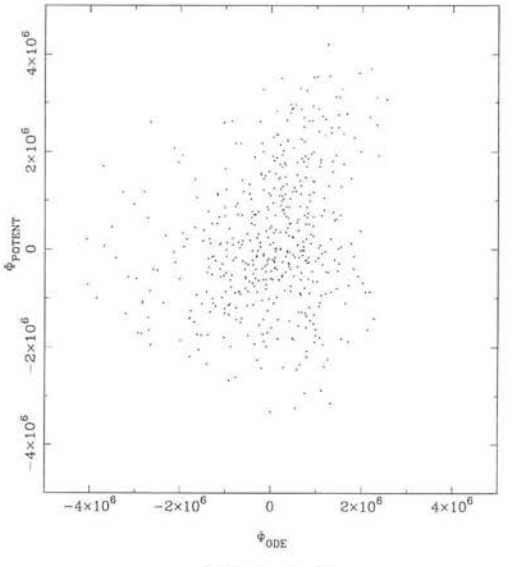

(d) β=2.0

Figure 5.6: Plot of POTENT velocity potential in the LG frame $\Phi_{\rm POTENT}$ against velocity potential obtained by O.D.E. ($\Phi_{\rm ODE}$) within a 6000 km/s radius for β of (a) 0.1, (b) 0.5, (c) 1.0 and (d) 2.0. l from 0 to 4 were used for the construction. Each comparison point has a spacing of 1200 km/s along any grid direction and the unit of the potential is in $(\mathrm{km/s})^2$.

5.7 Discussion

Most of the analysis in this chapter is based on the work of Nusser & Davis (1994). In their work, they deduced the value of β by matching the dipole velocity derived from the O.D.E. to that of POTENT. Here we have tried to match up the O.D.E. and POTENT potentials with different values of β. We also carry the work further by analysing $l > 1$ multipole potential. Our results suggest that the value of β must be much larger than unity for the dipole potentials to be consistent. For $l > 1$ multipole potential, our analysis was hindered by the lack of knowledge of the asymptotic solution and as such no conclusive value of β can be deduced here.

As figure 5.5 shows, there seems to be a strong correlation between $\Phi_{\rm ODE}$ and $\Phi_{\rm POTENT}$ with construction of $l = 0, 1$ coefficients. However with higher multipoles, such correlation disappears as figure 5.6 clearly shows. There could be a number of reasons for such a discrepancy. It might be that the asymptotic solution of the form $\Phi_{lm}(s) \propto s^{\tilde{l}}$ assumed was not appropriate at the boundary; or it could be that the 20,000 km/s boundary is not far enough for the asymptotic solution to be valid. Extending the boundary to a bigger value might seem like an obvious remedy, but the reliability of the $\delta^n_{0lm}(s)$ data decreases with increasing redshift. The filling of artificial galaxies in the galactic plane and the unobserved regions of sky could also render the $\delta^n_{0lm}(s)$ data unreliable. Also the optimisation of the selection function in section 5.3.1 does not take into the account of possible clustering of galaxies in redshift space. Without reliable $\delta^n_{0lm}(s)$ data at large redshift, it is difficult to determine which is the dominant cause for the discrepancy.

The difficulty with this approach is in the data itself. Any model testing requires proper account of the errors, and the POTENT data do not lend themselves to good error assessment. There may be biases in the potential determination (e.g. Newsam et al. 1995), and the errors in the potential will clearly not be independent, by the nature of the construction method used. Hence the results from this need to be treated cautiously until a proper error analysis can be done, almost certainly by Monte Carlo simulation.

The correlation between $\Phi_{\rm ODE}$ and $\Phi_{\rm POTENT}$ for the monopole and dipole terms

suggests that this method could be a promising way of determining β, if the higher multipole potential can be reliably constructed. As for the future prospect, a reliable deep full sky galaxy survey and perhaps a better measurement of the peculiar velocities will certainly aid this method to achieve its full potential. Hopefully, such prospect can be realised in future surveys.

Chapter 6

Final Remarks

In this the final chapter of my thesis, I shall first summarise the results of the thesis, and then give a brief overview of the current state of progress in cosmology that has both direct and indirect influence on the research work that I have presented in the previous chapters. From chapter 2 to 5, I have investigated a number of new methods of using galaxy and peculiar velocity data to estimate β. None of these methods has been used before, and I have tried to asses their advantages and disadvantages. Two of the methods (chapters 2 and 3) are promising and could potentially yield excellent constraints from good data. The methods of chapter 4 and 5 are probably not useful in their present form, for reasons outlined in the text.

In chapter 2, the preliminary conclusion is that it is possible to have a relatively stationary shell at 30 h^{-1} Mpc in a large ($\sim 60\ h^{-1}$ Mpc) bulk flow environment provided that $\beta \gtrsim 1$. However the peculiar velocity dataset is relatively old and not very large. It would be interesting to repeat the same analysis with a more extensive recent peculiar velocity compilations.

In the likelihood analysis of the redshift distortion in chapter 3, it is not possible to draw a firm conclusion on the value of β. This is probably due to some systematic errors in the catalogue or perhaps the effects of 'fingers of god' (e.g. de Lapparent et al. 1986; Wegner et al. 1993; Hamilton 1993b). The results are however consistent with any sensible value of β.

A high value of β is favoured from the comparison of the predicted and measured peculiar velocity potential in chapter 4. But the effect of redshift distortion was not taken into account and so any conclusion drawn here is possibly unreliable.

In the multipole analysis of chapter 5, the monopole and dipole velocity predicted from the galaxy sample seems to favour a high value of β. This method does not give an error on the estimated β and so any discussion of its value might be premature.

Putting them altogether, it seems that a high value of β would be the favoured option. It is however unwise to jump to such a conclusion as the current data are not extensive enough to give a really good, reliable result. The thesis presents some of the techniques that could be employed when better dataset is obtained. Hopefully the improvement on the data will be realised in the next generation surveys. Examples of some of the important future surveys include Sloan Digital Sky Survey and 2dF. The CCD photometric survey of Sloan will cover π steradians in the northern Galactic gap and produce images in five bands to limiting magnitudes of order 23 (Gunn & Weinberg 1995). It will obtain redshifts of 10^6 galaxies and 10^5 quasars. The 2dF uses a new and powerful 400-fibre spectroscopic survey facility and is capable of producing aberration-corrected images over a 2° field of view (Taylor 1995). It should provide the AAT (Anglo-Australian Telescope) with a new and important role for large-scale statistical studies into the early 21^{st} century.

The study of the large-scale motions of the universe is a big subject in itself but by no means does it represent the whole picture of cosmology. There are other fields in cosmology too that are currently commanding a huge research interest and effort: the study of microwave background radiation, gravitational lensing, quantum cosmology, evolution of galaxies, structure formation theory, etc to name just a few.

Cosmology used to be a data-starved science. This situation has been greatly reversed by the recent improvement of the quality and quantity of our telescopic observations, both ground and space-based. Nevertheless there is certainly still plenty of room for improvement in our data gathering. Sometime it is the quality and not the quantity of data that we are starved of. A good example is the true distances from us to all other galaxies. The current redshift data are reasonably sufficient for us to make some

sense out of the region a few hundred Mpc around us but they are not complemented well by any accurate measurement of the redshift-independent distances. This distance measurement is crucial in getting the peculiar velocity of galaxies. Today the distance measurements of distant galaxies still rely mainly on the Infrared Tully-Fisher method for spirals and $D_n - \sigma$ for ellipticals but these methods yield relatively high errors on the result. The problem of distance measurement lies in the difficulty of calibrating the relative distances for distant galaxies to the direct distance estimates of the nearby galaxies. Relative distances of galaxies are usually calibrated to the Virgo cluster of galaxies. What one then needs is to know the distance to the Virgo cluster. Currently the best direct measurement of distance is done by observing Cepheid stars, whose luminosity fluctuation period indicates their intrinsic luminosity. Resolving and measuring light of individual star in the Virgo cluster are difficult with ground-based telescope, but the task becomes possible with the Hubble Space Telescope (HST).

If we know the physical size of distant galaxies, then the angle they subtended in observation will also give a direct distance estimate. However we cannot trust our measurement to such an ideal situation given that we still do not have a complete knowledge of the galactic evolution. In fact, given that almost all classes of astronomical objects show at least some form of evolution with time, it would be surprising that the intrinsic properties of the galaxies should remain unchanged with their distances from the observer. A more promising way of distance measurement comes recently from the argument of the existence of "standard candles" in distant galaxies. The standard candles concerned here are the Type Ia supernovae (Branch & Tamman 1992) whose high luminosity makes them very attractive for such a task in the foreseeable future.

The importance of accurate distance measurement is not merely confined in the study of peculiar motion. The determination of the Hubble constant, and thus the age of the universe, also depends on it. Armed with the true distance to every observed galaxy, the cosmological principle of homogeneity and isotropy too can be scrutinised. Its importance in cosmology cannot be overstated. It is unfortunate and frustrating that such an important measurement is so elusive and hard to obtain at present.

Cosmology has progressed a long way since its practical inception at the turn of

this century, but today there are still many unanswered questions. Some of the most important foundation principles in this field have yet to be resolved. For example, the principle of homogeneity and isotropy was first proposed because of its simplicity that we can have with the Robertson-Walker metric. While isotropy is strongly demonstrated in the CMBR, there is still no definite observational proof yet of the principle of homogeneity. Another controversial issue that is currently under debate is the value of Hubble constant, though the range of disagreement should get narrow and narrower as the distance measurements improve in the future. As for the density parameter Ω_0, there is still a big question of whether our universe is open, flat or closed. Baryonic observations give a contribution to Ω_0 in the region of around 0.05, but the inflation theory and density evolution argument (section 1.8.3) favour a value of unity. This prompted the suggestion of the existence of dark matter which makes up the bulk of the universe. It is doubtful whether we really need a flat (or indeed open or closed) universe; and if dark matter does exist, what form does it take? Could it be in the form of black holes, weakly interacting massive particles (WIMP) like neutrinos, massive compact halo objects (MACHO) such as brown dwarfs, or the combination of all of them? Then there is also the question of biasing between light and matter. Most cosmologists nowadays assume a simple scale invariant bias parameter b because of the appeal of simplicity and yet to date there is still no direct evidence for such assumption. In fact the linear bias model must break down in the nonlinear regime (see discussion in section 4.1 of Hamilton 1997). Various models of nonlinear biasing have also been contemplated (Fry & Gaztañaga 1993; Mann et al. 1997). This is an important issue because our theory of structure formation is based on gravitational interaction of mass but our observation of galaxy count is based on the detection of light. Another parameter that can be of immense importance (or none at all!) is the cosmological constant Λ. The current upper limit on Λ is in the order of $10^{-38}\mathrm{m}^{-2}$ (section 1.8) but it remains to be seen whether it is truly zero as many cosmologists have assumed.

Even when the issues above are resolved, we still have to tackle the theory of structure formation. What gave birth to the seeds of mass perturbation in the first place? Were they caused by some topological defects such as cosmic strings or domain walls? Or can inflation theory provide all the answers to the origin of structure formation? To get an

answer to all these questions, we will probably have to understand (and speculate) the physics of the universe prior to the Planck epoch. So far I have highlighted some of the most important issues in cosmology. There are certainly many other similar problems that need to be solved which I shall not get into the detail of. For cosmology to be a science subject with credibility, all these issues must be addressed and tackled with.

It is remarkable that during the billions of years of history of the universe, we should be living in such a narrow time window where some of the most important discoveries of cosmology actually unfolded in front of our eyes. It started off with the discovery of Hubble expansion in the 1920s and the CMBR during the 1960s. And during my lifetime, one has to feel extremely fortunate to have witnessed many unforgettable events such as the supernova in 1987, the detection of COBE anisotropies in 1992, and recently of the HST deep field images of galaxies. It is also during my lifetime that many of the space telescopes that changed the face of cosmology such as the IRAS (without which this thesis would not exist), COBE, HST, etc were launched. With hope, there might still be many more unforgettable events that are going to happen in my remaining life.

Although there are many other areas of specific topics in cosmology beside the study of large-scale motions. Ultimately they are all aiming at one goal: to explain how all the structures and life in our universe came about. Undoubtedly there are still many hurdles to cross before we can find the answer. As yet many fundamental issues in cosmology still need our relentless effort to solve. But with an optimistic view, perhaps our effort could be rewarded one day!

References

Abbreviation

A&A = Astronomy And Astrophysics

ARA&A = Annual Review of Astronomical Astrophysics

ApJ = The Astrophysical Journal

ApJS = The Astrophysical Journal Supplement Series

Astron. J. = Astronomical Journal

MNRAS = Monthly Notices of the Royal Astronomical Society

Phys.Lett = Physical Letters

Aaronson M., Huchra J., Mould J., 1979, ApJ, 229, 1

Aaronson M., Bothun G.D., Cornell M.E., Dawe J.A., Dickens R.J., Hall P.J., Han Ming Sheng, Huchra J.P., Lucey J.R., Mould J.R., Murray J.D., Schommer R.A., Wright A.E., 1989, ApJ, 338, 654

Abramowitz M., Stegun I.A., 1970, Handbook of Mathematical Functions, Dover Publication, New York

Ballinger W.E., Heavens A.F., Taylor A.N., 1995, MNRAS, 276, L59

Banday A.J. et al., 1994, ApJ, 439, 99

Bertschinger E., 1991, in Martinez V.S., Portilla M., Saez D., eds., New Insights into the Universe. Springer-Verlag, Berlin, p.65

Bertschinger E., Dekel A., 1989, ApJ, 336, L5

Binney J., Quinn T., 1991, MNRAS, 249, 678

Binney J., Tremaine S., 1987, Galactic Dynamics, Princeton University Press

Branch D., Tamman G.A., 1992, ARA&A, 30, 359

Calzetti D., Giavalisco M., 1993, ApJ, 406, 338

Cole S., Fisher K.B., Weinberg D.H., 1994, MNRAS, 267, 785

Coles P., 1993, MNRAS, 262, 1065

de Lapparent V., Geller M.J., Huchra J.P., 1986, ApJ, 302, L1

de Vaucouleurs G., 1948, Ann. d'Astrophys., 11, 247

de Vaucouleurs G., Pence W.D., 1978, Astron. J., 83, 1163

Dekel A., 1986, Comments on Astrophysics, 11, 235

Dekel A., 1994, ARA&A, 32, 371

Dekel A., Bertschinger E., Faber S.M., 1990, ApJ, 364, 349 (DBF)

Dekel A., Bertschinger E., Yahil A., Strauss M.A., Davis M., Huchra J.P., 1993, ApJ, 412, 1

Djorgovski S., Davies M., 1987, ApJ, 313, 59

Dressler A., Faber S.M., Burstein D., Davies R.L., Lynden-Bell D., Terlevich R.J., Wegner G., 1987a, ApJ, 313, 42

Dressler A., Faber S.M., Burstein D., Davies R.L., Lynden-Bell D., Terlevich R.J., Wegner G., 1987b, ApJ, 313, L37

Efstathiou G., Bond J.R., White S.D.M., 1992, MNRAS, 258, 1

Fisher K.B., Scharf C.A., Lahav O., 1994a, MNRAS, 266, 219

Fisher K.B., Davis M., Strauss M.A., Yahil A., Huchra J.P., 1994b, MNRAS, 267, 927

Fisher K.B., Huchra J.P., Strauss M.A., Davies M., Yahil A., Schlegel D., 1995a, ApJS, 100, 69

Fisher K.B., Lahav O., Hoffman Y., Lynden-Bell D., Zaroubi S., 1995b, MNRAS, 272, 885

Fry J.N., Gaztañaga E., 1993, ApJ, 413, 447

Gunn J., Weinberg D., 1995, Wide Field Spectroscopy And The Distant Universe, proc. 35th Herstmonceux conference, eds Maddox S.J. & Aragán-Salamanca A., World Scientific, p3

Hamilton A.J.S., 1993a, ApJ, 406, L47

Hamilton A.J.S., 1993b, ApJ, 417, 19

Hamilton A.J.S., 1997, Linear Redshift Distortions: A Review, to appear in Proceedings Ringberg Workshop on Large-Scale Structure, held at Ringberg Castle, Germany, September 1996, Kluwer Academic, Dordrecht, (astro-ph/9708102)

Hatton S.J., Cole S., 1997, Modelling the Redshift-Space Distortion of Galaxy Clustering, MNRAS, submitted (astro-ph/9707186)

Heavens A.F., Taylor A.N., 1995, MNRAS, 275, 483

Hubble E.P., 1930, ApJ., 71, 231

Hudson M.J., 1994, MNRAS, 266, 475

Hudson M.J., Dekel A., Courteau S., Faber S.M., Willick J.A., 1995, MNRAS, 274, 305

Islam J.N., 1983, Phys.Lett, 97A, 239

Islam J.N., 1992, An Introduction To Mathematical Cosmology, Cambridge University Press

Kaiser N., 1987, MNRAS, 227, 1

Kaiser N., 1988, MNRAS, 231, 149

Kaiser N., Lahav O., 1987, in Rubin V.C., Coyne G.V., eds., Large Scale Motions in the Universe. Princeton University Press, Princeton, p.339

Kaiser N., Efstathiou G., Ellis R., Frenk C., Lawrence A., Rowan-Robinson M., Saunders W., 1991, MNRAS, 252, 1

Kirshner R.P., Oemler A., Schechter P.L., Shectman S.A., 1983, Astron. J., 88, 1285

Kogut A., Banday A.J., Bennet, C.L., Górski K.M., Hinshaw G., Smoot G.F., Wright E.L., 1996, ApJ, 464, L29

Kolb E.W., Turner M.S., 1990, The Early Universe, Addison Wesley

Kormendy J., 1977, ApJ., 218, 333

Lahav O., 1993, in Bouchet F.R., Lachiéze-Rey M., eds, Proc. 9th IAP Conference, Cosmic Velocity Fields, Editions Frontiéres, Gif-sur-Yvette, p.205

Loke H.Y., Heavens A.F., 1996, MNRAS, 279, 1303

Lynden-Bell D., Faber S.M., Burstein D., Davies R.L., Dressler A., Terlevich R.J., Wagner G., 1988, ApJ, 326, 19

Madsen M., Ellis G.F.R., 1988, MNRAS, 234, 67

Mann R.G., Peacock J.A., Heavens A.F., 1997, Eulerian Bias and the Galaxy Density Field, MNRAS, in press (astro-ph/9702228)

Martin-Mirones J.M., Goicoechea L.J., 1992, A&A, 253, 3 (MMG)

Mather J.C., Cheng E.S., Cottingham D.A. et al., 1994, ApJ, 420, 439

Mathews J., Walker R.L., 1970, Mathematical Methods of Physics, Addison Wesley World Student Series

Mathewson D., Ford V.L., Buchhorn M., 1992, ApJS, 81, 413

Newsam A., Simmons J.F.L., Hendry M.A., 1995, A&A, 294, 627

Nusser A., Davis M., 1994, ApJ, 421, L1

Padmanabhan T., 1993, Structure Formation In The Universe, Cambridge University Press

Peacock J.A., 1991, MNRAS, 253, 1p

Peacock J.A., 1992, MNRAS, 258, 581

Peacock J.A., Dodds S.J., 1994, MNRAS, 267, 1020

Peebles P.J.E., 1980, The Large-Scale Structure of the Universe, Princeton University Press, Chapter II

Press W.H., Teukolsky S.A., Vetterling W.T., Flannery B.P., 1992, Numerical Recipes in Fortran The Art of Scientific Computing, Second Edition, Cambridge University Press

Rees M.J., 1985, MNRAS, 213, 75P

Reynolds J.H., 1913, MNRAS, 74, 132

Roos M., 1994, Introduction to Cosmology, John Wiley & Sons

Scharf C.A., Hoffman Y., Lahav O., Lynden-Bell D., 1992, MNRAS, 256, 229

Scharf C.A., Lahav O., 1993, MNRAS, 264, 439

Shaya E.J., Peebles P.J.E., Tully R.B., 1995, ApJ, 454, 15

Sigad Y., Eldar A., Dekel A., Strauss M.A., Yahil A., 1997, in press (astro-ph/9708141)

Stirling A.J., Peacock J.A., 1996, MNRAS, 283, L99

Strauss M.A., 1989, PhD thesis, University of California, Berkeley

Strauss M.A., Willick J.A., 1995, Physics Reports, 261, 271

Taylor A.N., Rowan-Robinson M, 1993, MNRAS, 265, 809

Taylor K., 1995, Wide Field Spectroscopy And The Distant Universe, proc. 35th Herstmonceux conference, eds Maddox S.J. & Aragán-Salamanca A., World Scientific, p15

Tully R.B., Fisher J.R., 1977, A&A, 54, 661

Tytler D., Fan Xiao-Ming, Burles S., 1996, Nature, 381, 207

Webster M., Lahav O., Fisher K., 1997, MNRAS, submitted

Wegner G., Haynes M.P., Giovanelli R., 1993, Astron. J., 105, 1251

Willick J.A., Strauss M.A., Dekel A., Kolatt T., 1997, ApJ, in press (astro-ph/9612240)

Zaroubi S., Hoffman Y., 1996, ApJ, 462, 25

Zel'dovich Ya.B., 1970, A&A, 5, 84

Appendix A

Transform and Inverse of Spherical Bessel Harmonics

In the context of the continuous Spherical Bessel harmonics, one can define a scalar quantity $G(\mathbf{r})$ and its transform $G_{lm}(k)$ by

$$G(\mathbf{r}) = C\sum_{lm}\int G_{lm}(k)j_l(kr)Y_{lm}(\theta,\phi)k^2\mathrm{d}k \tag{A.1}$$

$$G_{lm}(k) = C\int G(\mathbf{r})j_l(kr)Y^*_{lm}(\theta,\phi)\mathrm{d}^3\mathbf{r}, \tag{A.2}$$

where the normalisation C in this case has been chosen to be symmetrical (the choice is arbitrary). Expanding $G(\mathbf{r})$ in the integral of equation (A.2), we have

$$G_{lm}(k) = C^2\sum_{l'm'}\int G_{l'm'}(k')j_l(kr)j_{l'}(k'r) \\ Y^*_{lm}Y_{l'm'}r^2\mathrm{d}rk'^2\mathrm{d}k'\mathrm{d}\Omega. \tag{A.3}$$

Using

$$\int j_l(kr)j_{l'}(k'r)Y^*_{lm}Y_{l'm'}r^2\mathrm{d}r\mathrm{d}\Omega = \frac{\pi}{2kk'}\delta^{\mathrm{D}}(k-k')\delta^{\mathrm{K}}_{ll'}\delta^{\mathrm{K}}_{mm'}, \tag{A.4}$$

where $\delta^{\mathrm{D}}(k-k')$ and $\delta^{\mathrm{K}}_{ll'}$ are the Dirac and Kronecker delta functions respectively, equation (A.3) is then

$$\begin{aligned} G_{lm}(k) &= C^2 \int G_{lm}(k') \frac{\pi}{2kk'} \delta^{\mathrm{D}}(k-k') k'^2 \mathrm{d}k' \\ &= \frac{\pi}{2} C^2 G_{lm}(k). \end{aligned} \tag{A.5}$$

Thus the symmetrical normalisation is $C = \sqrt{2/\pi}$.

Appendix B

Velocity and Density Fields

If a velocity field $\mathbf{v}(\mathbf{r})$ is curl free, then one can define a scalar potential $\Phi(\mathbf{r})$ such that $\mathbf{v}(\mathbf{r}) \equiv -\nabla\Phi(\mathbf{r})$. Expanding $\Phi(\mathbf{r})$ in terms of $\Phi_{lm}(k)$ as in equation (3.2),

$$\begin{aligned}\mathbf{v}(\mathbf{r}) &= -\sqrt{\frac{2}{\pi}}\sum_{lm}\int \Phi_{lm}(k) \\ &\quad\times\left(\frac{\mathrm{d}}{\mathrm{d}r}j_l(kr)Y_{lm}, \frac{j_l(kr)}{r}\frac{\partial Y_{lm}}{\partial\theta}, \frac{j_l(kr)}{r\sin\theta}\frac{\partial Y_{lm}}{\partial\phi}\right)k^2\mathrm{d}k. \qquad \text{(B.1)}\end{aligned}$$

So the radial part of the peculiar velocity $u \equiv s - r = \mathbf{v}.\hat{\mathbf{r}}$ is

$$u = -\sqrt{\frac{2}{\pi}}\sum_{lm}\int \Phi_{lm}(k)\frac{\mathrm{d}}{\mathrm{d}r}j_l(kr)Y_{lm}(\theta,\phi)k^2\mathrm{d}k. \qquad \text{(B.2)}$$

The relationship between $\Phi_{lm}(k)$ and $\delta_{lm}(k)$ can be explored using the Poisson equation:

$$\begin{aligned}\delta(\mathbf{r}) &= \frac{1}{\beta}\nabla^2\Phi(\mathrm{r}) \\ &= \sqrt{\frac{2}{\pi}}\sum_{lm}\int \Phi_{lm}(k)\left[\frac{1}{r^2}\frac{\partial}{\partial r}\left(r^2\frac{\partial j_l(kr)}{\partial r}\right)Y_{lm}\right. \\ &\quad+\frac{1}{r^2\sin\theta}\frac{\partial}{\partial\theta}\left(\sin\theta\frac{\partial Y_{lm}}{\partial\theta}\right)j_l(kr) \\ &\quad\left.+\frac{1}{r^2\sin^2\theta}\frac{\partial^2 Y_{lm}}{\partial\phi^2}j_l(kr)\right]k^2\mathrm{d}k. \qquad \text{(B.3)}\end{aligned}$$

The derivatives can be expressed as

$$\frac{1}{r^2}\frac{\partial}{\partial r}\left(r^2\frac{\partial j_l(kr)}{\partial r}\right) = \left[l(l+1) - k^2r^2\right]\frac{j_l(kr)}{r^2}, \qquad \text{(B.4)}$$

and

$$\frac{1}{\sin\theta}\frac{\partial}{\partial\theta}\left(\sin\theta\frac{\partial Y_{lm}}{\partial\theta}\right)+\frac{1}{\sin^2\theta}\frac{\partial^2 Y_{lm}}{\partial\phi^2}=-l(l+1)Y_{lm}. \tag{B.5}$$

Thus

$$\delta(\mathbf{r})=-\frac{1}{\beta}\sqrt{\frac{2}{\pi}}\sum_{lm}\int\Phi_{lm}(k)j_l(kr)Y_{lm}(\theta,\phi)k^4\mathrm{d}k. \tag{B.6}$$

Comparison of equation (B.6) and the definition of $\delta_{lm}(k)$ (Appendix A) gives

$$\delta_{lm}(k)=-\frac{1}{\beta}\Phi_{lm}(k)k^2. \tag{B.7}$$

Hence

$$u=\beta\sqrt{\frac{2}{\pi}}\sum_{lm}\int\delta_{lm}(k)\frac{\mathrm{d}j_l(kr)}{\mathrm{d}r}Y_{lm}(\theta,\phi)\mathrm{d}k. \tag{B.8}$$

Appendix C

Power Spectrum

In this appendix, the relationship between $\langle \delta_{lm}(k)\delta^*_{l'm'}(k')\rangle$ and the power spectrum $P(k)$ defined in the context of Fourier transform $\langle \delta_{\mathbf{k}}\delta^*_{\mathbf{k}'}\rangle \equiv P(k)\delta^{\mathrm{D}}(\mathrm{k}-\mathrm{k}')$ is established. Our $\delta_{\mathbf{k}}$ is defined in such a way that:

$$\begin{aligned}\delta(\mathbf{r}) &= \frac{1}{(2\pi)^{3/2}}\int \delta_{\mathbf{k}} \mathrm{e}^{i\mathbf{k}.\mathbf{r}}\mathrm{d}^3\mathbf{k} \\ &= \sqrt{\frac{2}{\pi}}\int \delta_{\bar{\mathbf{k}}}\sum_{\bar{l}\bar{m}} i^{\bar{l}} j_{\bar{l}}(\bar{k}r) \\ &\qquad \times Y_{\bar{l}\bar{m}}(\bar{\theta},\bar{\phi})Y_{\bar{l}-\bar{m}}(\theta,\phi)\bar{k}^2\mathrm{d}\bar{k}\mathrm{d}\bar{\Omega}, \end{aligned} \tag{C.1}$$

where we have used $\exp(i\bar{\mathbf{k}}.\mathbf{r}) = 4\pi\sum_{lm} i^l j_l(\bar{k}r)Y_{lm}(\bar{\theta},\bar{\phi})Y_{l-m}(\theta,\phi)$. With equation (C.1), $\delta_{lm}(k)$ is then

$$\begin{aligned}\delta_{lm}(k) &= \frac{2}{\pi}\int \delta_{\bar{\mathbf{k}}}\sum_{\bar{l}\bar{m}} i^{\bar{l}} j_{\bar{l}}(\bar{k}r)Y_{\bar{l}\bar{m}}(\bar{\theta},\bar{\phi})Y_{\bar{l}-\bar{m}}(\theta,\phi) \\ &\qquad \times j_l(kr)Y^*_{lm}(\theta,\phi)\bar{k}^2\mathrm{d}\bar{k}\mathrm{d}\bar{\Omega}\mathrm{d}^3\mathbf{r}. \end{aligned} \tag{C.2}$$

Using equation (A.4) and integrating over $\mathbf{r}$:

$$\delta_{lm}(k) = i^l\int \delta_{\bar{\mathbf{k}}}Y_{l-m}(\bar{\theta},\bar{\phi})\delta^{\mathrm{D}}(k-\bar{k})\mathrm{d}\bar{k}\mathrm{d}\bar{\Omega}. \tag{C.3}$$

Since $Y_{l-m} = Y^*_{lm}$,

$$\begin{aligned}\langle \delta_{lm}(k)\delta^*_{l'm'}(k')\rangle &= i^{l-l'}\int \langle \delta_{\bar{k}}\delta^*_{\bar{\bar{k}}}\rangle Y^*_{lm}(\bar{\theta},\bar{\phi})Y_{l'm'}(\bar{\bar{\theta}},\bar{\bar{\phi}}) \\ &\qquad \times\delta^{\mathrm{D}}(k-\bar{k})\delta^{\mathrm{D}}(k'-\bar{\bar{k}})\mathrm{d}\bar{k}\mathrm{d}\bar{\bar{k}}\mathrm{d}\bar{\Omega}\mathrm{d}\bar{\bar{\Omega}}. \end{aligned} \tag{C.4}$$

Using the definition of the power spectrum:

$$\langle \delta_{\bar{k}} \delta^*_{\bar{\bar{k}}} \rangle = P(k) \delta^{\mathrm{D}}(\bar{\mathbf{k}} - \bar{\bar{\mathbf{k}}}) \tag{C.5}$$

with

$$\delta^{\mathrm{D}}(\bar{\mathbf{k}} - \bar{\bar{\mathbf{k}}}) = \frac{\delta^{\mathrm{D}}(\bar{k} - \bar{\bar{k}}) \delta^{\mathrm{D}}(\cos\bar{\theta} - \cos\bar{\bar{\theta}}) \delta^{\mathrm{D}}(\bar{\phi} - \bar{\bar{\phi}})}{\bar{k}^2} \tag{C.6}$$

and

$$\int Y^*_{lm}(\theta, \phi) Y_{l'm'}(\theta, \phi) \mathrm{d}\Omega = \delta^{\mathrm{K}}_{ll'} \delta^{\mathrm{K}}_{mm'}, \tag{C.7}$$

equation (C.4) now becomes

$$\begin{aligned} \langle \delta_{lm}(k) \delta^*_{l'm'}(k') \rangle &= \int \frac{P(\bar{k})}{\bar{k}^2} \delta^{\mathrm{D}}(k - \bar{k}) \\ &\quad \times \delta^{\mathrm{D}}(k' - \bar{k}) \delta^{\mathrm{K}}_{ll'} \delta^{\mathrm{K}}_{mm'} \mathrm{d}\bar{k} \\ &= P(k) \frac{\delta^{\mathrm{D}}(k - k')}{k^2} \delta^{\mathrm{K}}_{ll'} \delta^{\mathrm{K}}_{mm'}. \end{aligned} \tag{C.8}$$

Appendix D

Shot Noise of the Covariance Matrix

Here, the shot noise for the covariance matrix $\langle D_\mu D_\nu \rangle$ of equation (3.24) associated with using the discrete galactic positions is derived.

We start off with $\rho_{lm}(k)$ from the discrete sum of N galaxies (see equation (3.17)):

$$\rho_{lm}(k) \equiv \sqrt{\frac{2}{\pi}} \sum_{n=1}^{N} w(r_n) j_l(kr_n) Y_{lm}^*(\theta_n, \phi_n). \tag{D.1}$$

By splitting the universe into many small cells, the discrete galactic sum can be rewritten as

$$\rho_{lm}(k) = \sqrt{\frac{2}{\pi}} \sum_{i=1} n_i w(r_i) j_l(kr_i) Y_{lm}^*(\theta_i, \phi_i), \tag{D.2}$$

where the sum is now over every cell with n_i being either 0 or 1 depending on whether a galaxy is contained in that cell or not. By approximating the discrete sum to a proper integral, the mean value of $\rho_{lm}(k)$ is then

$$\langle \rho_{lm}(k) \rangle = \sqrt{\frac{2}{\pi}} \int \rho_0(\mathbf{r}) w(r) j_l(kr) Y_{lm}^*(\theta, \phi) \mathrm{d}^3\mathbf{r}, \tag{D.3}$$

where $\rho_0(\mathbf{r})$ is the selection function which can be written

$$\rho_0(\mathbf{r}) = \rho_0(r) M(\Omega) \tag{D.4}$$

to incorporate the angular masking $M(\Omega)$ which has a value of 0 in a masked region and 1 otherwise.

The ensemble average $\langle \rho_{lm}(k)\rho_{l'm'}(k')\rangle$ is

$$\begin{aligned}\langle \rho_{lm}(k)\rho_{l'm'}(k')\rangle &= \frac{2}{\pi}\sum_i\sum_j \langle n_i n_j w_i w_j j_l(kr_i) j_{l'}(k'r_j) Y^*_{lm}(\Omega_i) Y^*_{l'm'}(\Omega_j)\\ &= \frac{2}{\pi}\sum_i \langle n_i\rangle w_i^2 j_l(kr_i) j_{l'}(k'r_i) Y^*_{lm}(\Omega_i) Y^*_{l'm'}(\Omega_i)\\ &\quad + \frac{2}{\pi}\sum_i\sum_{j\neq i} \langle n_i n_j\rangle w_i w_j j_l(kr_i) j_{l'}(k'r_j) Y^*_{lm}(\Omega_i) Y^*_{l'm'}(\Omega_j). \end{aligned} \tag{D.5}$$

In the small volume limit, equation (D.5) becomes

$$\begin{aligned}\langle \rho_{lm}(k)\rho_{l'm'}(k')\rangle &= \frac{2}{\pi}\int \rho_0(\mathbf{r}) w^2(r) j_l(kr) j_{l'}(k'r) Y^*_{lm}(\Omega) Y^*_{l'm'}(\Omega) \mathrm{d}^3\mathbf{r}\\ &\quad + \langle \rho_{lm}(k)\rangle\langle \rho_{l'm'}(k')\rangle. \end{aligned} \tag{D.6}$$

Hence the shot noise defined by $\rho_{\mathrm{SN}} \equiv \langle \rho_{lm}(k)\rho_{l'm'}(k')\rangle - \langle \rho_{lm}(k)\rangle\langle \rho_{l'm'}(k')\rangle$ is then

$$\begin{aligned}\rho_{\mathrm{SN}} &= \frac{2}{\pi}\int \rho_0(r) w^2(r) j_l(kr) j_{l'}(k'r) r^2 \mathrm{d}r\\ &\quad \times \int Y^*_{lm}(\Omega) M(\Omega) Y^*_{l'm'}(\Omega) \mathrm{d}\Omega. \end{aligned} \tag{D.7}$$

Mon. Not. R. Astron. Soc. 279, 1303–1309 (1996)

The correlation between bulk and shell velocities in cosmology

H.Y. Loke and A.F. Heavens

Institute for Astronomy, University of Edinburgh, Royal Observatory, Blackford Hill, Edinburgh EH9 3HJ

Accepted 1995 November 16. Received 1995 October 24; in original form 1995 August 29

ABSTRACT

Previous studies have shown that the bulk velocity of a sample of elliptical galaxies nearer than 60 h^{-1} Mpc is observed to be high (599 km s^{-1}), whereas the velocity of a shell of galaxies at a distance $\sim$30 h^{-1} Mpc is much smaller, 224 km s^{-1}, and consistent with shot noise only. We investigate the significance of the small ratio of these velocities in the context of Gaussian fluctuation theories for galaxy formation. We find that the shell and bulk velocities are significantly correlated for plausible power spectra, and the possibility of such a large discrepancy between them is small ($\sim$1.5 per cent). However, the probability rises to about 14 per cent since the shell at 30 h^{-1} Mpc is the most extreme of a sample of ten, and we conclude that the small ratio itself does not present a serious problem for the standard model of galaxy formation from gravitational instability of Gaussian fluctuations.

We also investigate the joint distribution of the shell speed and bulk speed, as this allows us to put constraints on the density parameter of the Universe. Using the power spectrum of *IRAS*-selected galaxies as a (possibly biased) indicator of the underlying mass power spectrum, we find acceptable solutions provided that $\Omega_0^{0.6}/b \gtrsim 1$, where b is the *IRAS* bias parameter.

Key words: cosmology: theory – dark matter – large-scale structure of Universe.

1 INTRODUCTION

If gravity is the cause of the peculiar velocities observed in the galaxy distribution, then in theory the observed peculiar velocity distribution can probe the underlying mass density distribution, namely the two-point correlation function $\xi(r)$ or the power spectrum $P(k)$. Using a catalogue of elliptical galaxies, Lynden-Bell et al. (1988) and Dressler et al. (1987) reported a bulk flow of 599 km s^{-1} towards l=312° ± 11°, b=6° ± 10° in the cosmic microwave background (CMB) frame for a sample up to a distance of 60 h^{-1} Mpc, where the Hubble constant is H_0=100 h km s^{-1} Mpc^{-1}. However, Martin-Mirones & Goicoechea (1992; hereafter MMG) reported that the shell at 30 h^{-1} Mpc is at rest in the CMB frame using the same elliptical galaxies catalogue (although their selection criteria differed from that of Lynden-Bell et al.). Motivated by this rather interesting question of whether these two results are in contradiction, Calzetti & Giavalisco (1993) attempted to reconcile these two results by using a double power-law fit for $1 + \xi(r)$, instead of the usual single power law for $\xi(r)$ itself.

Calzetti & Giavalisco claimed that, with the double power-law model, it is possible to have a bulk motion larger than the $\sim$500 km s^{-1} observed by Lynden-Bell et al. while the shell at 30 h^{-1} Mpc can have a velocity as low as $\sim$55 km s^{-1} in the CMB frame (Table 1). This is an interesting proposal, as the ratio of these quantities is (in the absence of noise) dependent only on the shape of the power spectrum, and not on its amplitude. Since the amplitude is free in most galaxy formation theories (even incorporating constraints from CMB fluctuations, if the density parameter is not fixed), the ratio could be a useful test. However, it turns out that shot noise

Table 1. MMG solution for the motion of the Local Group with respect to various shells. Rx stands for the shell centred at x h^{-1} Mpc with semi-width of 5 h^{-1} Mpc; N is the number of galaxies in each shell; α is the angle formed between $\Delta\boldsymbol{v} = (\Delta v_x, \Delta v_y, \Delta v_z)$ and the velocity they assumed for the Local Group with respect to the CMB: $\boldsymbol{v}_{LG}$ = (83, −504, 403) (Galactic coordinates and km s^{-1}). Note that the shell velocity in the CMB frame is independent of the $\boldsymbol{v}_{LG}$ assumed.

Shell	N	Δv	Δv_x	Δv_y	Δv_z	α	$\cos\alpha$
R10	23	160	39	111	-107	158°	-0.93
R15	42	363	-315	-165	72	68°	0.37
R20	57	532	-424	-310	82	63°	0.45
R25	43	519	-324	-316	255	46°	0.70
R30	33	570	94	-294	480	20°	0.94
R35	28	602	470	-52	372	57°	0.55
R40	29	651	424	-66	490	51°	0.63
R45	46	704	-173	-287	619	34°	0.83
R50	41	834	-311	-731	256	35°	0.82
R55	30	852	-90	-847	32	39°	0.78

(which was not considered by Calzetti & Giavalisco) is by no means negligible in current surveys, and this complicates the interpretation. In particular, the ratio is no longer independent of the power spectrum amplitude. In addition to the shot noise, one has to take account of the correlations between the two speeds.

With these two issues in mind, we calculate the joint probability distribution for the two velocities (including the shot noise error, which increases the expected variance), and quantify the probability of the existence of a near-stationary shell in the environment of a large bulk flow. In Section 3 the results of our calculations, using different power spectra, are presented and in Section 4 we discuss the implication of the results for the theory of large-scale structure formation. We find that, for the elliptical galaxy sample analysed by Lynden-Bell et al. (1988) and MMG, the probability of the ratio of the shell speed to the bulk speed being smaller than observed is ~1.5 per cent. This result looks significant, but the shell at 30 h^{-1} Mpc is the most extreme of the 10 shells examined by MMG. We therefore conclude that the ratio of the bulk and shell speeds does not present a serious challenge to the standard model of galaxy formation from Gaussian fluctuations.

When we consider the joint distribution of the two speeds, we find that models with low matter amplitude are more severely challenged. Obtaining the shape of the power spectrum from *IRAS* galaxy clustering studies, the large bulk flow solution is difficult to attain simultaneously with a small shell speed, unless $\beta \equiv \Omega_0^{0.6}/b$ is at least unity, where b is the *IRAS* bias parameter.

2 METHOD

2.1 Maximum likelihood method for the bulk and the shell velocities

The interpretation of joint bulk and shell velocities requires knowledge of the correlation between them. In this section, we derive expressions for bulk and shell velocities in terms of Fourier coefficients of the overdensity field, δ_k. This allows us to calculate explicitly the joint distribution of bulk and shell velocities.

The bulk and the shell velocities are determined by maximizing the likelihood function (see MMG):

$$\ln \mathscr{L} = \ln \left\{ \frac{1}{(2\pi)^{N/2} \parallel C_{ij} \parallel^{1/2}} \exp \left[-\sum_{i=1}^{N} \frac{(\boldsymbol{u}\cdot\hat{\boldsymbol{r}}_i - v_i)^2}{2\sigma_i^2} \right] \right\} \quad (1)$$

where v_i is the radial component of the peculiar velocity of the ith galaxy, N is the total number of galaxies or objects, $\sigma_i^2 = \sigma_z^2 + \sigma_{di}^2$ where σ_z and σ_{di} are the dispersions of the measured redshift z and the distance d respectively. i is the label for each galaxy or object, $C_{ij} = \mathrm{diag}(\sigma_i^2)$, $\hat{\boldsymbol{r}}_i$ is the unit radial vector of the ith object and $\boldsymbol{u}$ is the relevant shell or bulk velocity we are trying to obtain. In the case of the bulk sample of Lynden-Bell et al. (1988), σ_z=365 km s^{-1} and $\sigma_{di}^2 = \Delta^2 d^2$ where Δ=0.21. In the case of the shell sample, MMG used σ_z ranging from 250 to 400 km s^{-1} depending on which shell is concerned and they used a 'mean' dispersion of $\sigma_i^2 = \sigma_z^2 + \Delta^2(R_{\rm inn} + R_{\rm out})^2/4$ where $R_{\rm inn}$ and $R_{\rm out}$ are the inner and outer radii of the shell. Minimizing equation (1) by $\partial \ln \mathscr{L}/\partial u^\alpha = 0$ (where α=1,2,3) gives:

$$\sum_{i=1}^{N} \frac{u^\beta \hat{r}^\beta \hat{r}^\alpha}{\sigma_i^2} = \sum_{i=1}^{N} \frac{v_i \hat{r}^\alpha}{\sigma_i^2}. \quad (2)$$

Replacing the discrete sum by the integral with the appropriate selection function $\phi(r)$ and using $v_i = \boldsymbol{v}\cdot\hat{\boldsymbol{r}}_i$, $\boldsymbol{u}$ is then (assuming uniform sky coverage – see Kaiser (1988) for the general case)

$$u^\alpha = 3 \int (\boldsymbol{v}\cdot\hat{\boldsymbol{r}})\hat{r}^\alpha W(r) \mathrm{d}^3\boldsymbol{r} \quad (3)$$

where

$$W(r) \equiv \frac{\phi(r)}{\sigma^2(r) \int \frac{\phi(r')}{\sigma^2(r')} \mathrm{d}^3\boldsymbol{r}'}. \quad (4)$$

The selection function was obtained from Lynden-Bell et al. (1988) and MMG. With a Fourier expansion for $\boldsymbol{v}(\boldsymbol{r}) = \int \boldsymbol{v}(\boldsymbol{k}) \mathrm{e}^{\mathrm{i}\boldsymbol{k}\cdot\boldsymbol{r}} \mathrm{d}^3\boldsymbol{k}$, equation (3) can be written:

$$u^\alpha = 12\pi \int\int W(r) r^2 j_2(kr) v^\alpha(\boldsymbol{k}) \mathrm{d}r \mathrm{d}^3\boldsymbol{k} \quad (5)$$

where $2j_2(kr) = \int_{-1}^{+1} \mu^2 \mathrm{e}^{\mathrm{i}kr\mu} \mathrm{d}\mu$. In proper units, $\boldsymbol{v}(\boldsymbol{k}) = \mathrm{i}fH\frac{\boldsymbol{k}}{k^2}\delta_k$ (Peebles 1980), where $f \simeq \Omega_0^{0.6}$, H is the Hubble constant and δ_k refers to the mass density fluctuation in k space. The result of all these is to give

$$u^\alpha = \mathrm{i}fH \int W(k) \hat{k}^\alpha \delta_k \mathrm{d}^3\boldsymbol{k} \quad (6)$$

where the window function is

$$W(k) \equiv \frac{12\pi}{k} \int r^2 W(r) j_2(kr) \mathrm{d}r. \quad (7)$$

The quantity $\sigma_{ij}^2 = \frac{1}{3}\langle \boldsymbol{u}_i \cdot \boldsymbol{u}_j \rangle$ (where the bracket denotes the average value and i, j denote s (shell) or b (bulk) terms) is required to calculate the joint distribution of the velocities (Section 2.2):

$$\sigma_{ij}^2 = -\frac{f^2H^2}{3} \int W_i(k) W_j(k') \langle \delta_k \delta_{k'} \rangle \hat{\boldsymbol{k}}\cdot\hat{\boldsymbol{k}}' \mathrm{d}^3k \mathrm{d}^3k'. \quad (8)$$

From homogeneity (e.g. Bertschinger 1991),

$$\langle \delta_k \delta_{k'} \rangle = \delta^{\rm D}(\boldsymbol{k} + \boldsymbol{k}') P_{\rm mass}(k), \quad (9)$$

where $\delta^{\rm D}$ is the Dirac delta function, and $P_{\rm mass}(k)$ is the matter power spectrum. We estimate $P_{\rm mass}(k)$ from the power spectrum $P(k)$ of a galaxy catalogue, and assume a bias parameter b such that $P(k) = b^2 P_{\rm mass}(k)$. Therefore the one-dimensional variances may be written:

$$\begin{aligned} \sigma_{ss}^2 &= \frac{\beta^2H^2}{3} \int P(k) |W_s(k)|^2 \mathrm{d}^3k \\ \sigma_{BB}^2 &= \frac{\beta^2H^2}{3} \int P(k) |W_B(k)|^2 \mathrm{d}^3k \\ \sigma_{sB}^2 &= \frac{\beta^2H^2}{3} \int P(k) W_s(k) W_B^*(k) \mathrm{d}^3k \end{aligned} \quad (10)$$

with $\beta \equiv \Omega_0^{0.6}/b$. To this we must add the shot noise which is calculated in the next section. If we are using distance in the unit of h^{-1} Mpc and k in h Mpc^{-1}, then effectively H=100 in equation (10). Fig. 1 shows $W(r)$ in equation (4) for the shell and bulk samples, and Fig. 2 shows $|kW(k)|^2$ in equation (7).

The window functions $|W(k)|^2$ drop quite sharply at high k, even for the shell sample which is narrow in real space. For this reason the linear theory relation between $\boldsymbol{v}(\boldsymbol{k})$ and

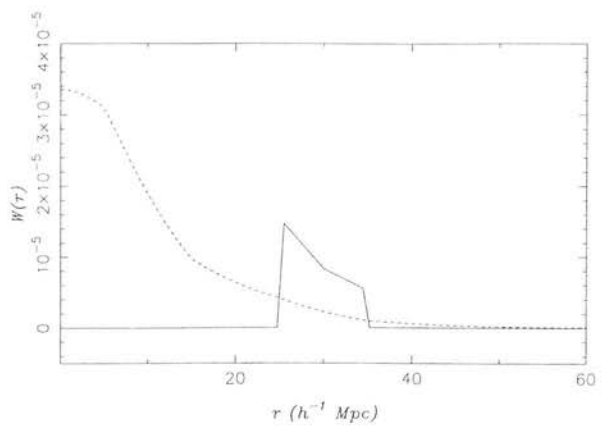

Figure 1. Normalized radial distribution $W(r)$ (see equation 4) for the shell sample R30 (solid) and the bulk sample from r=0 to 60 h^{-1} Mpc (dashed).

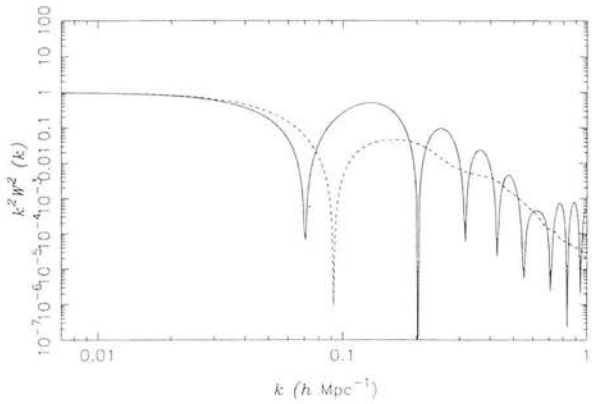

Figure 2. Window functions $k^2W^2(k)$ (see equation 7) for the two samples as in Fig. 1.

δ_k should be valid for the analysis. To illustrate that this is the case, the fraction of σ_{ss}^2 coming from the non-linear part $k > 0.29\ h$ Mpc^{-1} of the spectra considered later in this paper is only $\lesssim$0.4 per cent. The broad similarity of the two curves in Fig. 2 indicates that the bulk and shell velocities will be correlated. The bulk sample we have used in this paper runs from $r = 0$ to 60 h^{-1} Mpc and, for the shell sample, r is from 25 to 35 h^{-1} Mpc.

2.2 Noise from the peculiar velocity measurement

In equation (3) for u^α, the $\boldsymbol{v}\cdot\hat{\boldsymbol{r}}$ term in the integrand is the measured radial peculiar velocity, which is related to the true peculiar velocity $\boldsymbol{v}_t$ by $\boldsymbol{v}\cdot\hat{\boldsymbol{r}} = \boldsymbol{v}_t\cdot\hat{\boldsymbol{r}} + \varepsilon(\boldsymbol{r})$ where $\varepsilon(\boldsymbol{r})$ is the dispersion $\sigma(r)$ due to the distance and redshift errors (Kaiser & Lahav 1987). The σ_{ij}^2 in equation (8) is then

$$\langle u_i^\alpha u_j^\beta\rangle = \langle u_{iS}^\alpha u_{jS}^\beta\rangle + \langle u_{iN}^\alpha u_{jN}^\beta\rangle, \tag{11}$$

where the first term is the signal from $\boldsymbol{v}_t\cdot\hat{\boldsymbol{r}}$ and the second term is the shot noise from $\varepsilon(\boldsymbol{r})$. There is no cross-term between the signal and the noise since $\boldsymbol{v}_t\cdot\hat{\boldsymbol{r}}$ and $\varepsilon(\boldsymbol{r})$ are uncorrelated. From equation (3), the shot noise is

$$\langle u_{iN}^\alpha u_{jN}^\beta\rangle = 9\Big\langle\int \varepsilon(\boldsymbol{r})\varepsilon(\boldsymbol{r}')W_i(r)W_j(r')\hat{r}^\alpha\hat{r}'^\beta \mathrm{d}^3\boldsymbol{r}\mathrm{d}^3\boldsymbol{r}'\Big\rangle. \tag{12}$$

If we split the integration volume up into many small cells labelled by I (or J) each containing either n_I (or n_J) = 0 or 1 galaxy, then

$$\langle u_{iN}^\alpha u_{jN}^\beta\rangle = \sum_I\sum_J \hat{r}_I^\alpha\hat{r}_J^\beta\langle n_{iI}n_{jJ}\varepsilon_I\varepsilon_J\rangle W_i(r_I)W_j(r_J). \tag{13}$$

For $i = j$ (i.e. shell–shell or bulk–bulk term), $n_{iI}n_{jJ} = n_{iI} = 0$ or 1, and the galaxy errors are uncorrelated, $\langle\varepsilon_I\varepsilon_J\rangle = \sigma_I^2\delta_{IJ}^{\mathrm{K}}$ where δ_{IJ}^{K} is the Kronecker delta. With $\langle n_{iI}\rangle = \phi_i\delta^3\boldsymbol{r}$, conversion of the sum (13) to an integral gives

$$\langle u_{iN}^\alpha u_{iN}^\beta\rangle = \frac{3}{4\pi\int \mathrm{d}r\phi_i r^2/\sigma_i^2(r)}\delta_{\alpha\beta}^{\mathrm{K}}. \tag{14}$$

For $i \neq j$ (i.e. shell–bulk term), we note from MMG and Lynden-Bell et al. (1988) that the sample in MMG for the shell analysis is a sub-sample of that used by Lynden-Bell et al. for the bulk flow. Therefore $\langle n_{sI}n_{BJ}\rangle = \langle n_{sI}\rangle = \phi_{sI}\delta^3\boldsymbol{r}$ and

$$\langle u_{sN}^\alpha u_{BN}^\beta\rangle = \frac{3}{4\pi}\frac{\int r^2\mathrm{d}r\phi_s(r)/[\sigma_s(r)\sigma_B(r)]}{\int \mathrm{d}r\phi_s r^2/\sigma_s^2(r)\int \mathrm{d}r\phi_B r^2/\sigma_B^2(r)}. \tag{15}$$

The result of adding the noise to equation (10) is

$$\begin{aligned}
\sigma_{ss}^2 &= \frac{\beta^2H^2}{3}\int P(k)|W_s(k)|^2\mathrm{d}^3k + \frac{3}{4\pi\int \mathrm{d}r\phi_s r^2/\sigma_s^2(r)}\\
\sigma_{BB}^2 &= \frac{\beta^2H^2}{3}\int P(k)|W_B(k)|^2\mathrm{d}^3k + \frac{3}{4\pi\int \mathrm{d}r\phi_B r^2/\sigma_B^2(r)}\\
\sigma_{sB}^2 &= \frac{\beta^2H^2}{3}\int P(k)W_s(k)W_B^*(k)\mathrm{d}^3k\\
&\quad + \frac{3}{4\pi}\frac{\int r^2\mathrm{d}r\phi_s(r)/[\sigma_s(r)\sigma_B(r)]}{\int \mathrm{d}r\phi_s r^2/\sigma_s^2(r)\int \mathrm{d}r\phi_B r^2/\sigma_B^2(r)}.
\end{aligned} \tag{16}$$

The computed shell velocity has a noise of $\sqrt{3\langle u_{sN}^\alpha u_{sN}^\alpha\rangle}$= 367 km s^{-1} while the bulk velocity has a noise of $\sqrt{3\langle u_{BN}^\alpha u_{BN}^\alpha\rangle}$=124 km s^{-1}, so we see that the measured shell velocity could be entirely due to noise, whereas the bulk velocity is detected at a high signal-to-noise ratio.

2.3 Probability distribution of the shell and bulk velocities

For Gaussian fluctuations, the joint distribution of the six variables $x_i = (u_s^\alpha, u_B^\beta)$ is a multivariate Gaussian:

$$\begin{aligned}
p(x_i)\mathrm{d}^6x_i &= \frac{1}{(2\pi)^3\parallel M_{ij}\parallel^{1/2}}\times\\
&\quad \exp\left[-\frac{1}{2}(x_i-\bar{x}_i)M_{ij}^{-1}(x_j-\bar{x}_j)\right]\mathrm{d}^6x_i
\end{aligned} \tag{17}$$

where

$$M_{ij} \equiv \langle(x_i-\bar{x}_i)(x_j-\bar{x}_j)\rangle \tag{18}$$

and

$$\begin{aligned}
\langle u_s^\alpha u_B^\beta\rangle &= \sigma_{sB}^2\delta_{\alpha\beta}^{\mathrm{K}}\\
\langle u_s^\alpha u_s^\beta\rangle &= \sigma_{ss}^2\delta_{\alpha\beta}^{\mathrm{K}}\\
\langle u_B^\alpha u_B^\beta\rangle &= \sigma_{BB}^2\delta_{\alpha\beta}^{\mathrm{K}}.
\end{aligned} \tag{19}$$

Equation (17) is then

$$p(x_i)\mathrm{d}^6x_i = \frac{1}{(2\pi)^3(\sigma_{ss}^2\sigma_{BB}^2 - \sigma_{sB}^4)^{3/2}} \times \exp\left[-\frac{u_s^2\sigma_{BB}^2 + u_B^2\sigma_{ss}^2 - 2\boldsymbol{u}_s\cdot\boldsymbol{u}_B\sigma_{sB}^2}{2(\sigma_{ss}^2\sigma_{BB}^2 - \sigma_{sB}^4)}\right]\mathrm{d}^6x_i. \quad (20)$$

Rewriting equation (20) in terms of $|\boldsymbol{u}_s|$,$|\boldsymbol{u}_B|$ and $\mu = \hat{\boldsymbol{u}}_s\cdot\hat{\boldsymbol{u}}_B$:

$$p(u_s,u_B,\mu)\mathrm{d}u_s\mathrm{d}u_B\mathrm{d}\mu = \frac{u_s^2u_B^2}{\pi\Gamma^{3/2}} \times \exp\left[-\frac{(u_s^2\sigma_{BB}^2 + u_B^2\sigma_{ss}^2 - 2u_su_B\mu\sigma_{sB}^2)}{2\Gamma}\right]\mathrm{d}u_s\mathrm{d}u_B\mathrm{d}\mu \quad (21)$$

where $\Gamma = (\sigma_{ss}^2\sigma_{BB}^2 - \sigma_{sB}^4)$. Equation (21) is essentially the same as equation (8) of Peacock (1992). For our purpose, it would be more useful to work out the probability distribution of the shell–bulk velocity ratio rather than the absolute magnitude of $\boldsymbol{u}_s$ and $\boldsymbol{u}_B$. For that we define two new parameters (see Peacock 1992):

$$A \equiv \mu\frac{\sigma_{sB}^2}{\sigma_{ss}\sigma_{BB}} \equiv \mu r$$
$$B \equiv \frac{u_s}{u_B}\frac{\sigma_{BB}}{\sigma_{ss}} \equiv \frac{u_s}{u_B}F. \quad (22)$$

In terms of A and B, $p(u_s,u_B,\mu)$ can be rewritten as:

$$p(A,B)\mathrm{d}A\mathrm{d}B = \frac{8B^2(1-r^2)^{3/2}}{\pi r(1+B^2-2AB)^3}\mathrm{d}A\mathrm{d}B. \quad (23)$$

To obtain the distribution of velocity ratio $R = u_s/u_B$, equation (23) is integrated from $A=-r$ to $A=r$ which gives:

$$p(R)\mathrm{d}R = \frac{16F^3R^2(1-r^2)^{3/2}(1+F^2R^2)}{\pi[(1+F^2R^2)^2 - 4r^2F^2R^2]^2}\mathrm{d}R. \quad (24)$$

To obtain the distribution in μ, equation (23) is integrated from $B=0$ to $B=\infty$ which yields

$$p(\mu)\mathrm{d}\mu = \frac{3\mu r(1-r^2)^{3/2}}{\pi(1-\mu^2r^2)^2} + \frac{(1-r^2)^{3/2}(1+2\mu^2r^2)}{\pi(1-\mu^2r^2)^{5/2}}\left[\frac{\pi}{2} - \tan^{-1}\left(\frac{-\mu r}{\sqrt{1-\mu^2r^2}}\right)\right]\mathrm{d}\mu. \quad (25)$$

To complete our analysis, we also integrate equation (21) from $\mu=-1$ to $\mu=+1$ to get

$$p(u_s,u_B)\mathrm{d}u_s\mathrm{d}u_B = \frac{u_su_B}{\pi\Gamma^{1/2}\sigma_{sB}^2} \times \left\{\exp\left[-\frac{(u_s^2\sigma_{BB}^2 + u_B^2\sigma_{ss}^2 - 2u_su_B\sigma_{sB}^2)}{2\Gamma}\right] - \exp\left[-\frac{(u_s^2\sigma_{BB}^2 + u_B^2\sigma_{ss}^2 + 2u_su_B\sigma_{sB}^2)}{2\Gamma}\right]\right\}\mathrm{d}u_s\mathrm{d}u_B. \quad (26)$$

3 RESULTS

It is clear that the interpretation of the shell–bulk ratio is dependent on the power spectrum $P(k)$. To calculate the joint probability distribution, we consider two parametrized forms for the power spectrum. We take the empirical power spectrum of Peacock & Dodds (1994), obtained from fits to a variety of galaxy catalogues:

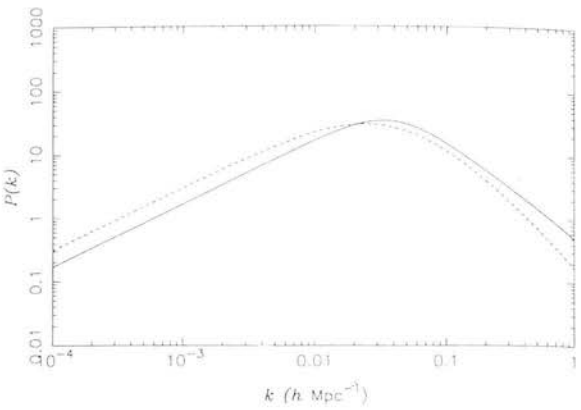

Figure 3. Power spectrum $P(k)$. The solid line represents the galaxy power spectrum of Peacock & Dodds (1994) while the dashed line represents the CDM model normalized to *COBE* with $\Gamma = 0.2$ and $\Omega_0 = 1$.

$$\Delta^2(k) = \frac{(k/k_0)^\alpha}{1+(k/k_c)^{\alpha-\beta}}, \quad (27)$$

with k_0=0.29±0.01 h Mpc^{-1}, k_c=0.039±0.002 h Mpc^{-1}, α=1.5±0.03, and β=4.0±0.5. Note that, since the shapes of the power spectra of the catalogues used are similar (Peacock 1991), it is plausible that, at least on the reasonably large scales used here, the mass power spectrum will also have the same shape. The only variable then is the normalization of the matter power spectrum, which can be expressed in terms of the bias parameter of any of the catalogues. We have chosen to express the matter power spectrum in terms of the *IRAS* power spectrum, for which (27) is a reasonable fit; we will then obtain constraints involving the *IRAS* bias parameter. This, of course, is entirely independent of the elliptical galaxy sample which has been used to trace the peculiar velocity field. We note in passing that spirals and ellipticals give qualitatively the same velocity fields (Dekel 1994). In addition to this empirical power spectrum, we also consider a CDM-like power spectrum with a shape parameter Γ (Kolb & Turner 1990):

$$P(k) = \frac{Ak^n}{(1+yk+wk^{1.5}+\gamma k^2)^2}, \quad (28)$$

where $y = 1.7\Gamma^{-1}h^{-1}$ Mpc, $w = 9\Gamma^{-1.5}h^{-1.5}$ Mpc$^{1.5}$, $\gamma = 1.0\Gamma^{-2}h^{-2}$ Mpc^2, n=1 for the Harrison–Zeldovich spectrum, and A is the normalization factor. We allow Γ to be a free parameter, bearing in mind that $\Gamma = \Omega_0 h = 0.5$ in the standard CDM scenario, and $\Gamma \simeq 0.2$ is an approximate fit to the galaxy data. A is chosen to be normalized to the *COBE* spectrum (Efstathiou, Bond & White 1992) for the spatially flat models:

$$A = \frac{3}{20\pi}\left(\frac{Q_{\mathrm{rms}}}{T_0}\right)^2\left(\frac{2c}{H_0}\right)^4\Omega_0^{-1.54}, \quad (29)$$

where $Q_{\mathrm{rms}} = 19.4^{+2.3}_{-2.1}$ μK (Banday et al. 1994), T_0 is the mean temperature of the background radiation ($T_0 = 2.735 \pm 0.006$ K), and c is the speed of light. Fig. 3 shows the plot of these two power spectra with Γ=0.2 for equation (28).

For the power spectrum of Peacock & Dodds (1994), Figs 4 and 5 show the plots of the probability distributions

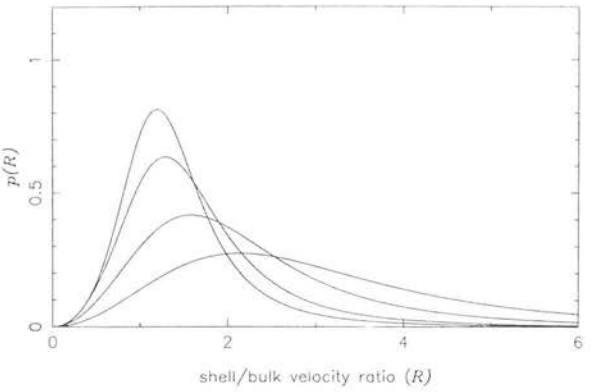

Figure 4. Probability distribution $p(R)$ of $R = u_s/u_B$ for the R30 shell at 30 h^{-1} Mpc and a bulk radius of 60 h^{-1} Mpc. The power spectrum used is that from Peacock & Dodds (1994) and the values of β chosen are, in order of increasing peak height, 0.1, 0.5, 1.0, and 1.5.

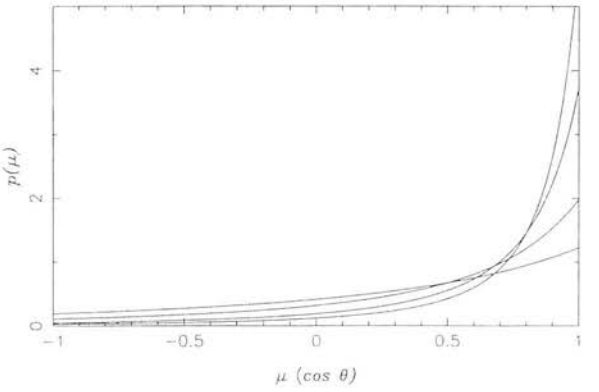

Figure 5. Probability distribution $p(\mu)$ of $\mu = \hat{\boldsymbol{u}}_s \cdot \hat{\boldsymbol{u}}_B$ for the R30 shell at 30 h^{-1} Mpc and a bulk radius of 60 h^{-1} Mpc using the power spectrum of Peacock & Dodds (1994). The values of β chosen are, in increasing order at the right of the graph, 0.1, 0.5, 1.0, and 1.5.

$p(R)$ and $p(\mu)$ (see equations (24) and (25)) with β=0.1, 0.5, 1.0 and 1.5 for the R30 shell and a bulk radius of 60 h^{-1} Mpc. We also calculated the probability that the shell–bulk velocity ratio is smaller than 0.4; and in this case the probability turns out to be around 0.3–1.6 per cent depending on the value of β, with a value of 1.5 per cent being favoured by recent determinations of $\beta \simeq 1$ (e.g. Heavens & Taylor 1995). Varying β alters the amplitude of the matter power spectrum, if Ω_0 is fixed, and the distribution of the shell–bulk ratio then changes only as a result of the difference in the relative contribution from shot noise. Table 2 shows the result of $\sqrt{3}\sigma_{ss}$, $\sqrt{3}\sigma_{BB}$, the correlation coefficient r, and the percentage chance of $u_s \leqslant 0.4u_B$ for different values of β. We apply a slightly less stringent ratio than observed, since the solar motion with respect to the CMB used by Lynden-Bell et al. has a modest error. The high value of the correlation coefficient r suggests that the shell and the bulk velocities are strongly correlated, and so it is unusual to find a stationary shell in a large bulk flow environment for this power spectrum. Indeed, inspection of the window function (Fig. 2) suggests that, with almost any smooth $P(k)$, the shell and bulk velocities will be strongly correlated, unless the variances are completely dominated by shot noise. In passing, we note that the cosine of the misalignment angle, $\mu = 0.62$, is quite compatible with the results shown in Fig. 5.

Table 2. Results of $\sqrt{3}\sigma_{ss}$, $\sqrt{3}\sigma_{BB}$ (in km s^{-1}), the correlation coefficient r, the percentage chance of u_s/u_B being smaller than 0.4, and the integral $\int p$ over $p \leqslant p(u_s = 240, u_B = 600)$ (in per cent) for different values of β for the power spectrum of Peacock & Dodds (1994). Note that the rms shell and bulk velocities are $\sqrt{3}\sigma_{ss}$ and $\sqrt{3}\sigma_{BB}$.

	$\sqrt{3}\sigma_{ss}$	$\sqrt{3}\sigma_{BB}$	r	$p(R<.4)/\%$	$\int p/\%$
$\beta = 0.1$	369	129	0.35	0.4	2.1×10^{-12}
$\beta = 0.5$	413	213	0.50	0.9	1.2×10^{-3}
$\beta = 1.0$	529	367	0.67	1.5	1.9
$\beta = 1.5$	679	533	0.75	1.6	10.4

Table 3. Results of $\sqrt{3}\sigma_{ss}$, $\sqrt{3}\sigma_{BB}$ (in km s^{-1}), the correlation coefficient r, the percentage chance of u_s/u_B being smaller than 0.4, and the integral $\int p$ over $p \leqslant p(u_s = 240, u_B = 600)$ (in per cent) for different values of Γ and Ω_0 for the CDM-like model normalized to *COBE*. As the *COBE* temperature variations arise from mass fluctuations, the effective bias parameter b is unity.

	Ω_0:	0.1	0.5	1.0	1.5
$\Gamma = 0.2$	$(\sqrt{3}\sigma_{ss})$	653	551	518	501
	$(\sqrt{3}\sigma_{BB})$	518	400	341	339
	(r)	0.76	0.70	0.68	0.66
	$(p(R \leqslant 0.4))$	1.6	1.6	1.5	1.5
	$(\int p)$	8.6	2.8	0.7	0.9
$\Gamma = 0.3$	$(\sqrt{3}\sigma_{ss})$	793	650	599	575
	$(\sqrt{3}\sigma_{BB})$	620	478	430	404
	(r)	0.76	0.72	0.69	0.68
	$(p(R \leqslant 0.4))$	1.6	1.6	1.5	1.5
	$(\int p)$	14.7	7.5	4.8	3.5
$\Gamma = 0.5$	$(\sqrt{3}\sigma_{ss})$	1037	824	750	714
	$(\sqrt{3}\sigma_{BB})$	752	577	516	483
	(r)	0.71	0.69	0.68	0.67
	$(p(R \leqslant 0.4))$	1.5	1.5	1.5	1.4
	$(\int p)$	17.3	14.1	11.0	8.9

It is important to note that the 1.5 per cent probability is not as significant as it appears, since this shell has been chosen for analysis as the most extreme of a sample of N=10. If all shells had the same $p(R \leqslant 0.4)$, then the probability of the most extreme R being $\leqslant 0.4$ would be $1-(1-0.015)^{10}$=14 per cent $\simeq Np(R \leqslant 0.4)$.

The results for the *COBE*-normalized flat CDM-like models are shown in Table 3, with the probability distributions $p(R)$ shown in Fig. 6. Once again we find consistently a probability of about 1.5 per cent for $u_s \leqslant 0.4\,u_B$. The results are insensitive to the value of Ω_0 since the normalization of the amplitude of the power spectrum $\propto \Omega_0^{-0.77}$ more-or-less cancels the growth rate $\propto \Omega_0^{0.6}$.

In Fig. 7, we show the joint distribution of shell and bulk speeds, for a variety of models. The striking aspect of this is that the high amplitude of the bulk flow is difficult to achieve unless the matter power spectrum has high amplitude. Tables 2 and 3 show the probability of the observations lying outside the contour passing through u_s=240, u_B=600 km s^{-1}. We see a consistent story with the ratio test: low-amplitude models with

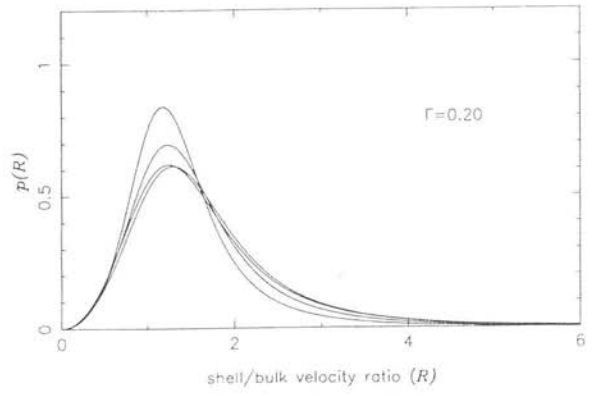

(a) $\Gamma = 0.2$

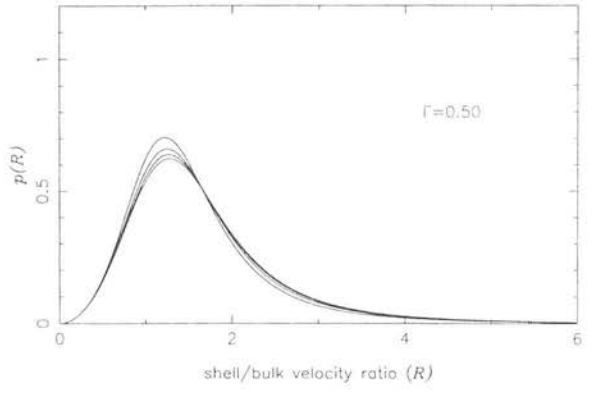

(b) $\Gamma = 0.5$

Figure 6. The distribution of the shell–bulk velocity ratio for the CDM-like models normalized to *COBE* with Γ= (a) 0.2 and (b) 0.5, for values of Ω_0, in decreasing order of peak height, of 0.1, 0.5, 1 and 1.5.

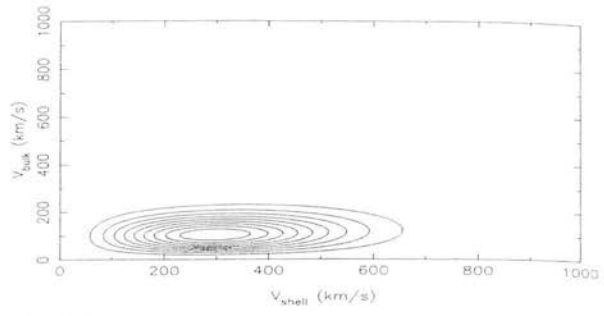

(a) $\beta = 0.1$

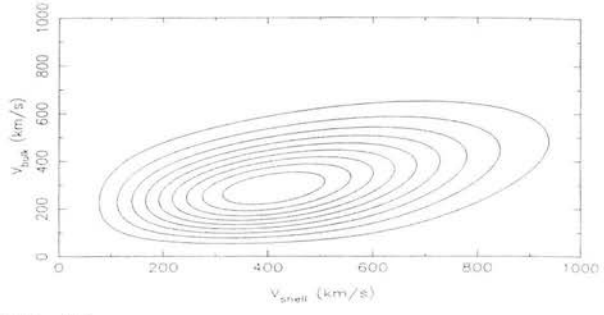

(b) $\beta = 1.0$

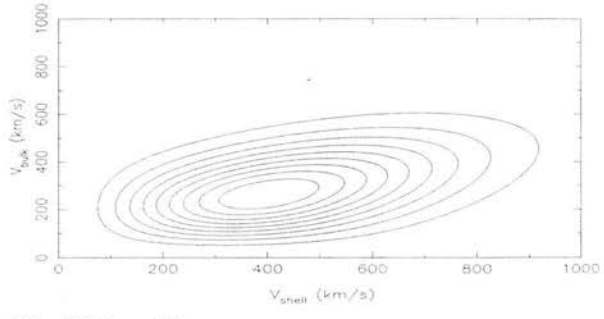

(c) $\Gamma = 0.2$, $\Omega_0 = 1.0$

Figure 7. Contour plot of the probability distribution $p(u_s, u_B)$ (equation (26)) of the bulk and shell velocities for the power spectrum of Peacock & Dodds (1994) with β= (a) 0.1, (b) 1.0. (c) shows a CDM-like model with $\Gamma = 0.2$, normalized to *COBE* with $\Omega_0 = 1$.

$\beta \lesssim 1$ are strongly excluded, but the probability is $\sim$1 per cent for the high-amplitude β=1 model and the *COBE*-normalized Γ=0.2 model.

4 DISCUSSION

We have calculated the joint distribution for the shell and bulk velocities, concentrating on the probability distribution for the ratio of the two magnitudes, assuming Gaussian fluctuations. The main motivation for this is that the ratio is, in the absence of noise, a test of the shape of the power spectrum, independent of its amplitude. In practice this turns out not to be the case, since shot noise in the shell velocities of current surveys is very large, and the shell solutions tend to be of limited use. However, the joint distribution of shell and bulk speeds can be used effectively to test galaxy formation models, provided that the noise and correlations are correctly accounted for.

We have applied the analysis to the shell of galaxies at $30\pm5\ h^{-1}$ Mpc investigated by MMG, and the bulk elliptical galaxy sample within $60\ h^{-1}$ Mpc of Lynden-Bell et al. (1988). We find that the probability of the ratio of the shell and bulk speeds being lower than the observed one is approximately 1.5 per cent, for power spectra of the shape required to fit the galaxy data and amplitude and Ω_0 sufficient to account for the magnitude of the bulk motion. Since we have considered the most extreme shell (of ten) in the MMG sample, we conclude that the small observed ratio does not itself present any serious challenge to the standard model of galaxy formation, i.e. gravitational instability of initially Gaussian fluctuations.

We have made two simplifying assumptions in the analysis. First, the sky coverage of the samples was assumed to be uniform, which allows us to use a scalar window function. Had the results of this analysis been highly significant, a more detailed treatment using the exact dataset would be justified. Secondly, the original shell and bulk velocity calculations involved some pre-grouping of galaxies in order to reduce noise, a process which we have ignored. The effect of this is, however, only significant nearby, since the variance for a group of N

galaxies (Lynden-Bell et al. 1988)

$$\sigma^2 = \sigma_z^2 + r^2[\exp(\Delta^2/N) - 1] \quad (30)$$

tends to $r^2\Delta^2/N$ at large r and the group behaves like N independent galaxies. We investigated the effect of the grouping by reducing the nearby selection function to that for groups. Taking the most pessimistic assumptions of largest group size and group variance equal to the galaxy variance, we find that the probabilities are virtually unchanged. We therefore do not think that the pre-grouping matters.

The joint distribution of the shell speed and the bulk speed is a more sensitive test of the amplitude than of the shape. Here we find that the high-amplitude model based on the *IRAS* galaxy power spectrum is acceptable provided that *IRAS* galaxies have $\beta \simeq 1$. Similarly the Γ=0.2 *COBE*-normalized flat models are not excluded for any value of Ω_0. As expected, if β for the *IRAS* sample drops below unity, it becomes very difficult to account for the high bulk speed observed.

ACKNOWLEDGMENTS

We thank Starlink for facilities in which all the computations were carried out, and Andy Taylor for his useful comments. HYL would also like to thank the Lee foundation for financial support.

REFERENCES

Calzetti D., Giavalisco M., 1993, ApJ, 406, 338
Banday A.J. et al., 1994, ApJ, 439, 99
Bertschinger E., 1991, in Martinez V.S., Portilla M., Saez D., eds, New Insights into the Universe. Springer-Verlag, Berlin, p.65
Dekel A., 1994, ARA&A, 32, 371
Dressler A., Faber S.M., Burstein D., Davies R.L., Lynden-Bell D., Terlevich R.J., Wegner G., 1987, ApJ, 313, L37
Efstathiou G., Bond J.R., White S.D.M., 1992, MNRAS, 258, 1
Heavens A.F., Taylor A.N., 1995, MNRAS, 275, 483
Kaiser N., 1988, MNRAS, 231, 149
Kaiser N., Lahav O., 1987, in Rubin V.C., Coyne G.V., eds, Large Scale Motions in the Universe. Princeton University Press, Princeton, p.339
Kolb E.W., Turner M.S., 1990, The Early Universe, Frontiers in Physics Lecture Note Series, Addison Wesley
Lynden-Bell D., Faber S.M., Burstein D., Davies R.L., Dressler A., Terlevich R.J., Wegner G., 1988, ApJ, 326, 19
Martin-Mirones J.M., Goicoechea L.J., 1992, A&A, 253, 3 (MMG)
Peacock J.A., 1991, MNRAS, 253, 1P
Peacock J.A., 1992, MNRAS, 258, 581
Peacock J.A., Dodds S.J., 1994, MNRAS, 267, 1020
Peebles P.J.E., 1980, The Large Scale Structure of the Universe. Princeton University Press, Princeton, NJ

This paper has been produced using the Royal Astronomical Society/Blackwell Science LaTeX style file.